

# For Reference

NOT TO BE TAKEN FROM THIS ROOM



Ex libris  
UNIVERSITATIS  
ALBERTAEENSIS







Digitized by the Internet Archive  
in 2019 with funding from  
University of Alberta Libraries

<https://archive.org/details/Campos1983>









THE UNIVERSITY OF ALBERTA

RELEASE FORM

NAME OF AUTHOR            RAMIRO PEREZ CAMPOS  
TITLE OF THESIS            EXPERIMENTAL AND THEORETICAL ASSESSMENTS  
                              OF SOME APPROXIMATIONS IN THE DYNAMICAL  
                              THEORY OF ELECTRON DIFFRACTION  
DEGREE FOR WHICH THESIS WAS PRESENTED    DOCTOR OF PHILOSOPHY  
YEAR THIS DEGREE GRANTED    FALL 1983

Permission is hereby granted to THE UNIVERSITY OF ALBERTA LIBRARY to reproduce single copies of this thesis and to lend or sell such copies for private, scholarly or scientific research purposes only.

The author reserves other publication rights, and neither the thesis nor extensive extracts from it may be printed or otherwise reproduced without the author's written permission.





THE UNIVERSITY OF ALBERTA

EXPERIMENTAL AND THEORETICAL ASSESSMENTS OF SOME  
APPROXIMATIONS IN THE DYNAMICAL THEORY OF ELECTRON  
DIFFRACTION

by



RAMIRO PEREZ CAMPOS

A THESIS

SUBMITTED TO THE FACULTY OF GRADUATE STUDIES AND RESEARCH  
IN PARTIAL FULFILMENT OF THE REQUIREMENTS FOR THE DEGREE  
OF DOCTOR OF PHILOSOPHY

DEPARTMENT OF PHYSICS

EDMONTON, ALBERTA

FALL 1983





83F-55D

THE UNIVERSITY OF ALBERTA  
FACULTY OF GRADUATE STUDIES AND RESEARCH

The undersigned certify that they have read, and recommend to the Faculty of Graduate Studies and Research, for acceptance, a thesis entitled EXPERIMENTAL AND THEORETICAL ASSESSMENTS OF SOME APPROXIMATIONS IN THE DYNAMICAL THEORY OF ELECTRON DIFFRACTION submitted by RAMIRO PEREZ CAMPOS in partial fulfilment of the requirements for the degree of DOCTOR OF PHILOSOPHY.





## DEDICATION

TO MY FOUR JEWELS, CONSUELO, NATY, GABY AND MARIANA FOR  
THEIR STEADFAST SUPPORT AND INSPIRATION DURING THIS  
STRUGGLE.



## ABSTRACT

The effects of the  $(1\ 0\ 0)$ ,  $(0\ 0\ 2)$  and  $(1\ -1\ 1)$  systematic sets of reflections are studied in HCP cobalt. The three systematic sets are similar in that the reciprocal lattice vectors  $\vec{g}_{(100)}$ ,  $\vec{g}_{(002)}$  and  $\vec{g}_{(1-11)}$  are very nearly the same in magnitude. Experimental results indicate that the effects of systematic reflections in the  $(0\ 0\ 2)$  and  $(1\ -1\ 1)$  sets are similar, however, the effects in the  $(1\ 0\ 0)$  set are very different from the previous cases. An analysis of the results in terms of Bloch wave parameters is carried out, also, transmission beam characteristics in the three systematic sets are explored. A discussion of the dark field results in terms of Bloch wave symmetries indicate that an assessment of the importance of systematic reflections can be obtained through a comparison of the operating voltage to the critical voltage.

An identification method of the nature of stacking faults in HCP materials is proposed. The method is based on comparisons between image contrast obtained for the different types of stacking faults in HCP materials when the  $(1\ -1\ 1)$  reflection satisfies its Bragg condition. Under this circumstance an extrinsic stacking fault give rises to a phase angle equal to  $\pm\pi$ . However, the two types of intrinsic faults give rise to phase angles equal to  $\pm 2\pi/3$  and  $\pm\pi/3$ .

A form of the many-beam dynamical theory applicable to twinned crystals and taking effects of common reflections





into account is developed. The treatment is based on a description of electrons in the twinned crystals in terms of Bloch waves. It has been shown in this chapter that the methods of Sutton and Pond and Gratias and Portier and the Bloch wave approach in the present treatment are completely equivalent.

Experimental evidence is presented which indicates that the widespread use of symmetrical Laue diffraction conditions in theoretical calculations of diffraction contrast can lead to significant errors. The experiments consisted of a comparison of thickness fringes in  $g$  and  $-g$  dark field images obtained with the crystal set at the symmetry position. Calculations based on the assumption of symmetrical Laue diffraction conditions give thickness fringes in  $g$  and  $-g$  dark field images which are identical. Experiment showed, however, that these thickness fringes are, in fact, quite different. Excellent agreement between experiment and theoretical intensity profiles based on a form of the dynamical theory of electron diffraction applicable to the non-symmetrical Laue case was found.

Experimental evidence is presented which indicates that calculations of diffraction contrast in electron microscope images obtained under weak beam diffraction conditions can be in considerable error if the column approximation is employed. This evidence is based on a comparison of experimental densitometer traces obtained from stacking faults in FCC cobalt with theoretical non-column and column



approximation calculations. A theoretical explanation of the significant differences between non-column and column approximation profiles is also given and some interpretative errors which can arise if the column approximation is employed are discussed.





## ACKNOWLEDGMENT

I would like to thank Professor S. S. Sheinin for the supervision of this work and also for the opportunity he provided me to work in his research group.

Part of this research has been carried out in collaboration with Dr. K. Z. Botros and Dr. H. S. Kim to whom I wish to express my sincere thanks.

Finally I wish to thank the Canada Council and the SSHRC of Canada for the financial support for part of my academic endeavors. I am indebted to the Consejo Nacional de Ciencia y Tecnologia of Mexico for the financial support during the last years of my program. I wish to thank the University of Alberta for partial financial assistance.



## Table of Contents

	<u>Page</u>
1. INTRODUCTION .....	1
2. THE DYNAMICAL THEORY OF ELECTRON DIFFRACTION .....	6
2.1 REVIEW OF THE DYNAMICAL THEORY FOR PERFECT CRYSTALS .....	6
2.2 CALCULATIONS OF THE DIFFRACTED BEAM INTENSITIES IN A PERFECT CRYSTAL .....	13
2.3 INELASTIC SCATTERING AND ABSORPTION .....	15
2.4 THEORETICAL APPROACH TO CALCULATE THE STACKING FAULT IMAGE CONTRAST USING THE DYNAMICAL THEORY .....	17
2.5 INTERBRANCH AND INTRABRANCH DYNAMICAL SCATTERING FOR A STACKING FAULT .....	21
3. APPROXIMATIONS INVOLVED IN THE DYNAMICAL THEORY OF ELECTRON DIFFRACTION AND OBJECTIVES OF THE PRESENT WORK .....	26
3.1 INTRODUCTION .....	26
3.2 THE MANY-BEAM APPROXIMATION .....	26
3.2.1 The many-beam approximation in perfect HCP crystals. ....	28
3.2.2 The many-beam approximation in HCP crystals containing stacking faults. ....	30
3.2.3 The many-beam approximation in crystals containing twin boundaries. ....	31
3.3 SYMMETRICAL LAUE DIFFRACTION CONDITIONS .....	35
3.4 THE COLUMN APPROXIMATION .....	37
4. EFFECTS OF SYSTEMATIC REFLECTIONS ON DIFFRACTION CONTRAST IN HCP COBALT .....	40
4.1 INTRODUCTION .....	40
4.2 EXPERIMENTAL METHOD .....	44
4.2.1 SPECIMEN PREPARATION .....	45





4.2.2	ELECTRON MICROSCOPE EXAMINATION .....	45
4.2.3	MEASUREMENTS OF NORMALIZED EXTINCTION DISTANCES .....	48
4.3	RESULTS .....	50
4.3.1	RESULTS OF $\xi / \xi_0$ VERSUS $\Delta \theta$ MEASUREMENTS .....	52
4.3.2	ANALYSIS OF THE RESULTS IN TERMS OF BLOCH WAVE PARAMETERS .....	58
4.3.2.1	ANALYSIS OF THE DARK AND BRIGHT FIELD RESULTS FOR THE (1 0 0) SYSTEMATIC SET. ....	58
4.4	EFFECTS OF HCP SYSTEMATIC REFLECTIONS ON ANOMALOUS ABSORPTION .....	63
4.4.1	BLOCH WAVE ABSORPTION COEFFICIENTS FOR THE (1 0 0), (0 0 2) AND (1 -1 1) SYSTEMATIC REFLECTIONS .....	68
4.4.1.1	RELATIONSHIP BETWEEN ABSORPTION COEFFICIENTS AND BLOCH WAVE CHANNELING. ....	72
4.4.2	TRANSMISSION PROPERTIES FOR HCP SYSTEMATIC REFLECTIONS .....	75
4.5	ON THE RELATIONSHIP BETWEEN THE EFFECTS OF SYSTEMATIC REFLECTIONS AND ACCELERATION VOLTAGE. ....	77
4.6	DISCUSSION .....	86
5.	EFFECTS OF SYSTEMATIC REFLECTIONS ON THE STACKING FAULT IMAGE CONTRAST IN HCP COBALT .....	88
5.1	INTRODUCTION .....	88
5.2	DISPLACEMENT VECTORS AND PHASE ANGLES OF STACKING FAULTS IN HCP STRUCTURES .....	89



5.3	IMAGE CONTRAST CHARACTERISTICS OF STACKING FAULTS WHEN THE (1 -1 1) SYSTEMATIC SET IS EXCITED .....	93
5.4	EXPERIMENTAL RESULTS .....	101
5.5	ANALYSIS OF THE RESULTS IN TERMS OF THE TWO-BEAM APPROXIMATION .....	102
5.6	CONCLUSIONS .....	106
6.	DYNAMICAL THEORY OF TWIN BOUNDARY CONTRAST INCLUDING EFFECTS OF COMMON REFLECTIONS .....	108
6.1	INTRODUCTION .....	108
6.2	DYNAMICAL THEORY FOR TWIN BOUNDARY CONTRAST .....	112
6.2.1	BLOCH WAVES IN THE TWIN .....	112
6.2.2	DYNAMICALLY COUPLED SETS OF DIFFRACTED BEAMS .....	115
6.2.3	DYNAMICAL EQUATIONS FOR THE TWIN .....	115
6.2.4	DIFFRACTED BEAM AMPLITUDE .....	118
6.3	COMPARISON OF BLOCH WAVE APPROACH WITH METHOD OF GRATIAS AND PORTIER .....	120
6.4	COMPARISON OF BLOCH WAVE APPROACH WITH METHOD OF SUTTON AND POND .....	125
6.5	DISCUSSION AND CONCLUSIONS .....	129
7.	EXPERIMENTAL EVIDENCE SHOWING THAT THE USE OF SYMMETRICAL LAUE DIFFRACTION CONDITIONS IN THE DYNAMICAL THEORY OF ELECTRON DIFFRACTION CAN GIVE SIGNIFICANT ERRORS IN DIFFRACTION CONTRAST CALCULATIONS .....	131
7.1	INTRODUCTION .....	131
7.2	THEORETICAL BACKGROUND .....	132
7.2.1	DYNAMICAL THEORY FOR THE NSL CASE .....	132
7.3	DIFFRACTED BEAM INTENSITY AT THE BOTTOM SURFACE OF A WEDGE CRYSTAL. ....	134



7.4	ANALYSIS OF IMPORTANT BLOCH WAVES CONTRIBUTING TO DIFFRACTED BEAM INTENSITY AT THE SYMMETRY POSITION. ....	136
7.5	EXPERIMENTAL RESULTS .....	140
7.5.1	SPECIMEN REQUIREMENTS .....	140
7.5.2	EXPERIMENTAL PROCEDURE .....	141
7.6	COMPARISON OF THEORY WITH EXPERIMENT .....	143
7.7	DISCUSSION .....	145
7.8	CONCLUSIONS .....	148
8.	EXPERIMENTAL EVIDENCE OF A BREAKDOWN OF THE COLUMN APPROXIMATION IN CALCULATIONS OF CONTRAST IN ELECTRON MICROSCOPE IMAGES OF STACKING FAULTS .....	150
8.1	INTRODUCTION .....	150
8.2	EXPERIMENTAL PROCEDURE .....	151
8.3	COMPARISON OF THEORY WITH EXPERIMENTAL RESULTS .....	152
8.4	EXPLANATION OF DIFFERENCES BETWEEN COLUMN AND NON-COLUMN PROFILES .....	157
8.5	DISCUSSION .....	162
9.	SUGGESTIONS FOR FURTHER WORK .....	165
	BIBLIOGRAPHY .....	167





## List of Figures

<u>Figure</u>		<u>Page</u>
2.1	The dispersion surface and the Ewald sphere construction for high energy electrons.....	11
2.2	A crystal containing a stacking fault at a depth $t$ , parallel to both surfaces of the crystal. $\vec{R}$ is the displacement vector of the fault.....	18
2.3	Two beam dispersion surface for a crystal containing a stacking fault inclined to the crystal surfaces.....	22
3.1	An experimental diffraction pattern obtained under systematic reflection conditions in HCP cobalt.....	27
3.2	A portion of a typical diffraction pattern in the non-systematic case. Many diffracted beams are important and must be taken into account in calculating the $A$ matrix of the dynamical theory.....	29
3.3	a) Illustration showing a twin boundary inclined to the surface of a specimen of thickness $t$ . b) Schematic diffraction pattern obtained from a twin boundary such as the one shown in a).....	32
3.4	Schematic drawings of a crystal under: a) symmetrical Laue diffraction conditions. b) non-symmetrical Laue diffraction conditions.....	36
4.1	TABLE 1.-Ratio of the structure factor to the atomic scattering amplitude for the first order reflections.....	42
4.2	Ratio of the structure factor to the atomic scattering amplitude for Class 0, 1, 2 and 3, as a function of the order of the reflection.....	43
4.3	Bright field image of a wedge-shaped crystal of HCP cobalt showing the presence of extinction contours.....	47



4.4	Diffraction pattern showing a systematic set of reflections. The reflection $4\bar{g}$ satisfies its Bragg condition therefore the Kikuchi line pass through the middle of the spot.....	49
4.5	Microdensitometer trace showing the spacing of the extinction contours.....	51
4.6	The variation of the dark field extinction distance at 150KV normalized to the value at the Bragg condition, with deviation from the Bragg condition of the (1 0 0) reflection.....	53
4.7	The variation of the dark field extinction distance at 150KV normalized to the value at the Bragg condition, with deviation from the Bragg condition of the (1 -1 1) reflection.....	54
4.8	The variation of the dark field extinction distance at 150KV normalized to the value at the Bragg condition, with deviation from the Bragg condition of the (0 0 2) reflection.....	55
4.9	An intensity profile of the variation with depth of the (1 -1 1) diffracted beam intensity at 150KV and found from a 13-beam approximation.....	56
4.10	The variation of the bright field extinction distance at 150KV normalized to the value at the Bragg condition, with deviation from the Bragg condition of the (1 0 0) reflection.....	59
4.11	The variation of the bright field extinction distance at 150KV normalized to the value at the Bragg condition, with deviation from the Bragg condition of the (1 -1 1) reflection.....	60
4.12	The variation of the bright field extinction distance at 150KV normalized to the value at the Bragg condition, with deviation from the Bragg condition of the (0 0 2) reflection.....	61



4.13	The variation of $ C^{(1)}C^{(1)}_g $ with deviation from the Bragg condition of the (1 0 0) reflection for Bloch waves 1 to 4. a) dark field, b) bright field.....	64
4.14	Branches of the dispersion surface for Bloch waves 1 to 4 in the (1 0 0) systematic set.....	65
4.15	An intensity profile showing the decrease in fringe contrast as the thickness of the crystal is increased.....	66
4.16	Bloch wave absorption coefficients $q^{(1)}$ as a function of the crystal orientation for the (1 0 0) set.....	69
4.17	Bloch wave absorption coefficients $q^{(1)}$ as a function of the crystal orientation for the (1 -1 1) set.....	70
4.18	Bloch wave absorption coefficients $q^{(1)}$ as a function of the crystal orientation for the (0 0 2) set.....	71
4.19	Bloch wave intensities for the two most important Bloch waves at the Bragg condition of the (0 0 2) reflection as a function of the interplanar distance $d_{(002)}$ .....	73
4.20	Bloch wave intensities for the two most important Bloch waves at the Bragg condition of the (1 0 0) reflection as a function of the interplanar distance $d_{(100)}$ .....	74
4.21	Bright field rocking curves at an accelerating voltage of 100KV and crystal thickness of 4000Å. a) (0 0 2) systematic case, b) (1 0 0) systematic case.....	78
4.22	Bright rocking curves at an accelerating voltage of 1000KV and crystal thickness of 8000Å. a) (0 0 2) systematic case, b) (1 0 0) systematic case.....	79
4.23	This figure shows a) the eigenvalues and b) the excitations amplitudes for Bloch waves 2 and 3 closed to the critical voltage. 13 beams from the (0 0 2) systematic set were taken into account and $\Delta\theta_g=0.0$ .....	82





5.1	Displacement vectors $\vec{R}$ in the hexagonal close packed lattice.....	90
5.2	TABLE 2.-Stacking fault phase angles $\alpha$ obtained using the HCP low order reflections (1 0 0), (0 0 2) and (1 -1 1).....	92
5.3	Stacking fault profile obtained when the (1 -1 1) reflection satisfies its Bragg condition and for a crystal thickness of 1710Å. The phase angle $\alpha=\pi/3$ .....	94
5.4	Stacking fault profile under the same conditions of the one in Fig. 5.3 but $\alpha=2\pi/3$ .....	95
5.5	Stacking fault profile under similar conditions to that in Fig. 5.3 but $\alpha=\pi$ .....	96
5.6	Two-dimensional displays of theoretical stacking faults obtained when (1 -1 1) reflection satisfies its Bragg condition in a wedge crystal and $\alpha=\pi/3$ .....	98
5.7	Two-dimensional display of a theoretical stacking fault obtained when the (1 -1 1) reflection satisfies its Bragg condition in a wedge crystal and $\alpha=2\pi/3$ .....	99
5.8	Two-dimensional display of a theoretical stacking fault obtained when the reflection (1 -1 1) satisfies its Bragg condition in a wedge crystal and $\alpha=\pi$ .....	100
5.9	Micrograph showing a bright field image of a stacking fault in a wedge crystal of HCP cobalt. The operating voltage was 150KV and $\Delta\theta_{(1-11)}=0.0$ .....	103
5.10	Micrograph showing a bright field image of a stacking fault in a wedge crystal of HCP cobalt. The operating voltage was 150KV and $\Delta\theta_{(1-11)}=0.0$ .....	104
6.1	Two possible structures for a twin boundary. a) the symmetrical boundary and b) the displaced boundary. The broken lines denotes the reflecting planes which give rise to common reflections.....	109



6.2	Schematic diagram showing a twin boundary in a specimen of total thickness $t$ . The twin boundary is shown in a configuration appropriate to the column approximation being made.....	113
6.3	Schematic diagram showing the diffraction pattern obtained from a twinned crystal such as the one shown in Fig. 6.2. The dotted lines indicates those reflections which are in the coupled set.....	116
6.4	Gratias and Portier dynamical matrix showing the sub-matrices associated with the dynamically coupled set of reflections.....	123
7.1	Schematic drawing of a wedge crystal. $\vec{k}$ is the incident wave vector, $\vec{n}$ is the surface normal and $\theta$ is the angle between $\vec{n}$ and the Brillouin zone boundary.....	135
7.2	Schematic drawing of the dispersion surface in the three beam approximation. The wave points obtained in the SL and NSL cases are indicated by the open and solid circles respectively.....	137
7.3	Excitation amplitudes $C^{-1}C_n$ plotted as a function of $\theta$ for silicon at the symmetry position of the systematic set. The circles correspond to $h=-g$ and the crosses to $h=g$ .....	139
7.4	Schematic drawing showing a cross section of a silicon whisker. The Bragg reflecting planes are $(0\ 2\ -2)$ . In this particular case the angle $\theta$ between the surface normal $\vec{n}$ and the Brillouin zone boundary is $60^\circ$ .....	142
7.5	a) Show the theoretical profile obtained by using the $-g=(0\ -2\ 2)$ reflection. Calculations were carried out for the NSL case. b) Show the experimental densitometer trace corresponding to a).....	144
7.6	a) Shows the theoretical profile obtained by using the $g=(0\ 2\ -2)$ reflection. Calculations were carried out for the NSL case. b) Shows the experimental densitometer trace corresponding to a).....	146



8.1	Experimental dark field of a stacking fault under weak beam diffraction conditions.....	153
8.2	Experimental densitometer trace obtained from a weak beam stacking fault image.....	154
8.3	Theoretical stacking fault profiles based on a) column and b) non-column approximations.....	156
8.4	Schematic diagram in reciprocal space showing the wave points associated with Bloch waves excited below the stacking fault in Fig. 8.5.....	161
8.5	Schematic diagram in real space showing a stacking fault in a crystal of thickness $t$ . $0$ is the origin of the coordinate system and $\vec{r}_e$ is a position vector terminating on the exit surface.....	163





## CHAPTER I

### INTRODUCTION

The electron microscope is one of the most important tools used in the study of the structure of materials. In order to interpret the experimental micrographs obtained from this instrument, a theoretical model which relates image contrast to specimen structure must be constructed. In order to obtain useful information, experimental micrographs must normally be compared to the results of theoretical calculations based on this model.

The theory involved in these calculations is normally the dynamical theory of electron diffraction. Although this theory will be described in detail in Chapter 2, for the present it is important to note that the interaction between the incident fast electrons and the crystal can be described by the Schrodinger wave equation. The wave functions are Bloch waves of the form:

$$b^{(i)} = \sum_{\vec{g}} C_g^{(i)} \exp[2\pi i (\vec{k} + \vec{g}) \cdot \vec{r}] \quad (1.1)$$

where  $\vec{g}$  is a reciprocal lattice vector,  $\vec{k}$  is a Bloch wave vector and  $C_g^{(i)}$  are the Bloch wave Fourier coefficients. In the Schrodinger equation the lattice potential is expressed as a Fourier series which can be written as:

$$V(\vec{r}) = \sum_{\vec{g}} V_g \exp [2\pi i \vec{g} \cdot \vec{r}] \quad (1.2)$$

where the  $V_g$ 's are the Fourier coefficients of the lattice potential.



In employing this theory many approximations must be made. The study of the validity of these approximations has become increasingly important in recent years because of the growing interest in obtaining higher resolution information from experimental micrographs. One of the major objectives of the electron microscopy group at the University of Alberta has been a theoretical and experimental study of these approximations. These studies involve, in the first instance, the development of more general forms of the theory in which the approximation being studied is not made. Assessments of diffraction conditions under which conventional forms of the theory might be expected to break down can then be made and experimental verification of these results carried out.

The work presented in this thesis is a continuation of this research. The theoretical approximations in the dynamical theory to be studied will be considered in detail in chapter 3 and at the beginning of each of the following chapters a detailed description of the objectives of the work to be described in this thesis will be presented.

In the remainder of this chapter a brief summary of the approximations to be studied will be given.

a) Many-beam approximation in single crystals.

The expression for the Bloch wave amplitude in equation 1.1 involves the sum over an infinite number of reciprocal lattice vectors  $\vec{g}$ . Therefore, when this Bloch wave function is substituted into the Schrodinger equation, an infinite



number of equations results (see chapter 2). In order to obtain numerical solutions, this infinite set of equations must be reduced to a finite set. This requires that a finite number of diffracted beams must be taken into account. Thus, for example, if only 2 beams are taken into account the well known two-beam approximation of the dynamical theory is obtained. However, practical experimental results indicate that when a high energy electron beam is incident on a crystal a relatively large number of reflections are always excited. Therefore, in practical situations the electron microscopist is always confronted with diffraction conditions which are quite different from that assumed in the two-beam dynamical approximation. It is consequently very important to carry out studies on the effects of higher order reflections on image contrast. In order to take these effects into account the many-beam approximation of the dynamical theory must be used.

One of the objectives of this thesis was the examination of these two approximations in perfect HCP crystals and HCP crystals containing stacking faults. In the perfect crystal case, a study of the effects of systematic reflections (see chapter 3) on the image contrast was carried out. In the stacking fault case, a study of the image contrast characteristics obtained under systematic reflections conditions was carried out. A possible method of identification of the nature of the different types of stacking faults in HCP structures is suggested.





b) Many-beam approximation in crystals containing grain boundaries

Interest in the image contrast exhibited by twin boundaries has been stimulated in recent years by the desire to determine body translation vectors in twinned crystals (see chapter 6 for a discussion of the meaning of this vector). The method used in the past has been of limited value since it was based on a theory which required the assumption that only common reflections are excited. This approximation neglects the effects of forbidden and non-common reflections in the twin (see chapter 3 and chapter 6 for a detailed discussion), with the result that significant errors in the measurements of body translation vectors might be obtained. Another objective of this thesis was therefore, the development of a general many-beam dynamical theory of twin boundary contrast including common, non-common and forbidden reflections (see chapter 3 and chapter 6).

c) Symmetrical Laue diffraction conditions.

Another important approximation which is commonly used in dynamical calculations of diffraction contrast is the assumption that the symmetrical Laue diffraction conditions prevail (see chapter 3 for more detailed discussion). In the symmetrical Laue case the reflecting planes are assumed to be perpendicular to the surface upon which the electron beam is incident. However, past theoretical investigations, (see Sheinin, et al. 1979), have predicted significant errors



when this approximation is made. Direct experimental evidence that these conditions do not necessarily provide an adequate description of image contrast has, however, not been reported. One of the objectives of this thesis was to obtain such evidence (see chapter 3).

d) Column approximation

Another important assumption in the dynamical theory which is used when theoretical calculations of the contrast exhibited in electron microscope images of lattice defects are carried out, is the so-called column approximation (see chapter 3 for detailed discussion). Theoretical calculations have predicted a breakdown of this assumption under particular diffraction conditions (see Jap, et al. 1981). However, direct experimental evidence of such a breakdown has not been previously presented in the literature. One of the objectives of this thesis was to present such an evidence.



## CHAPTER II

### THE DYNAMICAL THEORY OF ELECTRON DIFFRACTION

The dynamical theory of electron diffraction was first developed by Bethe (1928), who applied the Schrodinger equation to the problem of the scattering of fast electrons by the periodic potential of a crystal. There have been various approaches which have been used in formulating the equations of the dynamical theory. Thus, for example, Howie and Whelan (1961), developed a wave optical theoretical approach similar to the X-ray diffraction theory of Darwin (1914). A different wave optical model was developed by Cowley and Moodie (1957). They used the concept of transmission through a large number of crystal slices of very small thickness. The form of the theory which will be reviewed in this chapter is based on the approach given by Bethe (1928).

#### 2.1 REVIEW OF THE DYNAMICAL THEORY FOR PERFECT CRYSTALS

This theory starts with the Schrodinger equation with the periodic potential given by:

$$V(\vec{r}) = \sum_{\vec{g}} V_{\vec{g}} \exp [2\pi i \vec{g} \cdot \vec{r}] \quad (2.1)$$

The electron wave function within the crystal can be represented by a Bloch wave

$$\psi(\vec{k}, \vec{r}) = C(\vec{r}) \exp[2\pi i \vec{k} \cdot \vec{r}] \quad (2.2)$$

where  $C(\vec{r})$  is a periodic function in real space and



therefore can be expanded as a Fourier series to give:

$$b(\vec{k}, \vec{r}) = \sum_{\vec{g}} C_{\vec{g}} \exp[2\pi i (\vec{k} + \vec{g}) \cdot \vec{r}] \quad (2.3)$$

The  $C_{\vec{g}}$ 's are known as the Bloch wave coefficients. The constants in the Schrodinger equation can be collected together by defining a modified potential  $U(\vec{r})$  with Fourier coefficients

$$U_{\vec{g}} = \frac{2m_0 e}{h^2} V_{\vec{g}} \quad (2.4)$$

and a quantity  $K$  given by

$$K^2 = \frac{2m_0 e}{h^2} [E + V_0] \quad (2.5)$$

where  $E$  is the incident electron accelerating voltage and  $K$  is the magnitude of the mean electron wavevector in the crystal after allowing for refraction by the mean crystal potential. Substituting equations 2.1 and 2.3 in the Schrodinger equation and using 2.4 and 2.5 yields

$$\sum_{\vec{g}} \{ [K^2 - (\vec{h} + \vec{g})^2] C_{\vec{g}} + \sum_{\vec{h} \neq \vec{g}} U_{\vec{g}-\vec{h}} C_{\vec{h}} \} \exp[2\pi i (\vec{k} + \vec{g}) \cdot \vec{r}] = 0 \quad (2.6)$$

Equation 2.6 holds for all points in the crystal and therefore, the coefficients of each exponential term must be equal zero. Thus, we have the set of equations





$$[K^2 - (\vec{k} + \vec{g})^2] C_g + \sum_{h \neq g} U_{g-h} C_h = 0 \quad (2.7)$$

This expression gives one equation for each reciprocal lattice vector  $\vec{g}$  ( i. e. each diffracted beam ) considered. An exact solution of the set of equations represented by 2.7 can be obtained only if an infinite number of  $\vec{g}$  values is considered. In practice an approximate solution considering a finite number of diffracted beams,  $N$ , must, of course, be used.

The homogeneous set of equations 2.7, known as Bethe's dispersion equations, gives the relationship between the Bloch wave coefficients  $C_g$ , the Bloch wave vectors  $\vec{k}$  and the Fourier coefficients of the lattice potential  $U_g$ . This system of equations has a solution only if the determinant formed by the coefficients is equal to zero, i. e.

$$\begin{vmatrix} K^2 - k^2 & U_{-g} & \dots \\ U_g & K^2 - (\vec{k} + \vec{g})^2 & \dots \\ \dots & \dots & \dots \end{vmatrix} = 0 \quad (2.8)$$



The method which will be adopted in this thesis to solve 2.8, is based on the eigenvalue method. It is important to note that if we consider  $N$  diffracted beams, equation 2.8 will give rise to a polynomial in  $k$  of order  $2N$ . This expression would have  $2N$  roots,  $N$  of which are positive and  $N$  of which are negative corresponding to forward and backward propagation respectively. However, the high energy approximation (see, for example, Humphreys, 1979) can be used to reduce the degree of the polynomial obtained in 2.8 to  $N$ , rather than  $2N$ . As a result only those Bloch waves which propagate in the forward direction are taken into account, while those propagating in the backward direction are neglected. Thus in the two-beam case, for example, the high energy approximation gives:

$$K^2 - k^2 \cong 2K(K-k) \quad (2.9)$$

and

$$K^2 - (\vec{k} + \vec{g})^2 \cong 2K(K - |\vec{k} + \vec{g}|) \quad (2.10)$$

Inserting equations 2.9 and 2.10 in 2.8 yields

$$(K-k) (K - |\vec{k} + \vec{g}|) = U_g U_{-g} / 4K^2 \quad (2.11)$$

Equation 2.11 has two roots  $\vec{k}^{(1)}$  and  $\vec{k}^{(2)}$ , which are the Bloch wave vectors in the crystal for a given incident electron energy  $eE$ . The locus of the endpoints of the wave vectors  $\vec{k}^{(i)}$  satisfying equation 2.11 trace out branches of a surface of constant energy  $eE$  in  $k$  space which is known as



the dispersion surface. The manner in which the eigenvalue equation is derived can now be understood by considering Fig. 2.1. For simplicity only the two reciprocal lattice points  $O$  and  $\vec{g}$  have been included. In order to determine the Bloch wave vectors allowed within the crystal it is necessary to apply the boundary conditions at the entrance surface of the crystal. The boundary conditions require that the wave function and its derivative normal to the crystal surface should be continuous at the surface. Reflected waves from the surface can be ignored because of the large differences between the energy of the incident electrons and the lattice potential. To apply the boundary conditions it is necessary to take into account the inclination of the crystal surface with respect to the incident beam. However, in order to simplify the discussion it is normally assumed that the symmetrical Laue case holds. In the symmetrical Laue case, the entrance surface of the crystal is considered to be perpendicular to the reflecting lattice planes. Since Bragg angles are small in high energy electron diffraction, this also implies normal or near normal incidence. The boundary conditions can now be applied in Fig. 2.1 by drawing through the point  $T$ , a line perpendicular to the crystal surface. The intersections between this line and the branches of the dispersion surfaces are called wave points and determine the allowed Bloch wave vectors within the crystal. Now let  $\gamma$ , as shown in Fig. 2.1 be the distance of a possible wave point from  $T$ , and let  $s_g$  be the distance of





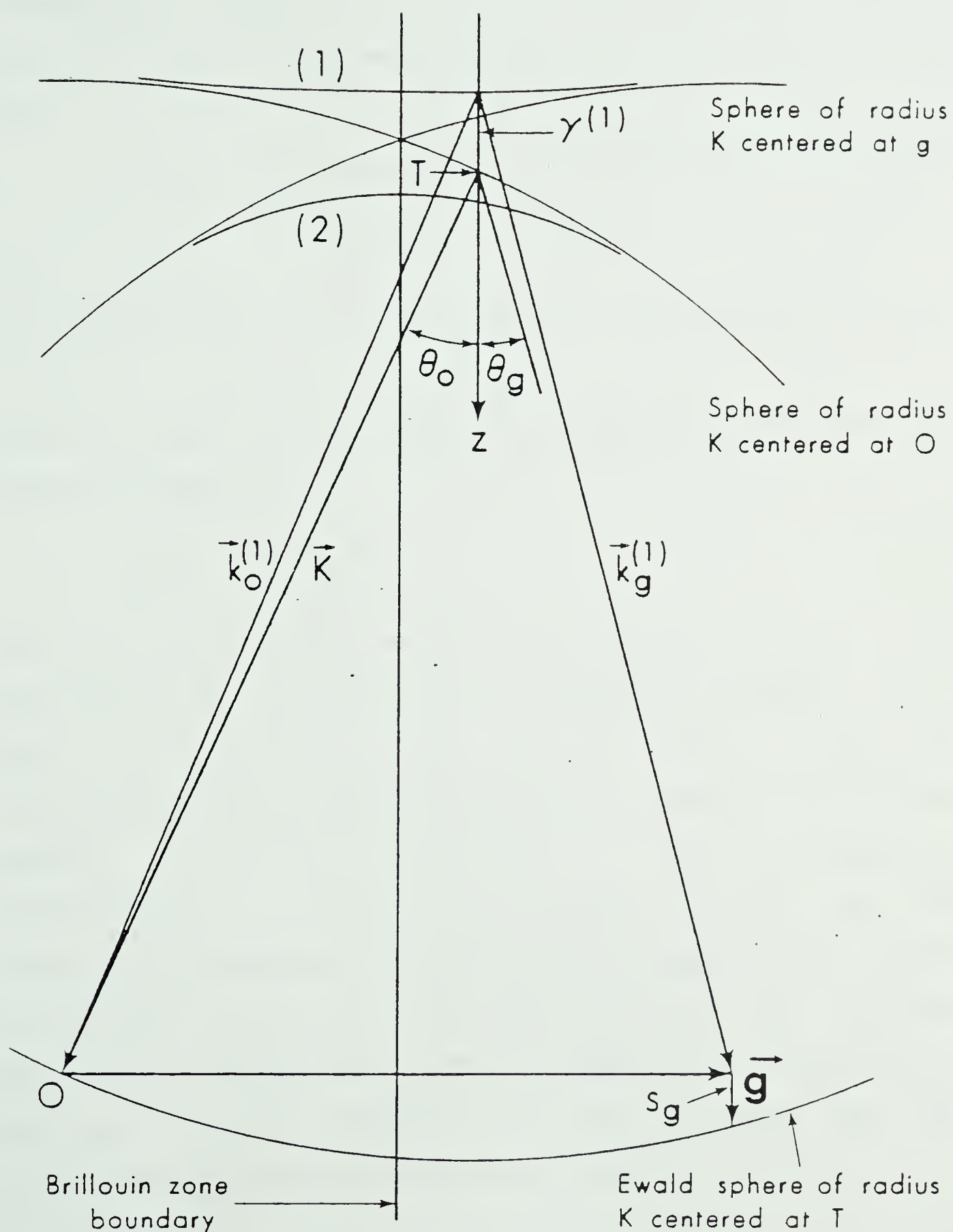


Figure 2.1 The dispersion surface and the Ewald sphere construction for high energy electrons.



the reciprocal lattice point  $\vec{g}$  from the Ewald sphere, measured in the direction normal to the reciprocal lattice vector  $\vec{g}$ . If it is also assumed that  $K \gg \gamma$  and  $K \gg (\gamma - s_g)$  then:

$$K^2 - k^2 \cong K^2 - [K + \gamma \cos \theta_o]^2 \cong -2K\gamma \cos \theta_o \quad (2.12)$$

and

$$K^2 - (\vec{k} + \vec{g})^2 \cong K^2 - [K - (\gamma - s_g) \cos \theta_g]^2 \cong 2K(s_g - \gamma) \cos \theta_g \quad (2.13)$$

Inserting equations 2.12 and 2.13 in equation 2.7 gives the eigenvalue equation:

$$\underline{A}\underline{C}^{(i)} = \gamma^{(i)}\underline{C}^{(i)} \quad (2.14)$$

Where  $\underline{C}^{(i)}$  is a column vector whose components  $C^{(i)}_g$  are the Bloch wave Fourier coefficients of equation 2.3 and  $\underline{A}$  is a matrix with elements  $A_{00}=0$ ,  $A_{gg}=s_g$  and  $A_{gh} = U_{g-h}/2K$  where  $g \neq h$ . Diagonalising the matrix  $\underline{A}$  using conventional methods yields the eigenvalues  $\gamma^{(i)}$  and corresponding eigenvectors  $\underline{C}^{(i)}$ . Since  $U(\vec{r})$  is real,  $U_g = U_{-g}^*$  and the matrix  $\underline{A}$  is therefore Hermitian. If the crystal has a center of symmetry, as will be the case for all the crystals considered in this thesis, and we choose this as the origin, then  $U_g = U_{-g}$ .  $\underline{A}$  is therefore real and symmetric and the eigenvalues and eigenvectors are all real.



## 2.2 CALCULATIONS OF THE DIFFRACTED BEAM INTENSITIES IN A PERFECT CRYSTAL

The total wave function  $\Psi(\vec{r})$  of the fast electron in the crystal can be written as a linear combination of all the Bloch waves excited:

$$\psi(\vec{r}) = \sum_i X^{(i)} b^{(i)} = \sum_i X^{(i)} \sum_g C_g^{(i)} \exp[2\pi i (\vec{k} + \vec{g}) \cdot \vec{r}] \quad (2.15)$$

where the coefficient  $X^{(i)}$  is the excitation coefficient of Bloch wave  $i$ . In order to calculate the directly transmitted ( $I_0$ ) or the diffracted beam intensity ( $I_g$ ), equation 2.15 can be decomposed into components in the directions of these beams. These components can be written as:

$$\phi_g(z) = \sum_i X^{(i)} C_g^{(i)} \exp[2\pi i (\vec{k} + \vec{g}) \cdot \vec{r}] \quad (2.16)$$

If these components are multiplied by the phase term  $\exp(-2\pi i \vec{K} \cdot \vec{r})$ , the intensity of the beam  $g$  at a thickness  $z$  in the crystal can be written as:

$$I_g(z) = |\phi_g(z)|^2 = \left| \sum_i X^{(i)} C_g^{(i)} \exp[2\pi i \gamma^{(i)} z] \right|^2 \quad (2.17)$$

Similar expressions can be written for the other diffracted beams. The excitation coefficients  $X^{(i)}$  can be calculated by imposing the boundary conditions at the entrance surface of the crystal i. e.  $\Phi_0(0)=1$ ,  $\Phi_g(0)=0$  if  $g \neq 0$ . Equation 2.16 together with these boundary conditions can be reduced to a matrix equation of the form



$$\underline{C}\underline{X} = \underline{\phi}(0) \quad (2.18)$$

where  $\underline{C}$  is a matrix having the elements  $C_{gi}^{(i)}$  in the  $g$ -row and  $i$ -column,  $\underline{X}$  is a column vector containing the excitation coefficients  $X^{(i)}$  and  $\underline{\phi}(0)$  is a column vector containing the diffracted beam amplitudes 1, 0, 0, ... at the entrance surface. Therefore, the excitation coefficients  $X^{(i)}$  can be obtained by solving the non-homogeneous set of linear equations 2.18. If the  $\underline{A}$  matrix in the eigenvalue equation 2.14 is real and symmetric, the matrix  $\underline{C}$  of normalized eigenvectors is orthogonal and  $\underline{C}^{-1} = \underline{C}^T$ , the transpose of  $\underline{C}$ . If equation 2.18 is multiplied from the left by  $\underline{C}^{-1}$  then

$$\underline{X} = \underline{C}^T \underline{\phi}(0) \quad (2.19)$$

and it immediately follows that the excitation coefficients  $X^{(i)}$  are given by the elements in the first row of  $\underline{C}$ , i. e.  $X^{(i)} = C_{o1}^{(i)}$ . The expression for the diffracted beam intensity therefore becomes:

$$I_g(z) = |\phi_g(z)|^2 = \left| \sum_i C_o^{(i)} C_g^{(i)} \exp[2\pi i \gamma^{(i)} z] \right|^2 \quad (2.20)$$

The diffracted beam amplitudes can be written in a matrix equation of the form:

$$\underline{\phi}_g(z) = \underline{C} \{ \exp[2\pi i \gamma^{(i)} z] \} \underline{X} \quad (2.21)$$

where the curly bracket indicates a diagonal matrix with elements equal to  $\exp(2\pi i \gamma^{(i)} z)$ . Substituting eq. 2.19 into





2.21 gives:

$$\underline{\phi}(z) = \underline{C} \{ \exp[2\pi i \gamma^{(i)} z] \} \underline{C}^{-1} \underline{\phi}_g(0) \quad (2.22)$$

Eq. 2.22 gives the diffracted beam amplitudes at a depth  $z$  in a perfect crystal in terms of  $\underline{\phi}(0)$ , the corresponding values at the entrance surface. This equation can be written in terms of the scattering matrix,  $\underline{P}(z)$ , as

$$\underline{\phi}_g(z) = \underline{P}(z) \underline{\phi}_g(0) \quad (2.23)$$

where  $\underline{P}(z) = \underline{C} \{ \exp(2\pi i \gamma^{(i)} z) \} \underline{C}^{-1}$ .  $\underline{P}(z)$ , the scattering matrix of the crystal relates the amplitudes of the different diffracted beams at a depth  $z$  in the crystal to the amplitudes at the entrance surface.

### 2.3 INELASTIC SCATTERING AND ABSORPTION

The theory developed in the previous sections considered only elastic scattering in a perfect crystal. However, the high energy electrons travelling through the crystal can also be inelastically scattered. Yoshioka (1957) formally showed that the effects of inelastic scattering could be taken into account by the addition of an imaginary part of the potential,  $iV(r)$ . Therefore, we can write:



$$V(\vec{r}) \rightarrow V(\vec{r}) + iV'(\vec{r})$$

$$V_g \rightarrow V_g + iV'_g$$

$$U_g \rightarrow U_g + iU'_g$$

(2.24)

If the potential in the Schrodinger equation is complex it follows that the Bloch wave vectors  $\vec{k}^{(i)}$  will also be complex i. e..

$$\vec{k}^{(i)} \rightarrow \vec{k}^{(i)} + iq^{(i)} \quad (2.25)$$

The total wavefunction of the incident electron within the crystal is therefore given by:

$$\psi(\vec{r}) = \sum_i X^{(i)} \sum_g C_g^{(i)} \exp[2\pi i(\vec{k}^{(i)} + \vec{g}) \cdot \vec{r}] \exp[-2\pi i\vec{q}^{(i)} \cdot \vec{r}] \quad (2.26)$$

In this thesis absorption coefficients will be calculated by using first order perturbation theory. The effect of the perturbation  $iV'(\vec{r})$  is to change the energy of the Bloch wave by an amount,  $e\Delta E$ , given by

$$e\Delta E = -i \int b^{(i)*} V'(\vec{r}) b^{(i)} d\tau \quad (2.27)$$

This change in energy can be related to a change  $\Delta k_z^{(i)}$  in the z-component of the Bloch wavevector  $\vec{k}^{(i)}$  by



$$\Delta k_z^{(i)} = \frac{me}{\hbar^2 k_z^{(i)}} \Delta E = -iq^{(i)} \quad (2.28)$$

The absorption coefficients  $q^{(i)}$  of Bloch wave  $b^{(i)}$  can then be obtained by evaluating the integral 2.27 to give

$$q^{(i)} = \frac{1}{2K_z} \sum_g \sum_h C_g^{(i)} C_h^{(i)} U_{g-h} \quad (2.29)$$

Including the effects of absorption in the elastic theory involves the replacement of each eigenvalue  $\gamma^{(i)}$  with  $\gamma^{(i)} + iq^{(i)}$ , where  $q^{(i)}$  is calculated by using the expression 2.29.

#### 2.4 THEORETICAL APPROACH TO CALCULATE THE STACKING FAULT IMAGE CONTRAST USING THE DYNAMICAL THEORY

Whelan and Hirsch (1957), have developed the form of the dynamical theory applicable to crystals containing stacking faults (for a description of a stacking fault in HCP materials see chapter 5). The faulted crystal arrangement is illustrated in Fig. 2.2, which shows a crystal made up of two slabs of thicknesses  $t_1$  and  $t_2$  of the same orientation but with a relative displacement  $R$  between them due to the presence of a stacking fault. The Bloch waves transmitted through such crystal are found by allowing the Bloch waves leaving slab 1 to be scattered again by slab 2. Using the scattering matrix approach, the total effect of both slabs can be obtained by multiplying the scattering matrices of the individual slabs of thicknesses  $t_1$  and  $t_2$ .





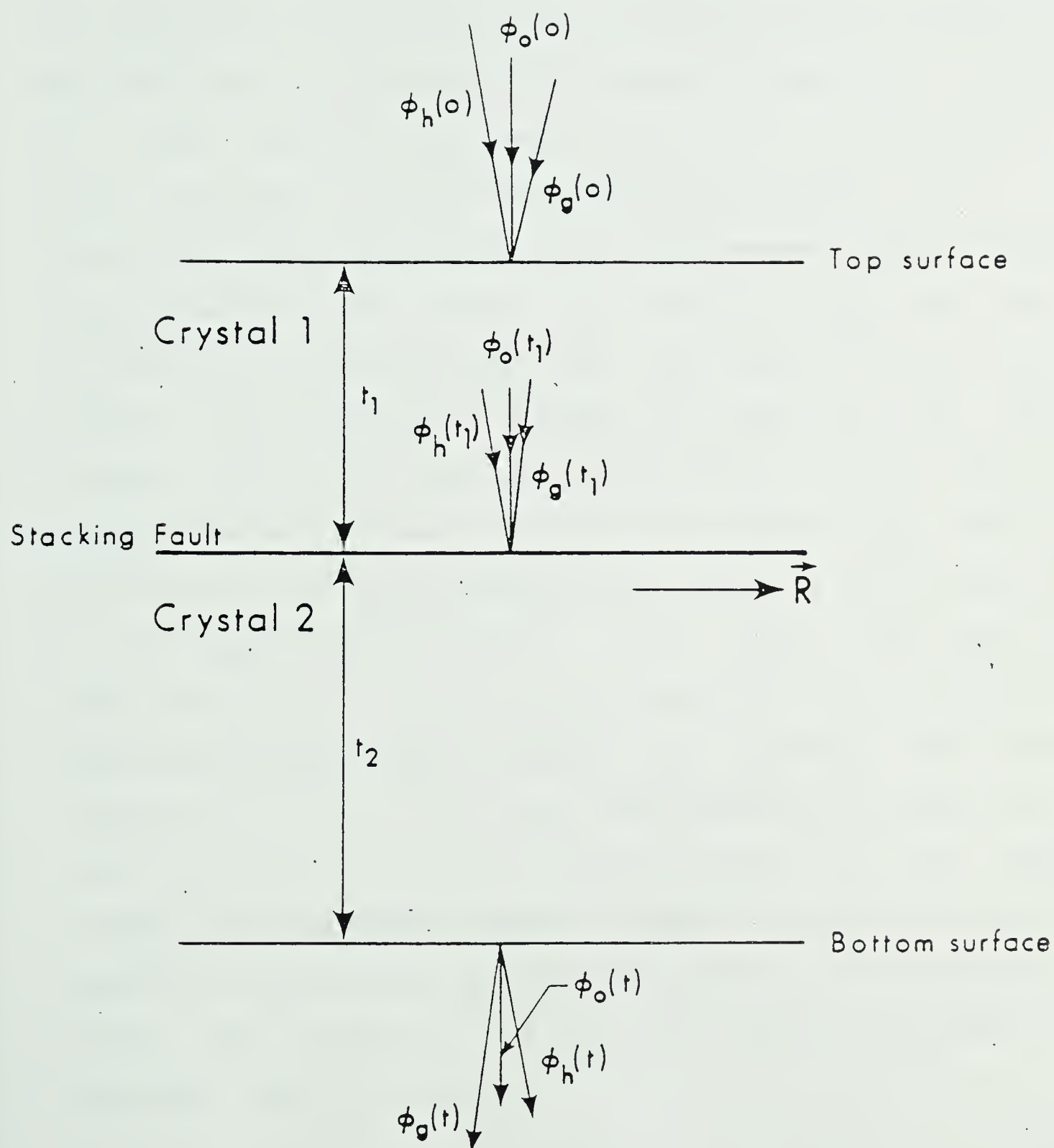


Figure 2.2 A crystal containing a stacking fault at a depth  $t_1$ , parallel to both surfaces of the crystal.  $\vec{R}$  is the displacement vector of the fault.



giving:

$$\phi_g(z) = \underline{P}(t_2) \phi_g(t_1) = \underline{P}(t_2) \underline{P}(t_1) \phi_g(0) \quad (2.30)$$

The amplitudes of the different diffracted waves incident on the fault are the same as for a perfect crystal of thickness  $t_1$ , where the scattering matrix  $\underline{P}(t_1)$  is given by equation 2.23. In order to calculate the scattering matrix  $\underline{P}(t_2)$  of the lower slab, the effect of the displacement of the lower crystal needs to be taken into account. This has been included by noticing that for any point  $\vec{r}$  in the lower crystal, the potential is the same as that of the upper crystal for an atom at a position  $(\vec{r}-\vec{R})$ . Thus to take the translation of the lower crystal into account, the lattice potential in the lower slab can be written as  $V(\vec{r}+\vec{R})$  where  $\vec{R}$  is the displacement vector. As a result, the Fourier coefficient  $U_{\vec{g}}$ , in the series expression for the lattice potential becomes  $U_{\vec{g}} \exp(-2\pi i \vec{g} \cdot \vec{R})$  and therefore the terms containing  $C_{\vec{g}}^{(i)}$ , are also multiplied by a phase factor given by  $\exp(2\pi i \vec{g} \cdot \vec{R})$ . Thus, the displacement  $\vec{R}$  will cause changes in the off-diagonal elements of the matrix  $\underline{A}$  in equation 2.14 and corresponding changes in the scattering matrix. The effects of  $\vec{R}$  can be taken into account by defining a matrix  $\underline{Q}$  given as:

$$\underline{Q} = \{\exp[2\pi i \vec{g} \cdot \vec{R}]\} \quad (2.31)$$

where the curly bracket indicates a diagonal matrix whose elements are  $\exp(-2\pi i \vec{g} \cdot \vec{R})$ . The scattering matrix  $\underline{P}$  in the



lower part of the crystal becomes  $\underline{Q}^{-1}\underline{PQ}$ , i. e.

$$\underline{P}(t_2) = \underline{Q}^{-1} \underline{C}\{\exp[2\pi i \gamma^{(i)} t_2]\} \underline{C}^{-1} \underline{Q} \quad (2.32)$$

The amplitudes of the diffracted beams at the bottom surface of the faulted crystal can then be written as:

$$\underline{\phi}(z) = \underline{Q}^{-1} \underline{C}\{\exp[2\pi i \gamma^{(i)} t_2]\} \underline{C}^{-1} \underline{QC} \{\exp[2\pi i \gamma^{(i)} t_1]\} \underline{C}^{-1} \underline{\phi}(0) \quad (2.33)$$

Effects of absorption can be included by replacing the eigenvalues  $\gamma^{(i)}$  by  $(\gamma^{(i)} + i q^{(i)})$ .

Equation 2.33 shows that if the fault lies at constant depth  $t_1$ , the intensity of the diffracted beams at the bottom surface will remain constant and consequently no contrast result. It is clear therefore that image contrast can only occur when  $t_1$  varies, i. e. for the case of a fault inclined to the surfaces of the crystal. The calculation of image contrast from an inclined stacking fault requires matching of the electron wave functions at the fault plane, which will involve the inclination of the fault to the crystal surfaces. This approach will be discussed in chapter 3 and chapter 8 of this thesis. However, another approach has been widely used in stacking fault image contrast calculations. This approximation assumes that each point on the inclined fault can be considered to correspond to a stacking fault at the same depth but lying parallel to both surfaces of the crystal in Fig. 2.2. This approximation was introduced by Whelan and Hirsch (1957), and is commonly referred to as column approximation (see chapter 3 for a



more detailed discussion).

## 2.5 INTERBRANCH AND INTRABRANCH DYNAMICAL SCATTERING FOR A STACKING FAULT

Some physical insight into the mechanisms producing stacking fault image contrast can be obtained by studying the dispersion surface representation for a crystal containing a stacking fault. Fig. 2.3 shows two branches of the dispersion surface for a crystal containing a stacking fault inclined to the surfaces of the crystal. In this figure  $\vec{n}_F$  represents the normal to the fault plane and  $\vec{n}$  the normal to the crystal surface upon which the electron beam is incident. In the upper part of the crystal, the incident electron beam excites two Bloch waves corresponding to the wave points  $D^1$  and  $D^2$ . These wave points are determined by the intersection of the normal  $\vec{n}$  to the top surface of the crystal with the two branches of the dispersion surface. When a Bloch wave encounters the stacking fault, correct wave matching (see Whelan and Hirsch, 1957), requires the excitation of additional wave points,  $D'^1$  and  $D'^2$ . The additional wave points are determined from the intersection of the normal of the fault  $\vec{n}_F$  with the two branches of the dispersion surface.

In order to examine stacking fault image contrast in terms of Bloch wave interactions, Hirsch et. al. (1977) considered the relationship between the excitation coefficients  $X^{(i)}$  above and below the fault. They found





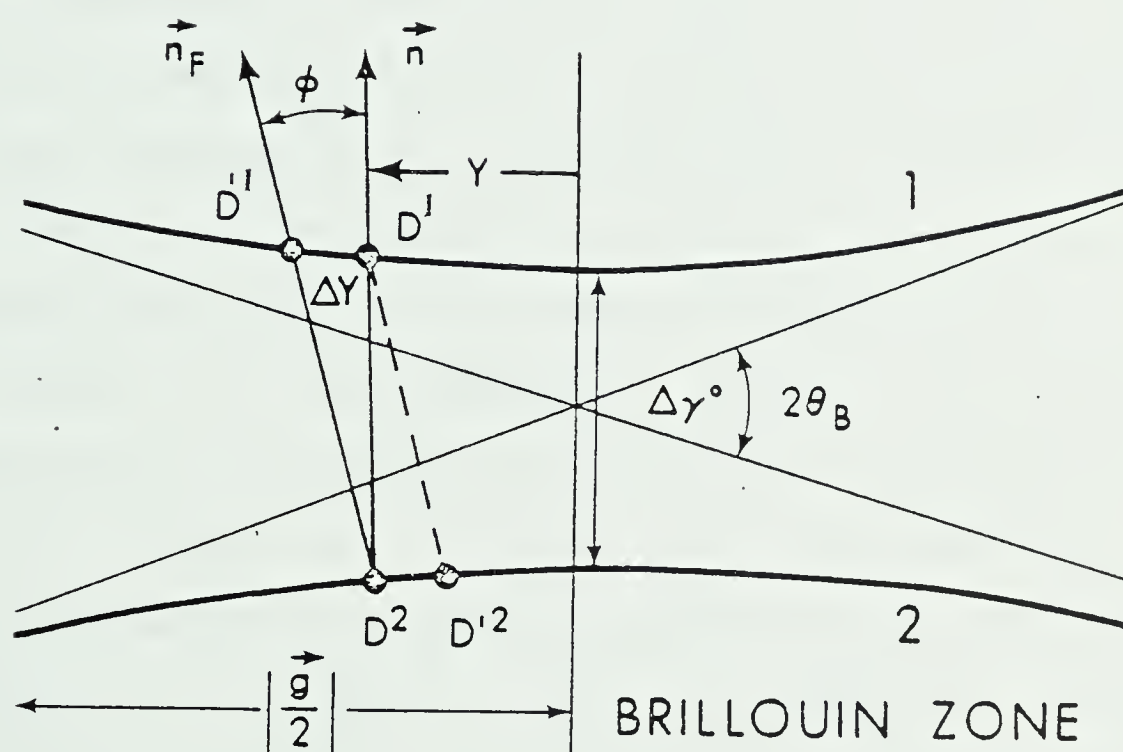


Figure 2.3 Two beam dispersion surface for a crystal containing a stacking fault inclined to the crystal surfaces.



that:

$$X'^{(1)} = (C_o^{(1)^2} + C_g^{(1)^2} e^{i\alpha}) X^{(1)} + C_o^{(1)} C_o^{(2)} (1 - e^{i\alpha}) * e^{2\pi i \Delta \gamma t_1} e^{-2\pi i \Delta q t_1} X^{(2)} \quad (2.34)$$

and

$$X'^{(2)} = (C_o^{(2)^2} + C_g^{(2)^2} e^{i\alpha}) X^{(2)} + C_o^{(1)} C_o^{(2)} (1 - e^{i\alpha}) * e^{-2\pi i \Delta \gamma t_1} e^{i\pi \Delta q t_1} X^{(1)} \quad (2.35)$$

where  $X'^{(i)}$  represents the excitation coefficients below the fault,  $\Delta\gamma = \gamma^{(1)} - \gamma^{(2)}$ ,  $\Delta q = q^{(1)} - q^{(2)}$  and  $t_1$  is the depth of the fault in the crystal. The above equations show that the excitation coefficient  $X'^{(1)}$  is made up of two parts. The first part depends on  $X^{(1)}$ , the previous excitation on the same branch of the dispersion surface. This is referred as intrabranh scattering since the wavevector stays on the same branch of the dispersion surface. The second part depends on  $X^{(2)}$ , the previous excitation on the other branch of the dispersion surface and is therefore called interbranch scattering. It corresponds to part of  $X^{(2)}$  being scattered to branch 1 with a wavevector change of  $\vec{\Delta k} = \vec{k}^{(2)} - \vec{k}^{(1)}$ . A similar interpretation can be placed on equation 2.35, except that in this case scattering occurs from branch 1 to branch 2. Stacking fault contrast in this picture arises from the interaction of Bloch waves associated with the different wave points  $D^1$ ,  $D^2$ ,  $D'^1$  and  $D'^2$ . It is important to note, however, that if the stacking fault is parallel to the crystal surfaces the wave points  $D^{(i)}$  coincide with  $D'^{(i)}$ .



The many-beam expressions which allow the extension of this analysis to the case where more than two Bloch waves are important have been derived by Sheinin and Botros (1972). In their many-beam theory, the diffracted beam amplitude for a crystal containing a stacking fault at a depth  $t_1$ , can be written as:

$$\phi_g = \sum_i \sum_j \phi_g^{ij} \quad (2.36)$$

where

$$\phi_g^{ij} = C_g^{(i)} C_o^{(j)} B^{ij} \exp[-2\pi i \vec{g} \cdot \vec{R}] \exp(2\pi i \gamma^{(i)} z) \quad (2.37)$$

and

$$B^{ij} = \exp 2\pi i (\gamma^{(j)} - \gamma^{(i)}) t_1 \sum_g C_g^{(i)} C_g^{(j)} \exp[2\pi i \vec{g} \cdot \vec{R}] \quad (2.38)$$

The summations  $i$  and  $j$  are from 1 to  $N$ , where  $N$  is the number of beams taken into account in a particular calculation and the summation  $g$  is over all the reciprocal lattice vectors corresponding to the reflections included in the calculation. The elements  $\Phi^{ij}$  represent interbranch scattering from Bloch wave  $b^{(j)}$  to Bloch wave  $b^{(i)}$ . On the other hand,  $\Phi^{ii}$  represents scattering of Bloch wave  $b^{(i)}$  into itself and is referred to as intrabranch scattering. It is important to note from equation 2.38 that stacking fault contrast arises from interbranch scattering only. This can be seen from the fact that the intrabranch contributions  $\Phi^{ii}$  are independent of  $t_1$ , the depth of the fault in the crystal. It is also important to point out that the





contributions  $\Phi^{ij}$  to the diffracted beam amplitude are complex in nature and therefore phase amplitude diagrams are useful in understanding the effects of these quantities on image contrast.



## CHAPTER III

### APPROXIMATIONS INVOLVED IN THE DYNAMICAL THEORY OF ELECTRON DIFFRACTION AND OBJECTIVES OF THE PRESENT WORK

#### 3.1 INTRODUCTION

In the last chapter the dynamical theory for perfect crystals and crystals containing stacking faults was given. It was indicated that when this theory is applied in practice a number of approximations are made. In this chapter the approximations to be studied in this thesis will be reviewed.

#### 3.2 THE MANY-BEAM APPROXIMATION

In the many-beam approximation of the dynamical theory the number of beams included in a calculation must be reduced to a finite number  $N$ . In most cases, when diffraction contrast is discussed in the literature, it is assumed that either two beams or only systematic reflections are excited. Systematic reflections correspond to diffracted beams with reciprocal vectors equal to  $\vec{n}g$  where  $n=0, \pm 1, \pm 2, \dots$  (see Fig. 3.1) while other reflections are called non-systematic reflections (see Fig. 3.2). The use of goniometer stages have permitted electron microscopists to orient their specimens so that the effects of non-systematic reflections can be minimized and under these circumstances it can, therefore, be assumed that the only strongly excited low-order reflections lie along the systematic row. When the





Figure 3.1 An experimental diffraction pattern obtained under systematic reflection conditions in HCP cobalt



lowest order reflection,  $g$ , in a systematic set is strongly excited, the number of beams included in the many-beam approximation can be reduced to two and therefore the two-beam approximation of the dynamical theory is obtained.

### 3.2.1 The many-beam approximation in perfect HCP crystals.

The effects of systematic reflections on the diffraction contrast exhibited by perfect and defected FCC crystals have received considerable attention in the literature. It is interesting to note, however, that in the previous studies of many-beam effects, relatively little attention has been paid to hexagonal materials even though some of the more common metals have this crystalline structure. Serneels and Gevers (1969) in their paper on systematic reflections in electron diffraction have compared theoretical extinction distances for different reflections in Zn and Serneels et al. (1971) have carried out theoretical studies under particular diffraction conditions. Some HCP materials have been included in their studies. In particular, they carried out diffracted beam intensity calculations for different systematic reflections and different electron accelerating potentials in HCP cobalt. Jones (1978), carried out the first experimental investigation on the effects of systematic reflections in HCP materials. He studied the behavior of bend contours as a function of the electron energy for different types of HCP materials. He introduced a classification of systematic sets





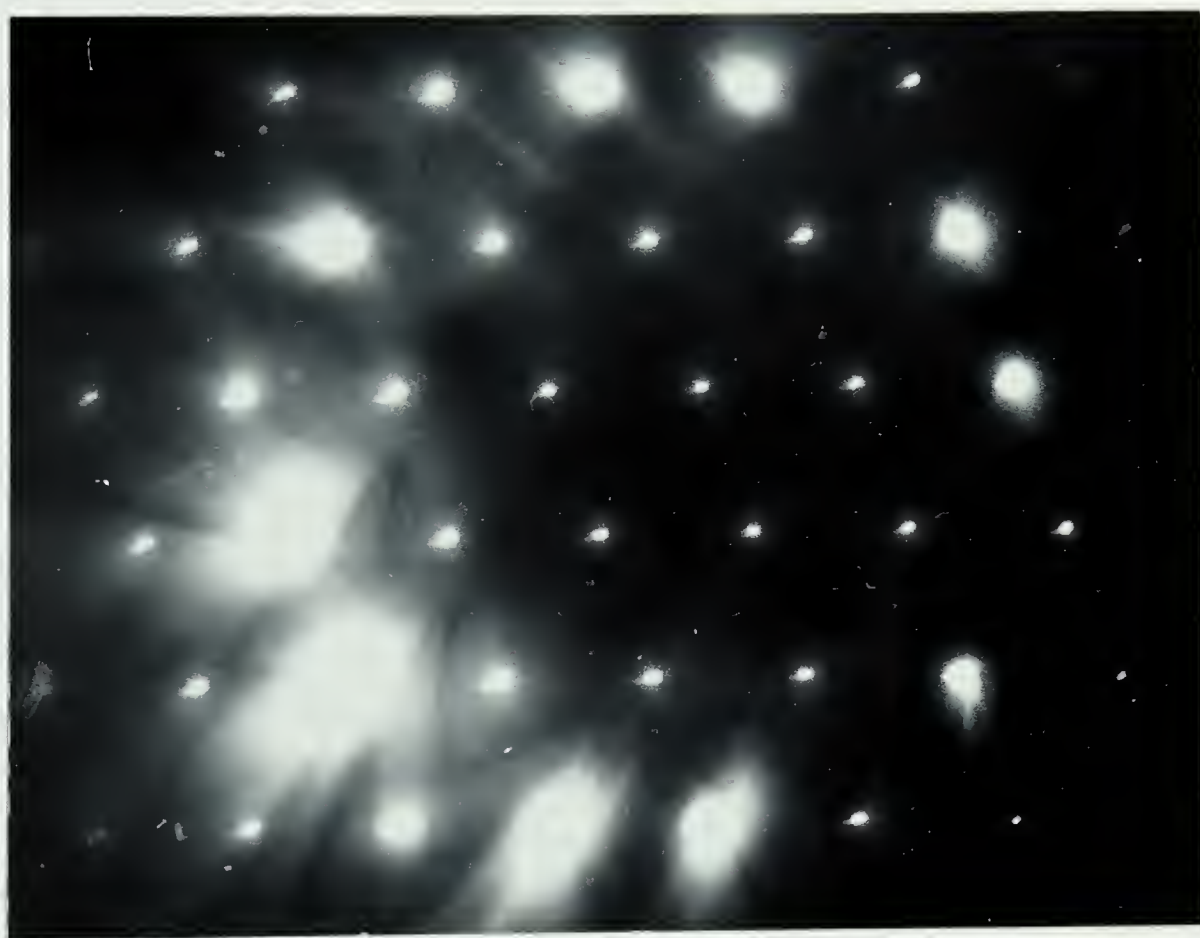


Figure 3.2 A portion of a typical diffraction pattern in the non-systematic case. Many diffracted beams are important and must be taken into account in calculating the  $A$  matrix of the dynamical theory.



of reflections in HCP structures based on the magnitude of the structure factor for the lowest order reflection in each set (see chapter 4). His results indicated that some types of systematic reflections have transmission properties similar to the transmission properties of systematic sets in FCC and BCC materials. However, there are some systematic sets whose transmission properties are very unusual.

Studies of the variation of extinction distance with deviation from the Bragg condition have provided considerable insight into effects of systematic reflections in FCC materials (see for example, Sheinin 1967, Sheinin 1970.). However similar studies in hexagonal materials have not previously been carried out. One of the objectives of this thesis has, therefore, been to study the effects of systematic reflections on the electron microscope images of perfect HCP crystals by adopting this approach (see chapter 4 for detailed discussion).

### 3.2.2 The many-beam approximation in HCP crystals containing stacking faults.

The effects of systematic reflections have also been extensively studied in FCC materials which contain stacking faults (see for example, Humphreys et. al. 1967, Sheinin et. al 1972, Botros et. al 1975.). As a result of these investigations methods which permit a determination of the nature of the two possible types of stacking faults found in FCC structures, (Hirsch et. al. 1977, Gevers et. al. 1963.),



have been developed. Unlike FCC materials, stacking faults in HCP structures are of three different types. Therefore, the question as to whether or not the commonly used methods to identify stacking faults in FCC materials can be used in HCP structures remains. One of the objectives of this thesis has been to investigate this question by studying the image characteristics of stacking faults in HCP cobalt (see chapter 5 for detailed discussion).

### 3.2.3 The many-beam approximation in crystals containing twin boundaries.

The geometry of the electron diffraction patterns from crystals containing twin boundaries is in general more complex than the perfect crystal case or crystals containing defects such as stacking faults or dislocations, (see for example, Hirsch et. al 1977). In the case of an overlapping matrix and twin such as the one shown in Fig. 3.3a, three types of reflections can arise. These are non-common reflections which arise from sets of lattice planes which are either in the matrix or the twin, forbidden reflections which arise when a diffracted beam from the matrix is diffracted again by the twin and common reflections which arise from families of crystal planes which are continuous accross the twin boundary (or displaced by a fraction of a lattice vector as a result of the presence of a rigid body translation, see Fig. 3.3b and Fig. 6.1 in chapter 6). In order to calculate the intensities of the diffracted beams



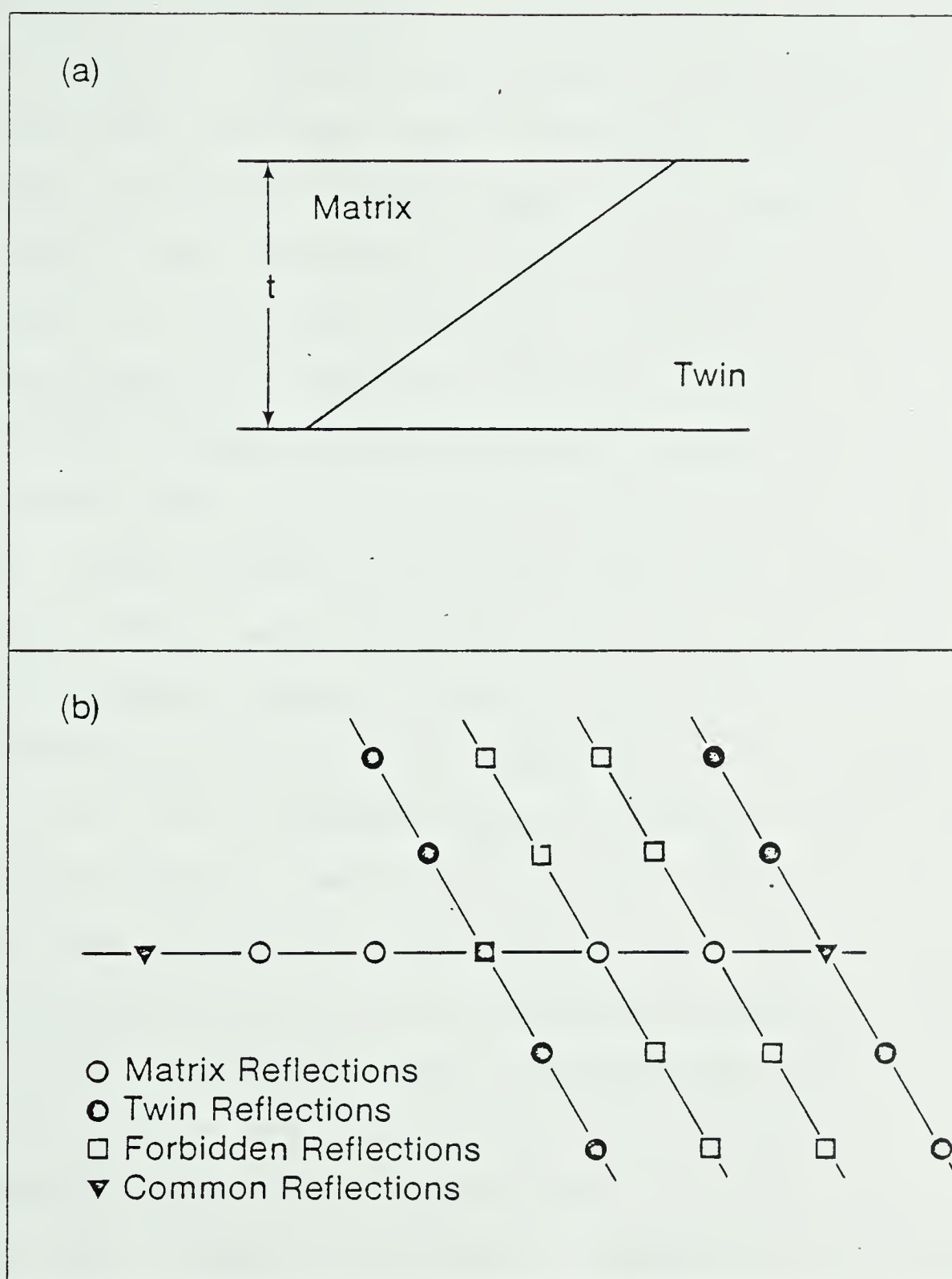


Figure 3.3 a) Illustration showing a twin boundary inclined to the surface of a specimen of thickness  $t$ . b) Schematic diffraction pattern obtained from a twin boundary such as the one shown in a).





obtained from twinned crystals, the dynamical theory of electron diffraction must be employed. The description of the electron scattering processes by the dynamical theory gives rise to the well known dynamical coupling phenomena between diffracted beams (see, for example, Hirsch et al. 1977). When the dynamical theory is applied to a perfect crystal or crystals containing dislocations or stacking faults, there is dynamical coupling between all of the diffracted beams excited. However in a twinned crystal this is not the case (see for example Sheinin et al. 1976). Thus, when common reflections are not taken into account, Sheinin et al. (1976), have shown that dynamical coupling can only occur between those diffracted beams which originate from the same matrix reflection. Therefore, if for example, there is only one diffracted beam intensity of interest, the reflections which need to be taken into account in a many-beam dynamical calculation, are those which are dynamically coupled to this particular diffracted beam. It is clear, therefore, that the many-beam dynamical theory applied in the past to crystals containing defects such as stacking faults and dislocations can not be used in this case. As a result a different approach is required to develop a many-beam form of the dynamical theory for twinned crystals.

The first analyses of the twin boundary problem have been based on the two-beam approximation of the dynamical theory (see for example Van Landuyt et al. 1965, Marukawa



1977, and Pond et. al. 1976). However, this approximation has limited applicability since it requires that the same reflection be considered in both matrix and twin (i. e. only common reflections can be taken into account). In practice, however, the specimen will be so oriented that different reflections in the twin and matrix are excited. It is, therefore, clearly desirable to develop a many-beam form of the dynamical theory for the twin boundary case. The first many-beam theory for twin boundary contrast has been developed by Sheinin and Corbett (1976). In this theory, both non-common and forbidden reflections were considered. Recently, Sutton and Pond (1978), and Gratias and Portier (1980), have developed general many-beam forms of the dynamical theory for twin boundaries which include the effects of common, non-common and forbidden reflections. The method of Sutton and Pond (1978), has been criticized in the literature from a number of points of view (see for example, Gomez et. al 1980, Gratias et. al. 1980.). Thus, the question as to whether or not these two forms of the theory are equivalent or in fact, whether one form is correct while the other is incorrect remains. A many-beam form of the dynamical theory of twin boundary contrast including effects of common reflections and based on a Bloch wave approach has not been presented in the literature. Therefore, another of the objectives of this thesis was to derive a form of the dynamical theory applicable to this case and based on this approach. These results were compared with the methods of



Sutton and Pond (1978), and Gratias and Portier (1980). (see chapter 6)

### 3.3 SYMMETRICAL LAUE DIFFRACTION CONDITIONS

Another approximation normally made in many-beam dynamical theory calculations is that the symmetrical Laue diffraction conditions prevail. The symmetrical Laue case in electron diffraction assumes that the reflecting lattice planes are perpendicular to the surface of the specimen upon which the electron beam is incident (see Fig. 3.4). Past investigations, (see for example, Whelan et al. 1957, Saldin et al. 1978, Sheinin et al. 1979 ) concerning the assessment of the validity of the assumption that these diffraction conditions prevail have predicted errors when certain conditions are met. Thus, for example, Saldin et al. (1978) found that for a range of angles of inclinations of the crystal surface up to about  $70^\circ$ , the errors involved in assuming symmetrical Laue conditions are less than 5%. Sheinin and Jap (1979), carried out an analysis of the validity of assuming symmetrical Laue diffraction conditions based on the Bloch wave formulation of the dynamical theory. Their method was similar to that developed by Spencer and Humphreys (1971), who solved the equation of the crystal surface normal in the k-space and the many-beam dynamical equations simultaneously. The results obtained from the Sheinin and Jap (1979) investigation showed clearly that for certain diffraction conditions the assumption of symmetrical





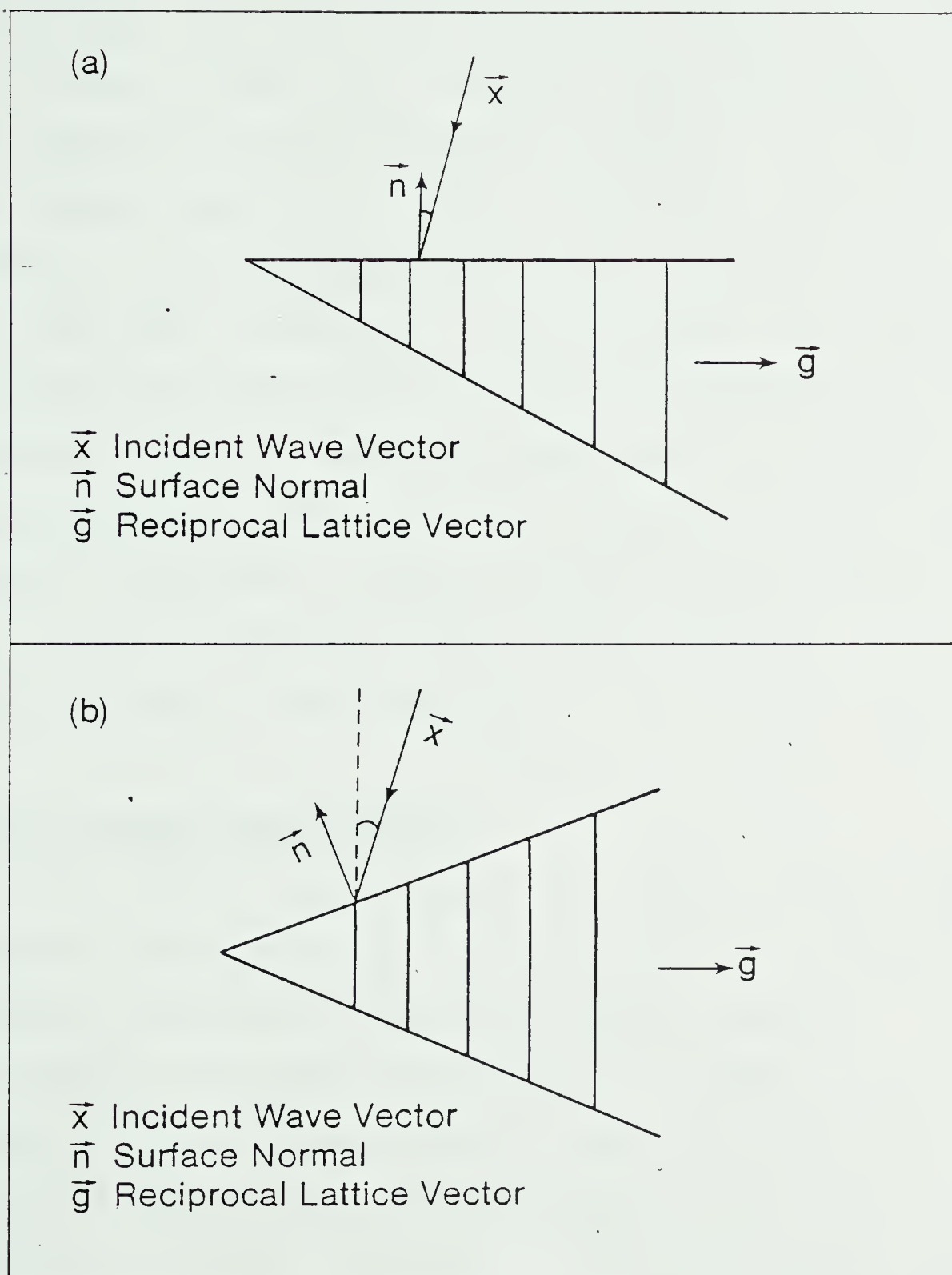


Figure 3.4 Schematic drawings of a crystal under: a) symmetrical Laue diffraction conditions. b) non-symmetrical Laue diffraction conditions.





Laue diffraction conditions can result in significant errors in diffracted beam intensities and theoretical lattice defect images even for relatively small angles of tilt of the surface. Thus, for example, they found that for weak beam diffraction conditions and an angle of inclination of the crystal surface of  $30^\circ$ , significant differences in symmetrical and non-symmetrical Laue dislocation profiles were obtained. Therefore, on the basis of theoretical considerations there seems to be strong evidence that the widespread use of symmetrical Laue conditions can give rise to serious errors. However, there has been no experimental evidence presented in the literature which supports this view. Another objective of this thesis has been to provide such an evidence. (see chapter 7)

### 3.4 THE COLUMN APPROXIMATION

The column approximation has been widely used in dynamical theory calculations of the contrast exhibited in electron microscope images of lattice defects. In this approximation the imperfect crystal is divided into narrow columns with the length of each column being parallel to the incident electron beam. The displacement in a given column produced by a lattice defect is assumed to vary along the length of the column, defined usually as the  $z$ -direction. The basic assumption of the column approximation is that each column may be chosen sufficiently narrow so that the displacement within it is only a function of  $z$  and



sufficiently wide so that an electron entering at the top of the column is not scattered out of the column during its passage through the crystal. Therefore, the electron wave function at the bottom surface of such a column is the same as that at the lower surface of a crystal with the same specimen thickness but with infinite lateral extension.

Previous assessments of the validity of assuming the column approximation have predicted errors when certain conditions are met, (see for example, Howie et. al. 1968, Jouffrey et. al 1967, Howie et. al. 1970). In these investigations the formal treatment of the non-column case gives rise to a set of simultaneous partial differential equations, which can be analytically solved when only two beams are taken into account. It is important to mention that all of these previous investigations of the column approximation were concerned with dislocation images. The first theoretical investigation of the validity of the column approximation in the case of stacking faults was carried out by Jap and Sheinin (1981). The results obtained showed that the validity domain of the column approximation for a particular stacking fault inclination decreased with increasing deviation from the Bragg condition and increases with increasing electron energy. Comparisons between many-beam stacking fault profiles in the non-column and column case showed that significant differences can be obtained for weak beam diffraction conditions even when the stacking fault inclination is less than  $45^\circ$ . Thus based in



these theoretical considerations there seems to be strong evidence that the use of the column approximation in the stacking fault or dislocation image contrast calculations can give rise to serious errors. However, there has been no experimental evidence which supports this view. Another objective of this thesis has been to provide such evidence (see chapter 8).



## CHAPTER IV

### EFFECTS OF SYSTEMATIC REFLECTIONS ON DIFFRACTION CONTRAST IN HCP COBALT

#### 4.1 INTRODUCTION

The HCP structure differs from FCC and BCC structures in two important respects. Firstly, the primitive cell of the HCP lattice contains two atoms, whereas the primitive cells of FCC and BCC lattices contain one atom only. The second important difference between HCP and these cubic lattices is that the hexagonal structure does not have a centre of symmetry at an atomic site. There is, however, a centre of symmetry at a position half-way between the two atoms in the unit cell. One of the consequences of there being two atoms in the HCP primitive cell is that the non-zero values of the structure factor  $F_g$  vary from reflection to reflection, rather than always remains constant, as for FCC and BCC crystals. In the case of HCP structures, the two atoms in the primitive cell are in the positions:  $(0\ 0\ 0)$  and  $(1/3\ 2/3\ 1/2)$ , therefore the ratio between  $F_g$  and  $f$ , the atomic scattering amplitude can be written as:

$$\frac{F_g}{f} = 2 \cos \pi \left( \frac{2(h+2k)+3l}{6} \right) \quad (4.1)$$

Using this expression the reflections in HCP structures can





be classified as shown in Fig. 4.1 (see Bonnet, 1976 and Jones 1978). It is important to mention that the values of  $|F_g / f|$  vary with the order of the reflection as is illustrated in Fig. 4.2. Jones (1978), has indicated that although there are 4 different types of reflections, only 3 different types of systematic rows of reflections are obtained. This can be understood by comparing Fig. 4.2a, d, which indicates that reflections of the type  $2n\vec{g}$  ( $n$  integer) in Class 3 are similar to reflections of the type  $n\vec{g}$  in Class 0. This is because when  $|F_g / f|=0$ , the reflection is forbidden and for those sets in Class 3, these reflections can not appear in the systematic row. Therefore a systematic row of class 3 reflections will have the elements  $0, \pm 2\vec{g}, \pm 4\vec{g}, \dots$  as a result will be equivalent to those rows in Class 0.

The work presented in this chapter explores the effects that HCP systematic reflections have on the thickness extinction contours. Three different systematic sets have been chosen  $((1\ 0\ 0), (0\ 0\ 2)$  and  $(1\ -1\ 1))$ . Each of these systematic sets of reflections is in one of the three different groups obtained by Jones (1978) in HCP structures. The  $(0\ 0\ 2)$  systematic set is in Class 0, the  $(1\ -1\ 1)$  systematic set in Class 1 and finally the  $(1\ 0\ 0)$  systematic set in Class 2. They are also the most commonly appearing low order systematic sets in electron diffraction patterns of HCP specimens in the electron microscope. This chapter has been divided into five major sections 4.2, 4.3, 4.4, 4.5



CLASS	$F_g / f$	EXAMPLES
0	2	(002), (1-22), (2-10), ..
1	$\sqrt{3}$	(1-1 1), (0 1 -1), (1-1 3), ..
2	1	(1 0 0), (0 1 2), (2 1 0), ..
3	0	(2 -1 1), (1 1 -1), (111), ..

Figure 4.1 TABLE 1.-Ratio of the structure factor to the atomic scattering amplitude for the first order reflections.



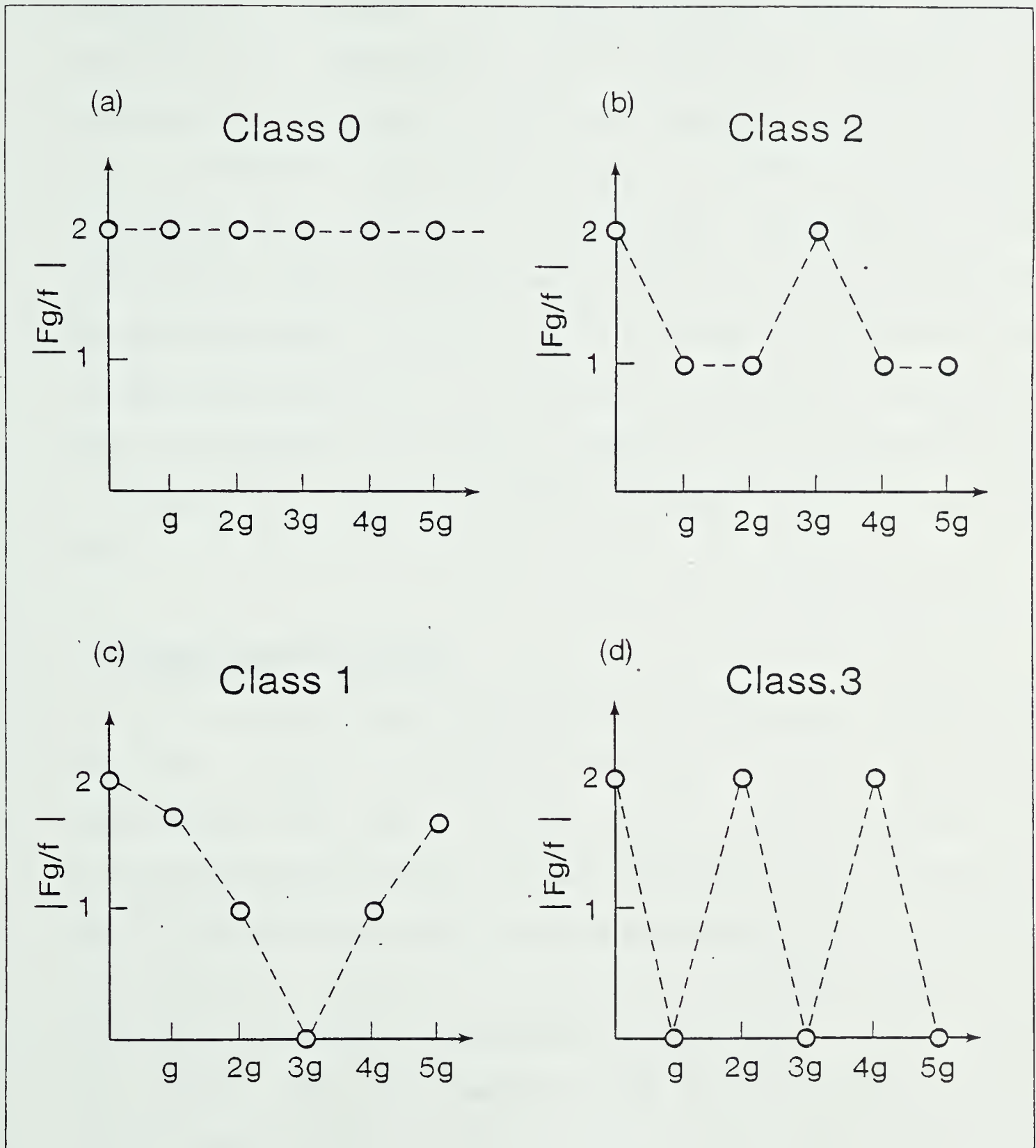


Figure 4.2 Ratio of the structure factor to the atomic scattering amplitude for Class 0, 1, 2 and 3, as a function of the order of the reflection.



and 4.6. Section 4.2 is devoted to a description of the experimental methods used in the present study of thickness fringes. In section 4.3, experimental results and the results of theoretical calculations are compared. An analysis of this work in terms of Bloch wave parameters is also carried out. Section 4.4 deals with the effects of HCP systematic reflections on anomalous absorption. Beam penetration characteristics as a function of the orientation is also discussed. In section 4.5 an analysis is carried out on the relationship of the effects of systematic reflections and the acceleration voltage. Section 4.6 is concerned with a discussion of the results obtained in sections 4.3 and 4.4.

#### 4.2 EXPERIMENTAL METHOD

In order to study the effects of systematic reflections on the image contrast obtained in HCP materials, measurements have been carried out of the variation of extinction distance with crystal orientation. The systematic sets of reflections used for this experimental investigation were the  $(1\ 0\ 0)$ ,  $(1\ -1\ 1)$  and  $(0\ 0\ 2)$  in HCP cobalt. The electron microscope accelerating voltage used in this work was 150KV. The experimental method can be divided in three parts: specimen preparation, electron microscope examination and analysis of experimental results.





#### 4.2.1 SPECIMEN PREPARATION

Cobalt was chosen as the material to be investigated. Cobalt is stable as a HCP structure below 417 °C (Bibby et. al. 1963.), whereas above this temperature the FCC structure is stable. Previous work (see for example, Troiano et. al. 1948, Edwards et. al. 1943.), has shown that the phase transformation at the above mentioned temperature is martensitic in type. The heat treatment used for obtaining a high proportion of the low temperature HCP phase at room temperature was to anneal the specimens for about 24 hrs. at 800° and then to cool it very slowly ( $\approx 5^{\circ}\text{C}/\text{min}$ ). The electron microscope observations were carried out using annealed specimen discs of cobalt (3mm in diameter). These specimens were polished following a method developed by K. Z. Botros (1973). They were first jet polished and finally using an electrolytic polishing system they were made ready for observation.

#### 4.2.2 ELECTRON MICROSCOPE EXAMINATION

The specimens were examined in a JEM 150 electron microscope equipped with a tilting-rotating stage which permitted the orientation of the specimen with respect to the electron beam to be varied. This stage can be used to tilt the specimen about two mutually perpendicular axes through an angular range of  $\pm 10^{\circ}$  and  $\pm 5^{\circ}$  respectively. The specimen can also be rotated through  $360^{\circ}$ . In order to tilt through a known angle a high precision click-type control



which permitted the angle of tilt to be changed in increments of  $0.005^\circ$  was used. In order to test the accuracy of this stage two different methods developed by Sheinin (1966) and Cann (1967), were used. It was found that the angles of tilt as given by the tilt control were within 10% of those determined by the above mentioned methods.

In order to measure the extinction distances  $\xi$  from electron microscope images of wedge-shaped crystals (see Fig. 4.3), it is first necessary to choose and orient a suitable specimen. Then a series of electron micrographs must be taken as the specimen is systematically tilted over a given range of  $\Delta\theta_g$ . In order to determine whether the crystal is FCC or HCP and also in order to obtain the precise orientation of the crystalline area the following method has been used. A symmetrical diffraction pattern from the area concerned was first recorded. From these patterns, values of the distances  $R$  from the different low-order diffraction spots to the directly transmitted beam were measured. Using these values of  $R$  and the camera constant  $L$  which was independently obtained using a standard of gold, the corresponding lattice planes spacing,  $d_{hkl}$  were obtained. The ratios of these spacings were then compared to the theoretically calculated ratios. Using this procedure it was possible to index the diffraction pattern and to identify the crystalline phase in the area of the specimen concerned.



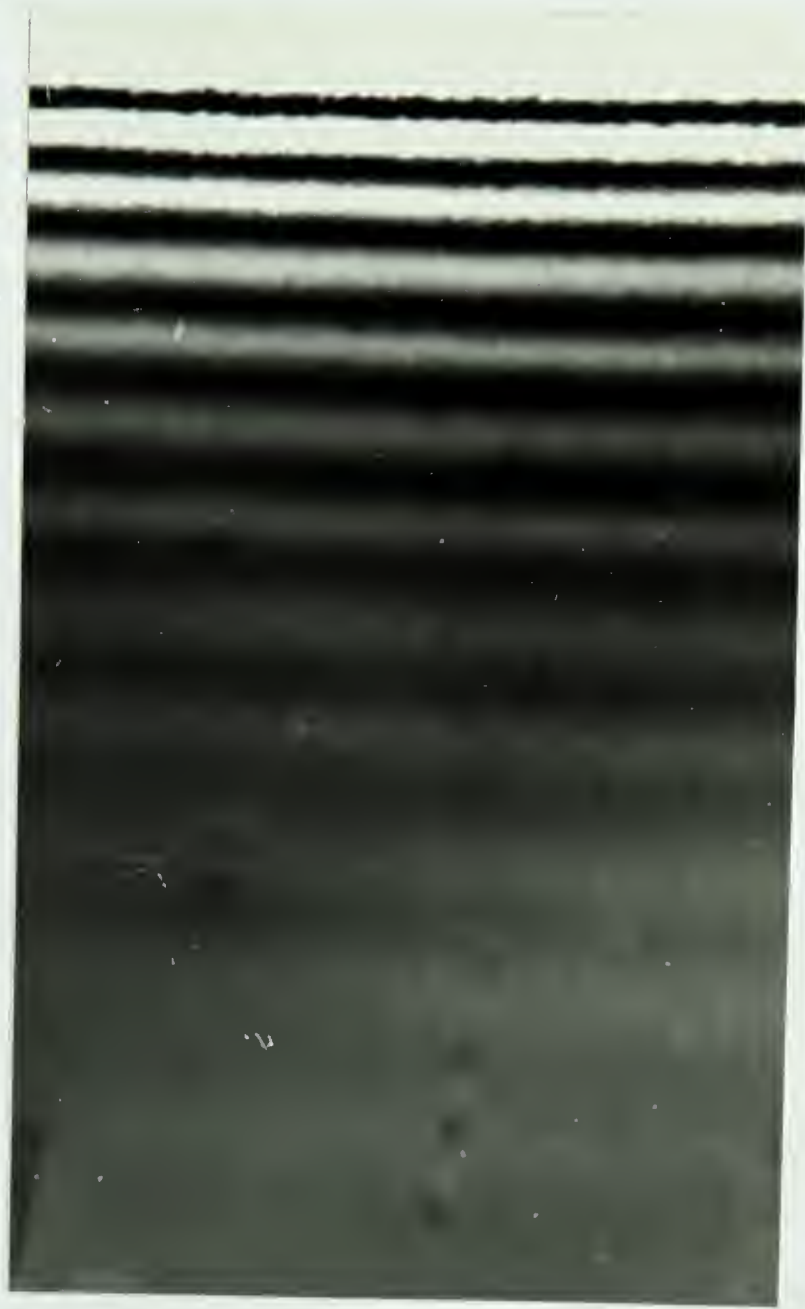


Figure 4.3 Bright field image of a wedge-shaped crystal of HCP cobalt showing the presence of extinction contours.





In order to carry out the experimental measurements of extinction distance in wedge-shaped HCP crystals, it was first necessary to orient the specimen so that the set of planes corresponding to the systematic row of interest was parallel to one of the axis of tilt in the stage. Next the specimen was tilted about the axes perpendicular to this one until the non-systematic reflections were as far as possible from satisfying their Bragg conditions. After the specimen was oriented in this manner it was tilted until one of the higher order reflections in the systematic set was in the Bragg condition, as determined from the Kikuchi pattern (see Fig. 4.4). Subsequent orientations were obtained by tilting the specimen from this reference orientation about an axes parallel to the lattice planes using the click control of the stage. Bright and dark field micrographs were taken at each previously chosen step ( $\cong 0.2\theta_B$ ). In the dark field case, the range of orientations over which these micrographs were taken was approximately three times the Bragg angle of the reflection of interest. However, in the bright field case, this range was approximately two Bragg angles. A diffraction pattern was also recorded for each thickness fringes micrograph. Therefore, the presence of undesirable non-systematic reflections was always detected.

#### 4.2.3 MEASUREMENTS OF NORMALIZED EXTINCTION DISTANCES

In order to find the variation of extinction distance  $\xi$  with  $\Delta\theta_g$  it was necessary to measure the spacing between







Figure 4.4 Diffraction pattern showing a systematic set of reflections. The reflection  $4g$  satisfies its Bragg condition therefore the Kikuchi line pass through the middle of the spot.



extinction contours in the bright and dark field micrographs. These measurements were carried out using a microdensitometer. It is important to note that absolute values of the extinction distance can not be measured. To obtain a value for this parameter a knowledge of either the wedge angle or the thickness of the specimen at a given point is required. Since these parameters can not be easily obtained for chemically polished specimens, no measurements were made of the absolute value of the extinction distance. However, a normalized value of this parameter defined as the ratio between the extinction distance at certain deviation from the Bragg condition of the first order reflection to the extinction distance when the first order reflection satisfies its Bragg condition can be determined experimentally. This can be done by taking experimental densitometer traces from micrographs obtained at the exact Bragg condition of the first order reflection in the systematic set and at the values of  $\Delta\theta_g$  covered (see Fig. 4.5). Extinction distances were measured by taking the average spacing between the fringes in the densitometer traces, provided that the peak to peak spacings do not vary by more than 10%.

#### 4.3 RESULTS

Extinction distance measurements have been carried out for three different sets of systematic reflections. The experimental results to be presented correspond to averages



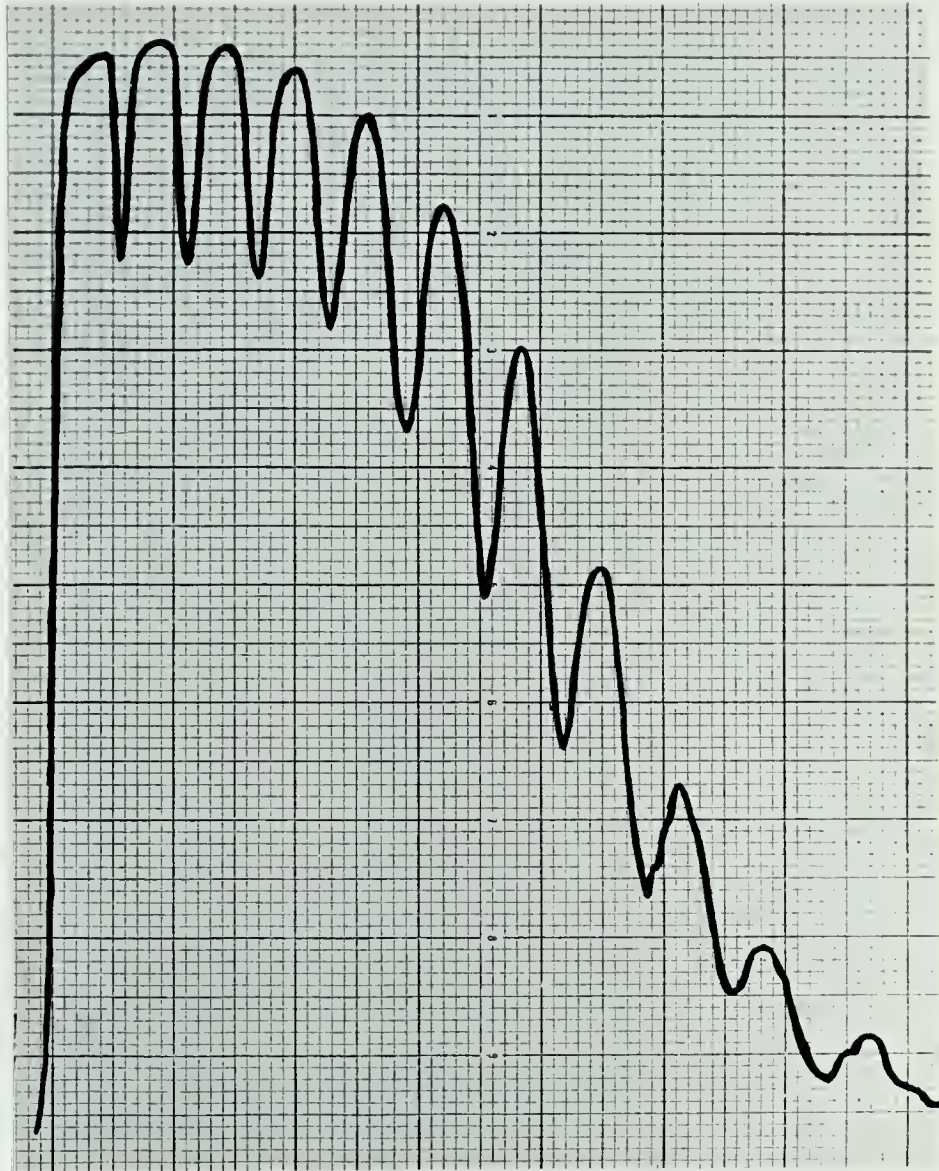


Figure 4.5 Microdensitometer trace showing the spacing of the extinction contours.





of three sets of measurements taken from three different specimens. The predictions of the two-beam and many-beam approximations of the dynamical theory are compared with these measurements.

#### 4.3.1 RESULTS OF $\xi/\xi_g$ VERSUS $\Delta\theta_g$

##### MEASUREMENTS

The experimental results of the dark field measurements for the (1 0 0), (1 -1 1) and (0 0 2) systematic sets are presented in Figs. 4.6, 4.7 and 4.8, along with the predictions of the two-beam and many-beam approximations. The predictions of the two-beam and many-beam theories were obtained using the expressions developed in chapter 2. In making the many-beam calculations only systematic reflections were included. The number of these beams used in a calculation was determined by a trial process, with more beams being added until the change in extinction distance was less than 1%. The extinction distance in the theoretical calculations were found from intensity profiles such as the one shown in Fig. 4.9. These profiles are plots of the variation in intensity of the beam under consideration with depth in the crystal. The extinction distance was found by measuring the average distance between the peaks. As can be seen from Figs. 4.6, 4.7 and 4.8, the predictions of the two-beam and many-beam approximations are very similar in the range of orientations close to the Bragg condition of the first order reflection in the systematic set ( $\Delta\theta_g=0.0$ ).





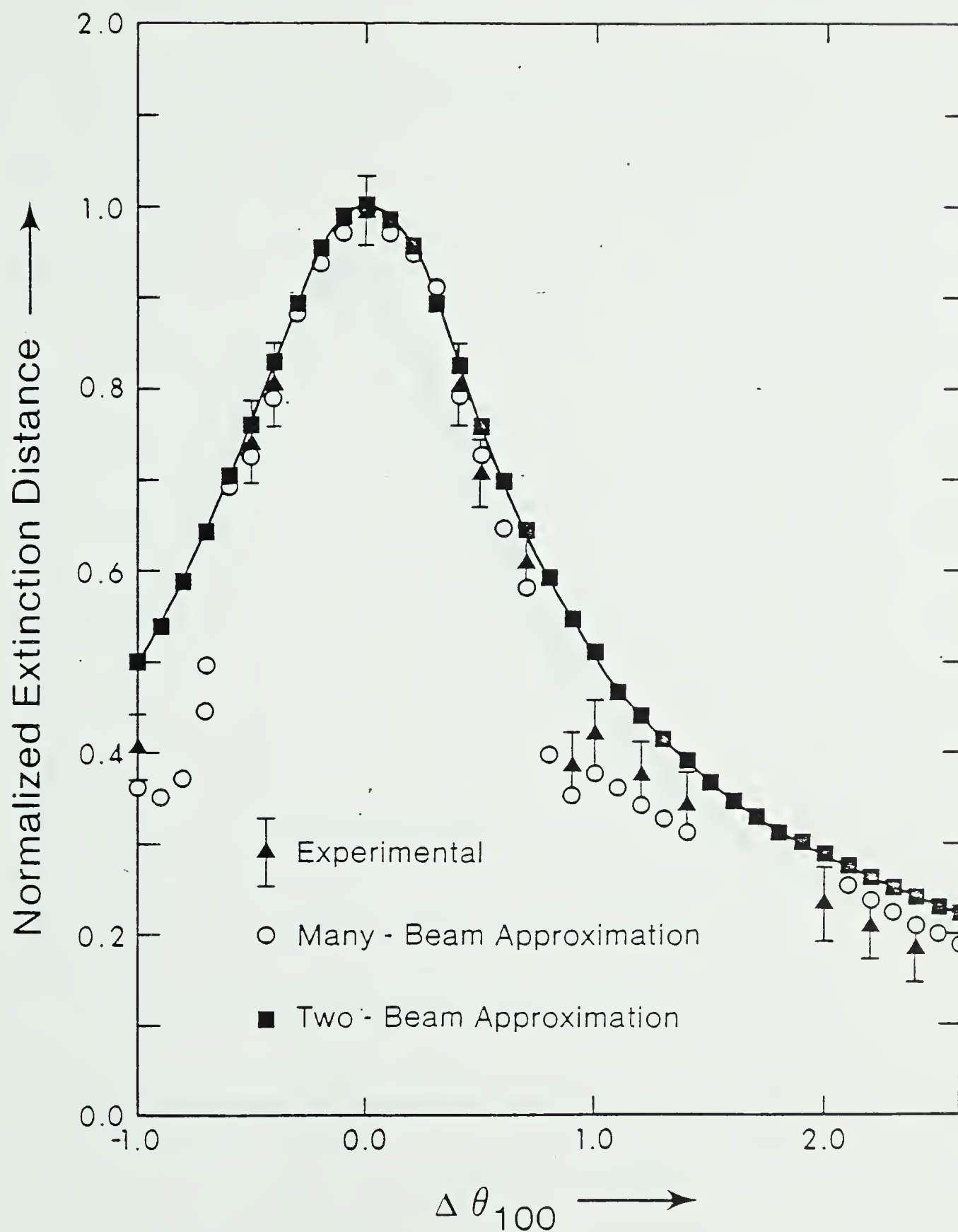


Figure 4.6 The variation of the dark field extinction distance at 150KV normalized to the value at the Bragg condition, with deviation from the Bragg condition of the (1 0 0) reflection.



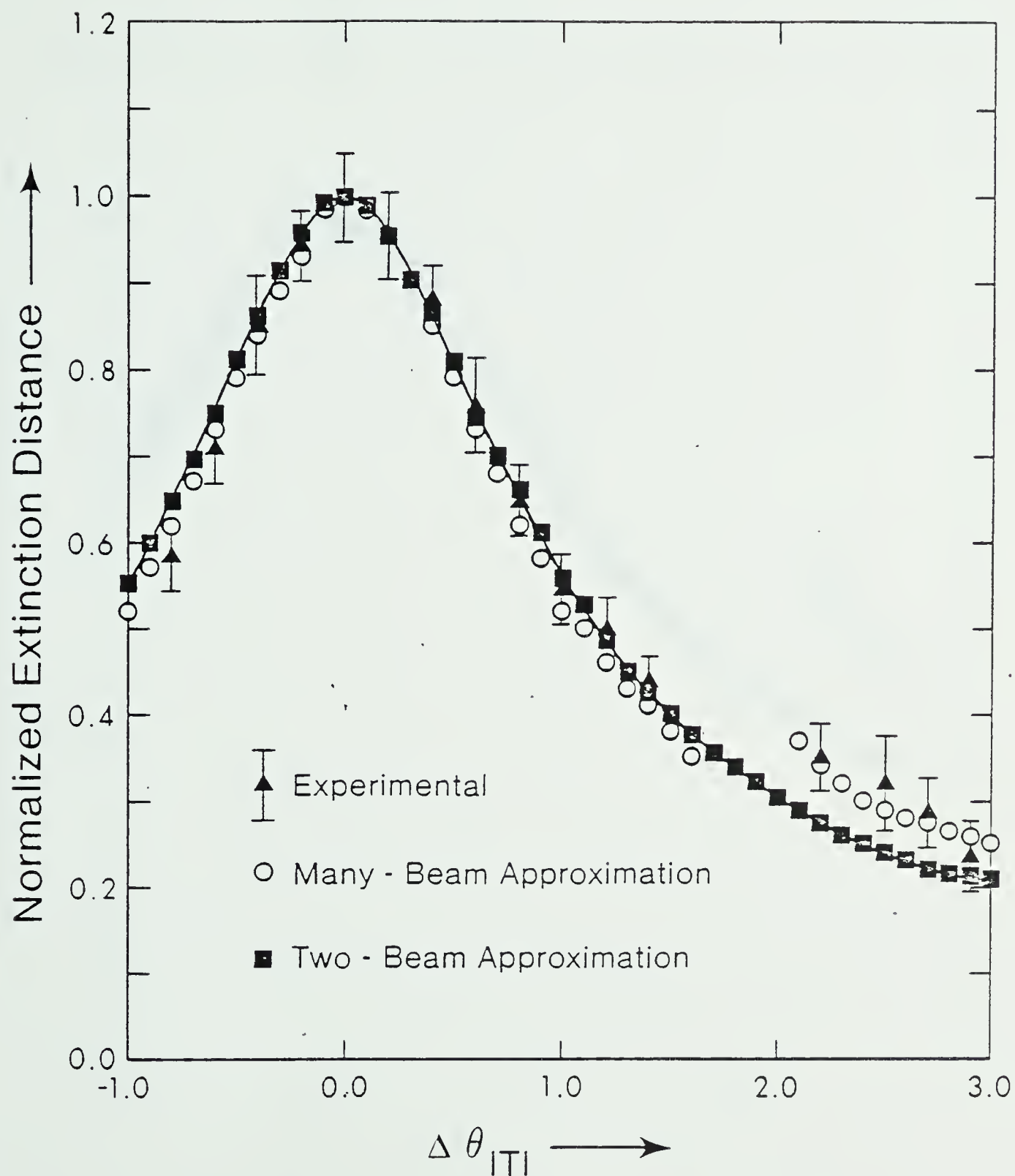


Figure 4.7 The variation of the dark field extinction distance at 150KV normalized to the value at the Bragg condition, with deviation from the Bragg condition of the (1 -1 1) reflection.



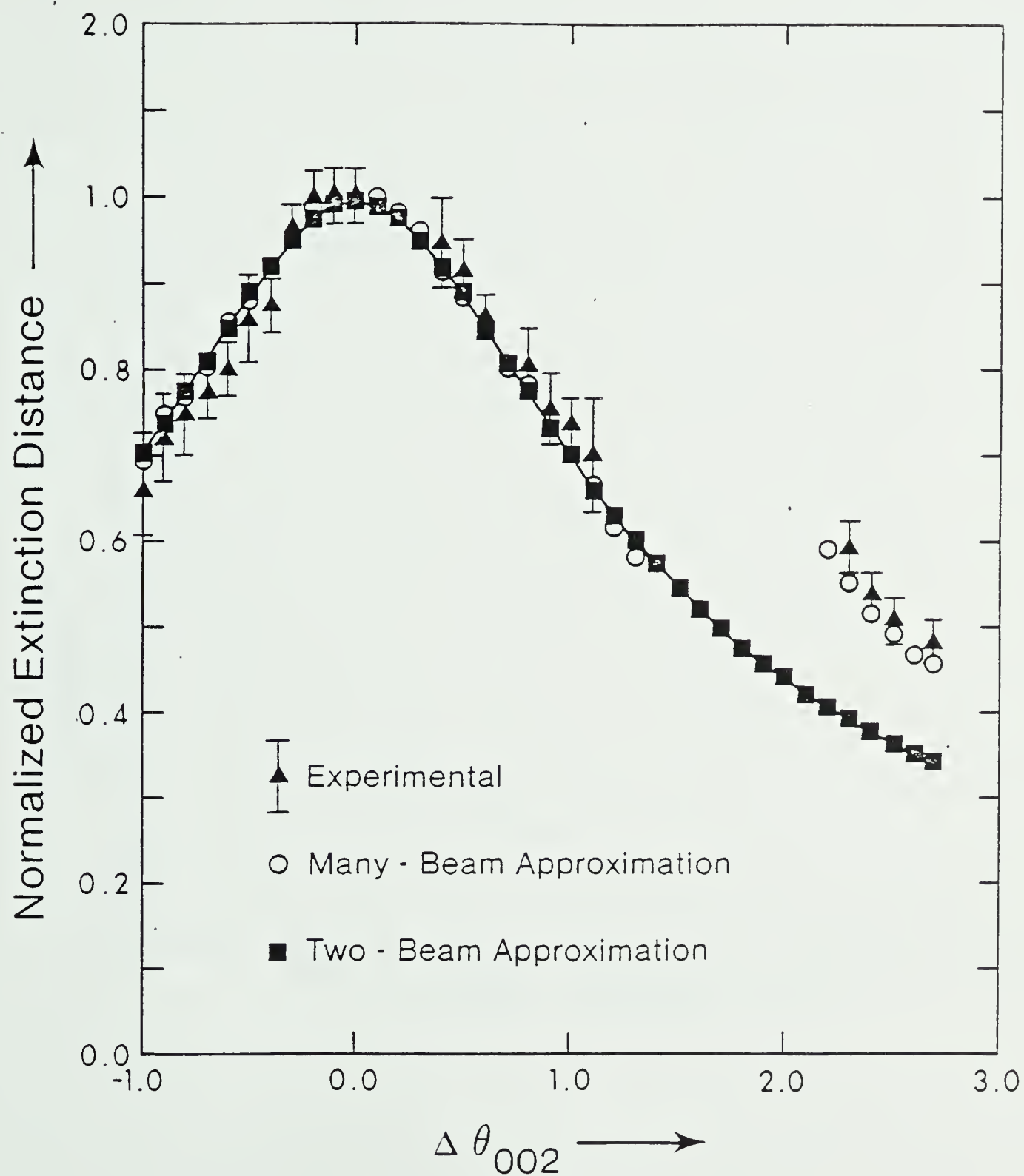


Figure 4.8 The variation of the dark field extinction distance at 150KV normalized to the value at the Bragg condition, with deviation from the Bragg condition of the (0 0 2) reflection.



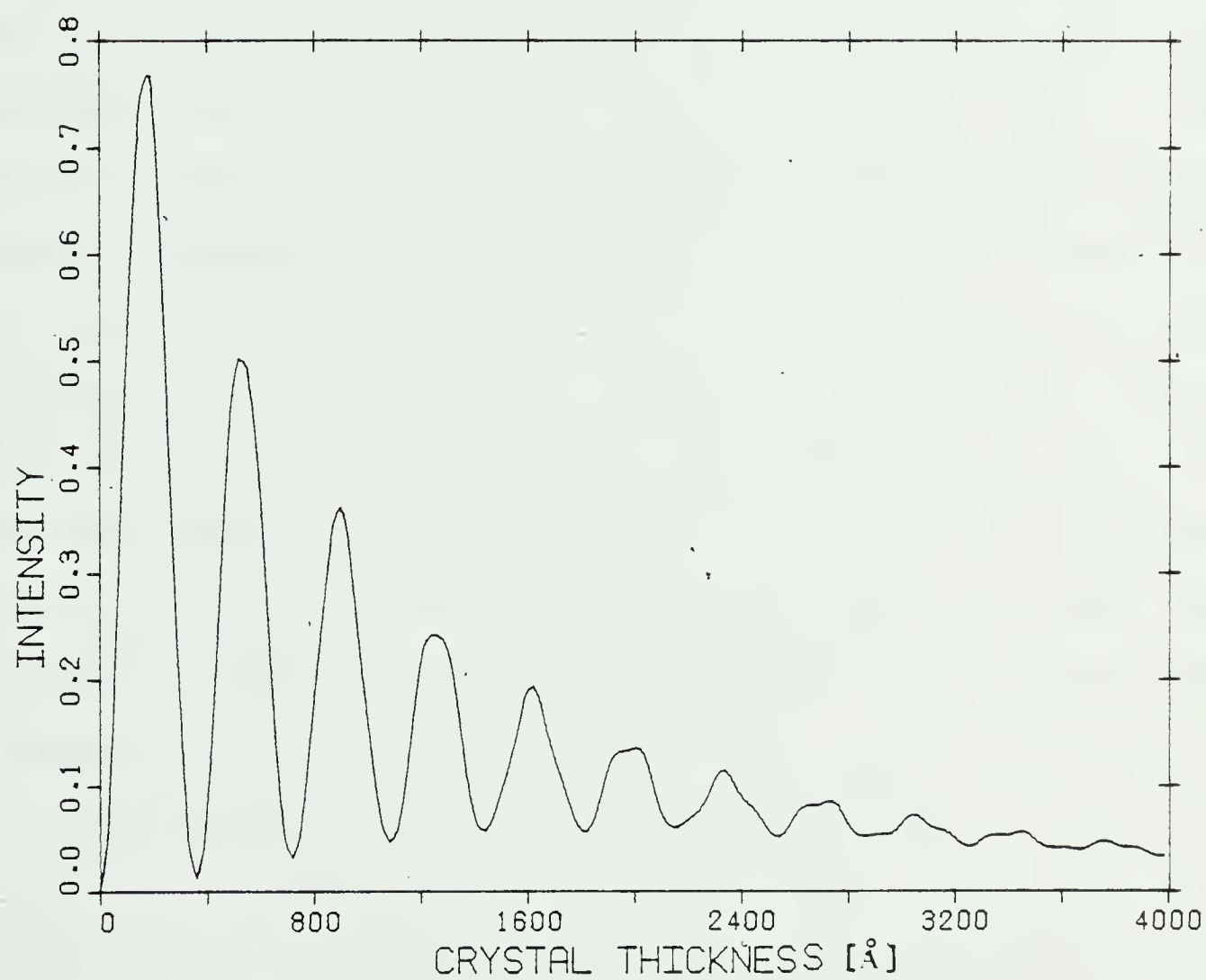


Figure 4.9 An intensity profile of the variation with depth of the (1 -1 1) diffracted beam intensity at 150KV and found from a 13-beam approximation.





At orientations in the range of the Bragg condition of the second order reflection, the predictions of the two-beam and many-beam approximations are in good agreement with experiment for the  $(1\ -1\ 1)$  and  $(0\ 0\ 2)$  systematic sets. However, in the  $(1\ 0\ 0)$  case, a sharp drop in the experimental extinction distance is obtained at  $\Delta\theta_g \cong 1.0$ . This drop can not be accounted by the two-beam approximation but excellent agreement between theory and experiment was obtained when systematic reflections were taken into account. When the third order reflection satisfies its Bragg condition ( $\Delta\theta_g = 2.0$ ), both the  $(1\ -1\ 1)$  and  $(0\ 0\ 2)$  systematic sets show a sharp increase in extinction distance with the increase being considerable greater in the  $(0\ 0\ 2)$  case. Good agreement between theory and experiment was only obtained when systematic reflection were taken into account. In the  $(1\ 0\ 0)$  case, however, both the two-beam and many-beam approximations agree with the experimental results.

The results of the bright field measurements for the  $(1\ 0\ 0)$ ,  $(1\ -1\ 1)$  and  $(0\ 0\ 2)$  systematic sets are presented in Figs. 4.10, 4.11 and 4.12 along with the predictions of the two-beam and many-beam approximations. For the  $(0\ 0\ 2)$  and  $(1\ -1\ 1)$  systematic sets the predictions of the two-beam and many-beam approximations are similar in most of the range of orientations considered and the experimental extinction distances are also in good agreement with these predictions. On the other hand, for the  $(1\ 0\ 0)$  set, the two-beam and



many-beam theoretical results are similar only at orientations in the range of the Bragg condition of the first order reflection ( $\Delta\theta_g=0.0$ ). Thus for example at values of  $\Delta\theta_g \cong 1.0$  an unusual increase in the experimental extinction distance is obtained. This increase can not be accounted by the two-beam approximation but excellent agreement between theory and experiment was obtained when systematic reflections were taken into account.

#### 4.3.2 ANALYSIS OF THE RESULTS IN TERMS OF BLOCH WAVE PARAMETERS

In this section an analysis of the results presented in section 4.3.1 in terms of Bloch wave parameters will be presented. Since the basic mechanisms which emerge from this kind of analysis are similar in kind for each of the three systematic sets of reflections, a detailed analysis for the (1 0 0) set only will be presented. In order to carry out such an analysis, the importance of each of the Bloch waves contributing to the diffracted beam intensity have to be assessed. The manner in which this can be done can be seen by considering equation 2.20 which shows that the importance of the contribution of a particular Bloch wave to diffracted beam intensity is determined by  $|C^{(i)}_0 C^{(i)}_g|$ .

##### 4.3.2.1 ANALYSIS OF THE DARK AND BRIGHT FIELD RESULTS FOR THE (1 0 0) SYSTEMATIC SET.

The variation of  $|C^{(i)}_0 C^{(i)}_g|$  for the (1 0 0) systematic set as a function of  $\Delta\theta_{(100)}$  has therefore



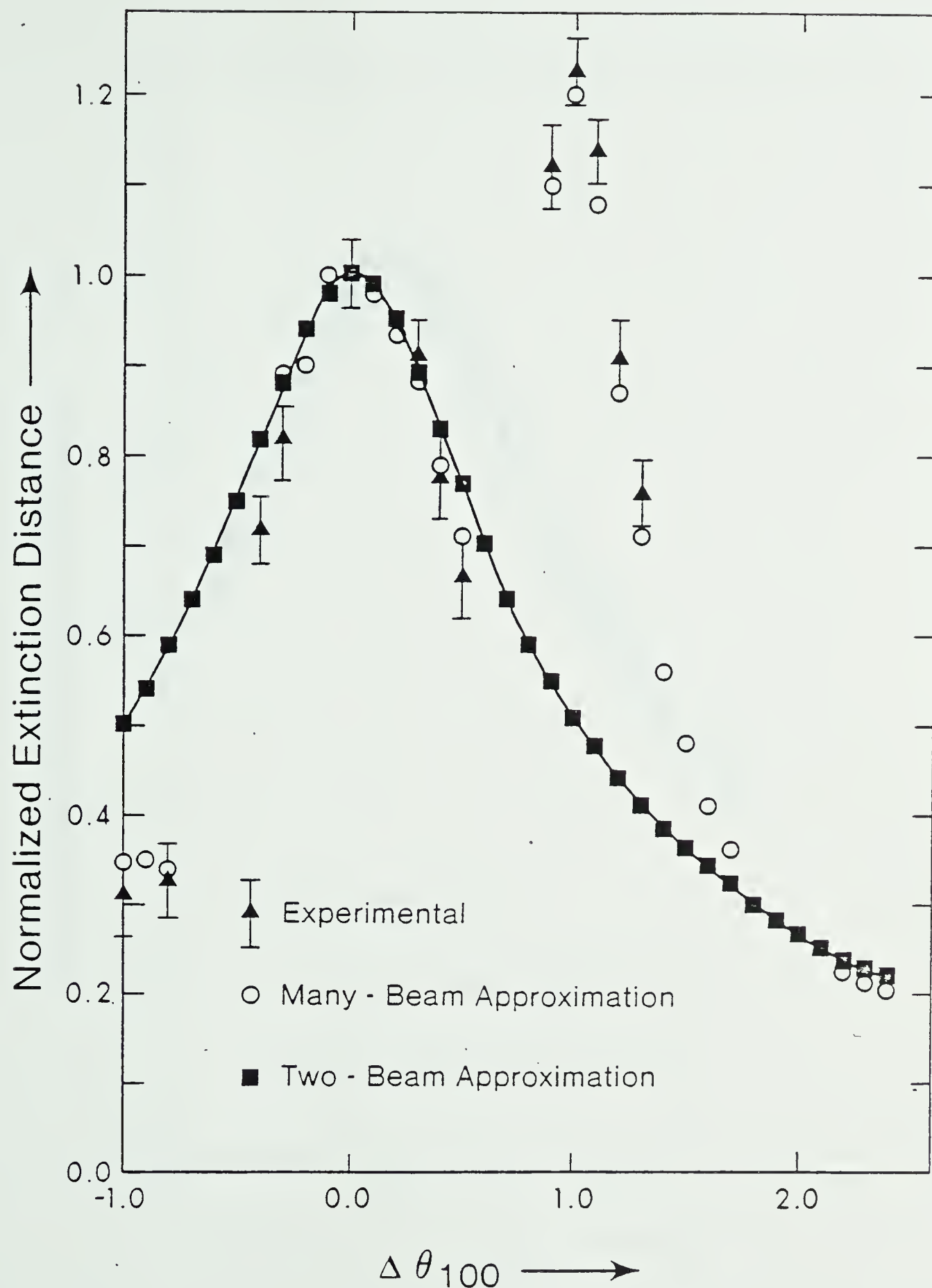


Figure 4.10 The variation of the bright field extinction distance at 150KV normalized to the value at the Bragg condition, with deviation from the Bragg condition of the (1 0 0) reflection.



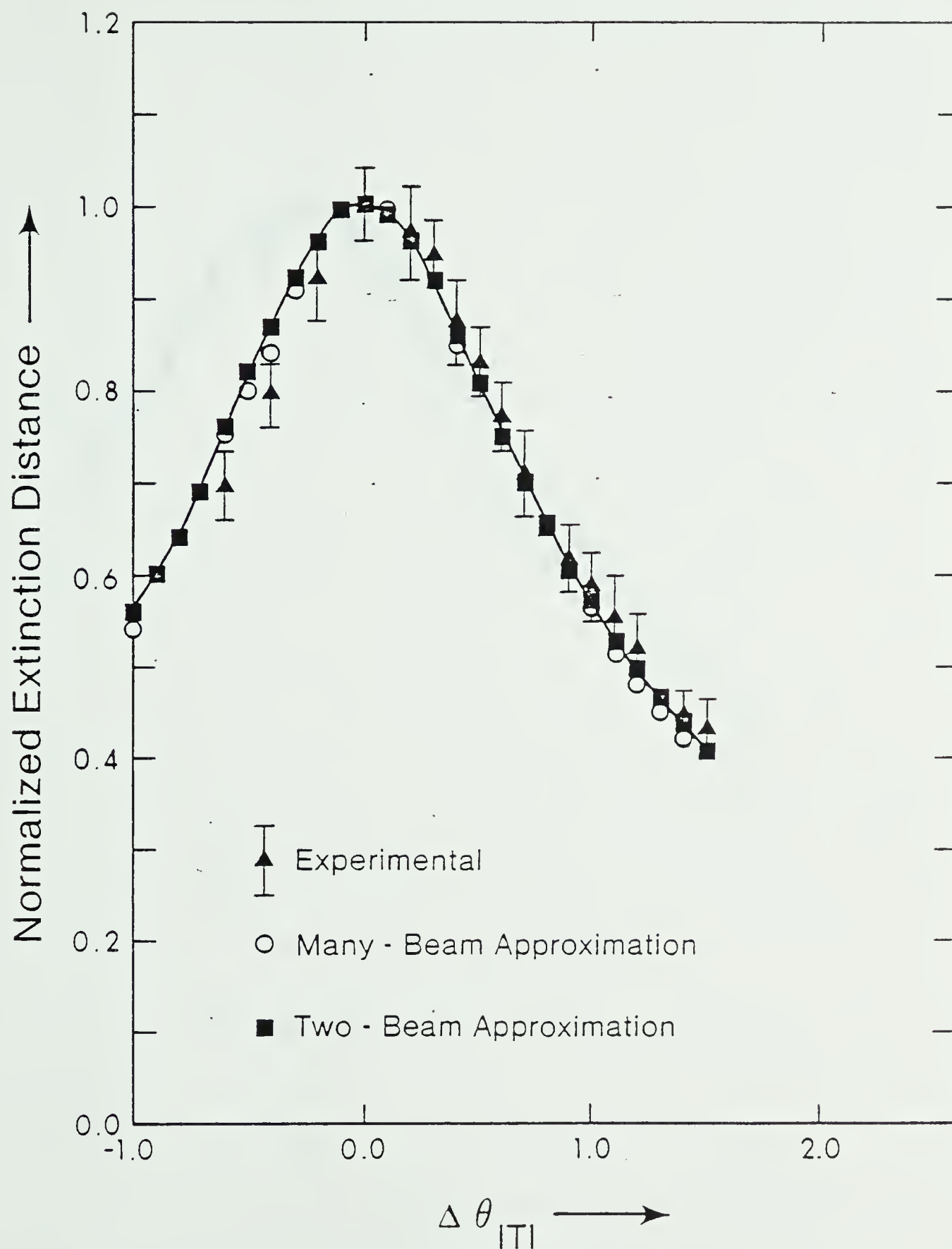


Figure 4.11 The variation of the bright field extinction distance at 150KV normalized to the value at the Bragg condition, with deviation from the Bragg condition of the (1 -1 1) reflection.





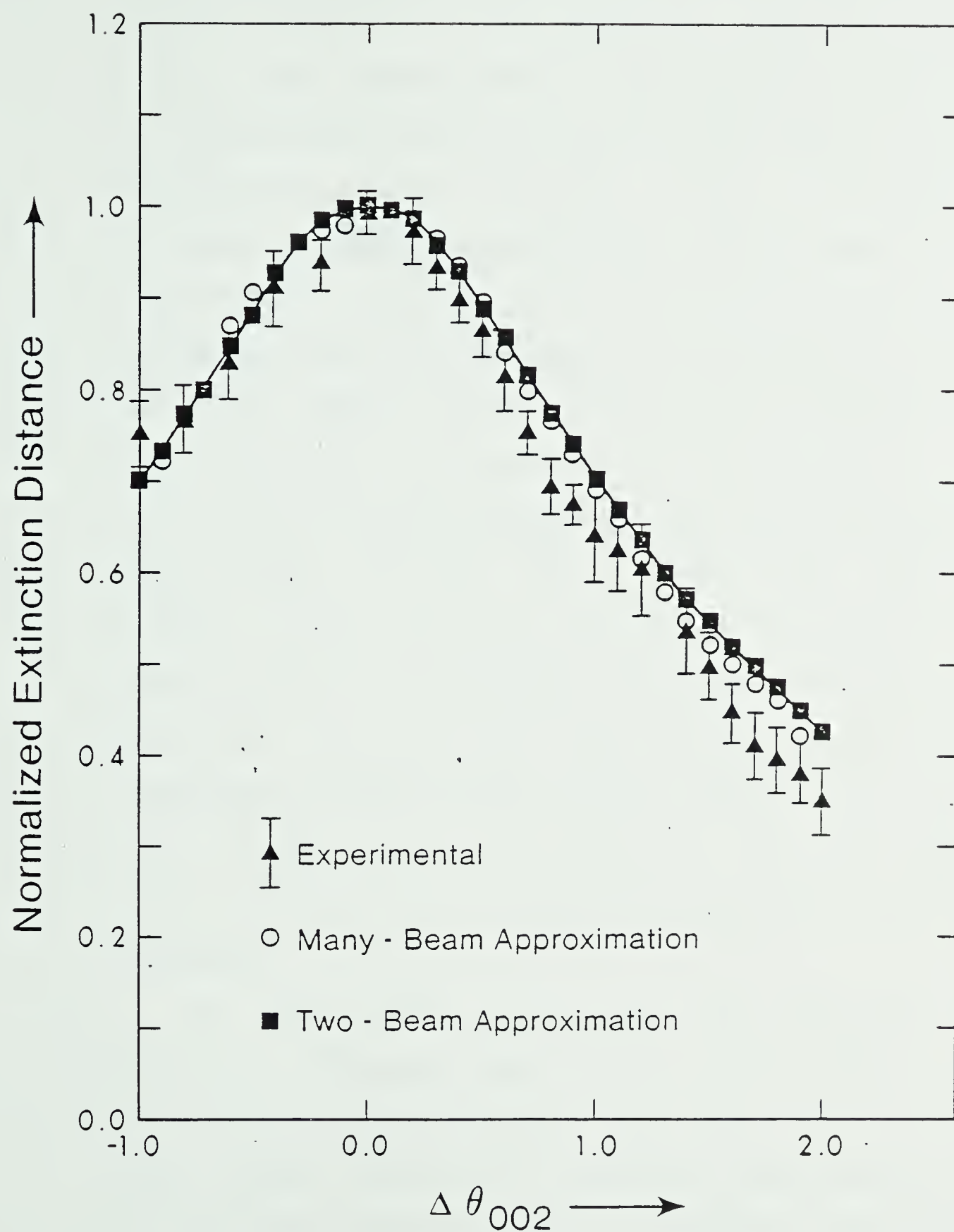


Figure 4.12 The variation of the bright field extinction distance at 150KV normalized to the value at the Bragg condition, with deviation from the Bragg condition of the (0 0 2) reflection.



been obtained and is shown in Fig. 4.13. It was pointed out in section 4.3.1 that excellent agreement between the two-beam approximation and experiment was obtained at orientations near  $\Delta\theta_{(100)} \cong 0.0$ . The reason for this can be clearly seen from Figs. 4.13a, b which show that at these orientations Bloch waves 1 and 2 make the most significant contributions to diffracted beam intensity. The sharp drop in the value of the extinction distance which is shown in Fig. 4.6 can now be understood from Fig. 4.13a which indicates that at orientations close to  $\Delta\theta_{(100)} = 1.0$ , an interchange in importance between Bloch waves 2 and 3 occurs. As a result, the extinction distance prior to the occurrence of the interchange is given by  $1/(\gamma^{(1)} - \gamma^{(2)})$  while after the interchange it is given by  $1/(\gamma^{(1)} - \gamma^{(3)})$ . Fig. 4.14 shows the four most important branches of the many-beam dispersion surface. This figure clearly indicates that for  $\Delta\theta_g \cong 1.0$ ,  $(\gamma^{(1)} - \gamma^{(3)}) > (\gamma^{(1)} - \gamma^{(2)})$  therefore explaining the results obtained.

In the bright field case the unusually high extinction distance shown in Fig. 4.10 at  $\Delta\theta_{(100)}$  close to 1.0 can be understood by referring to Fig. 4.13b. This figure shows that at  $\Delta\theta_g = 0.0$ , Bloch waves 1 and 2 are the most important whereas at  $\Delta\theta_g \cong 1.0$ , Bloch waves 2 and 3 become the most important. Again, referring to Fig. 4.14, it can be seen therefore that  $(\gamma^{(1)} - \gamma^{(2)}) > (\gamma^{(2)} - \gamma^{(3)})$ , as a result, the high



extinction distance obtained after the interchange of the Bloch waves is explained.

#### 4.4 EFFECTS OF HCP SYSTEMATIC REFLECTIONS ON ANOMALOUS ABSORPTION

Thickness fringes obtained from electron microscope images of wedge crystals are often characterized by a decrease in fringe contrast as the thickness of the crystal is increased although the transmitted or diffracted beam intensity usually remains relatively high (see Fig. 4.15). The decrease in fringe contrast can be understood in terms of the differences in the transmission properties (absorption coefficients) of the Bloch waves giving rise to the contours. For example, at the Bragg condition of the first order reflection ( $\Delta\theta_g=0.0$ ) Bloch waves 1 and 2 are the most important. Under these conditions Bloch wave 1 has a maximum in intensity peaked at the atomic planes, whereas Bloch wave 2 has a minimum in intensity at these positions (see Amelinckx et. al. 1978). Bloch wave 1 is, therefore, highly absorbed by the crystal (i. e. has a high absorption coefficient) whereas Bloch wave 2 is well transmitted (i. e. has a low absorption coefficient). Thus, if the contribution of Bloch wave 1 to the intensity becomes small enough to render thickness fringes inobservable, appreciable intensity associated with Bloch wave 2 will still be transmitted. The effects on the image contrast due to the different attenuations of these two Bloch waves is referred to as



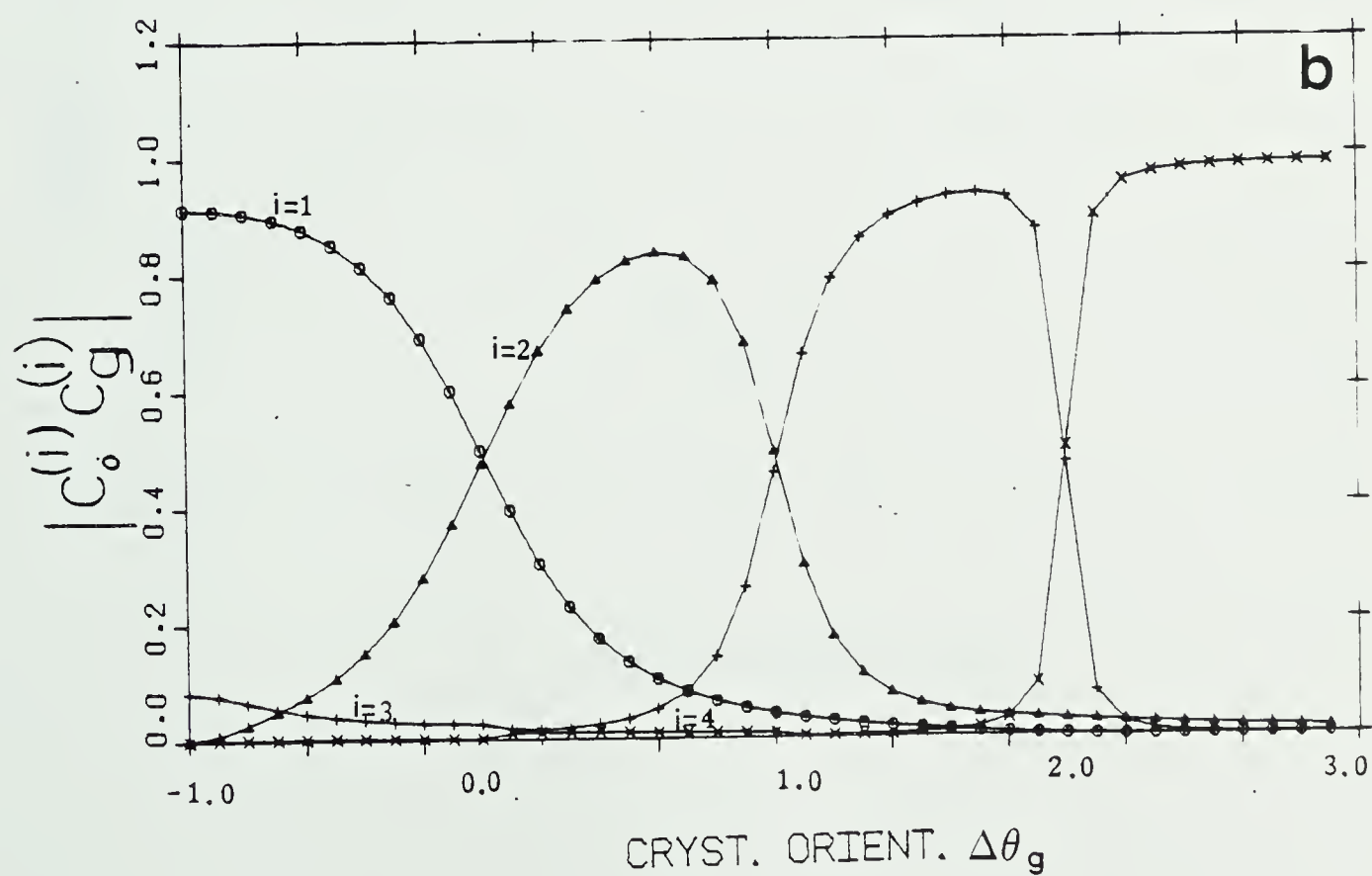
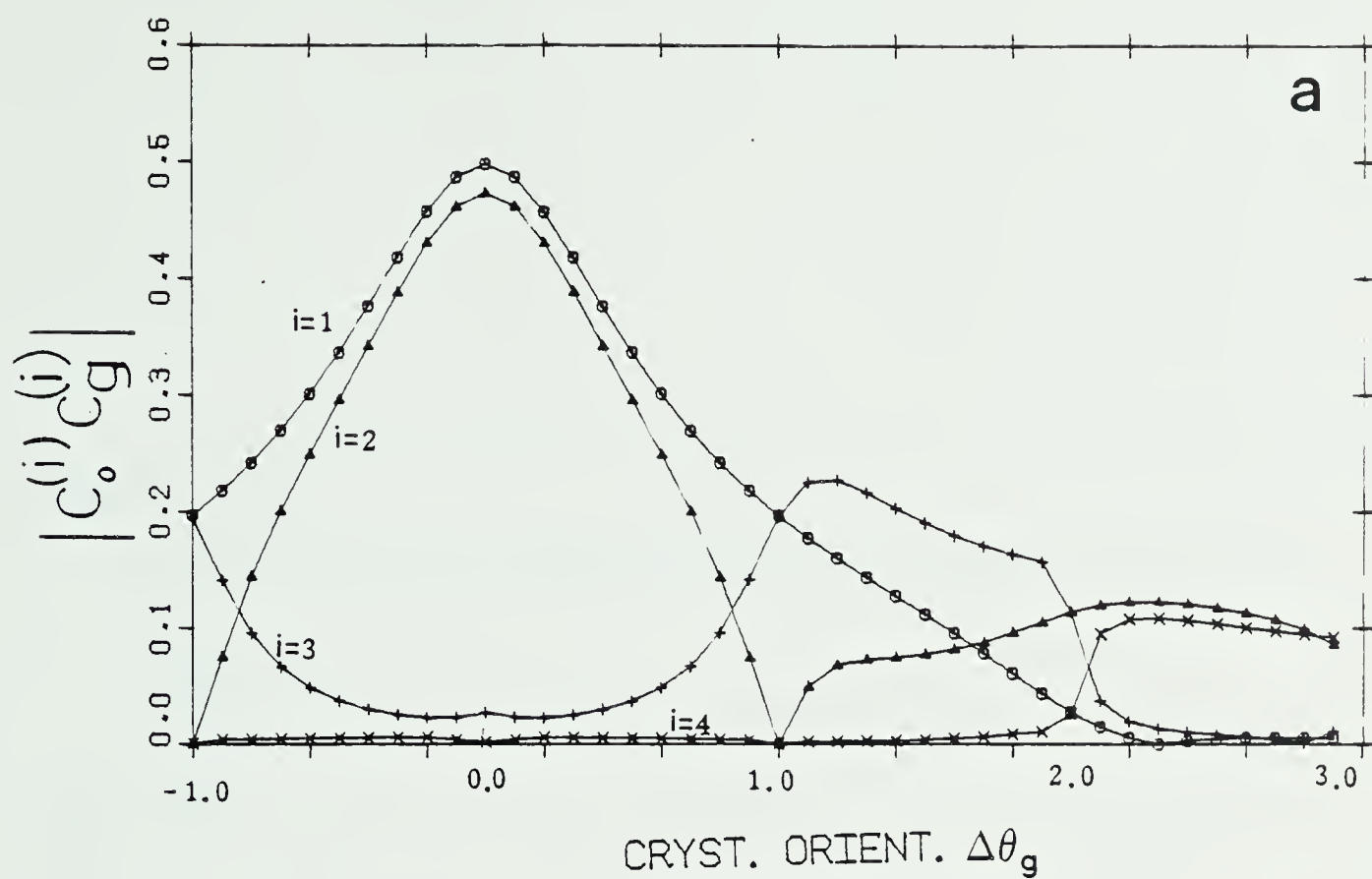


Figure 4.13 The variation of  $|C_o^{(i)} C_g^{(i)}|$  with deviation from the Bragg condition of the (1 0 0) reflection for Bloch waves 1 to 4. a) dark field, b) bright field.





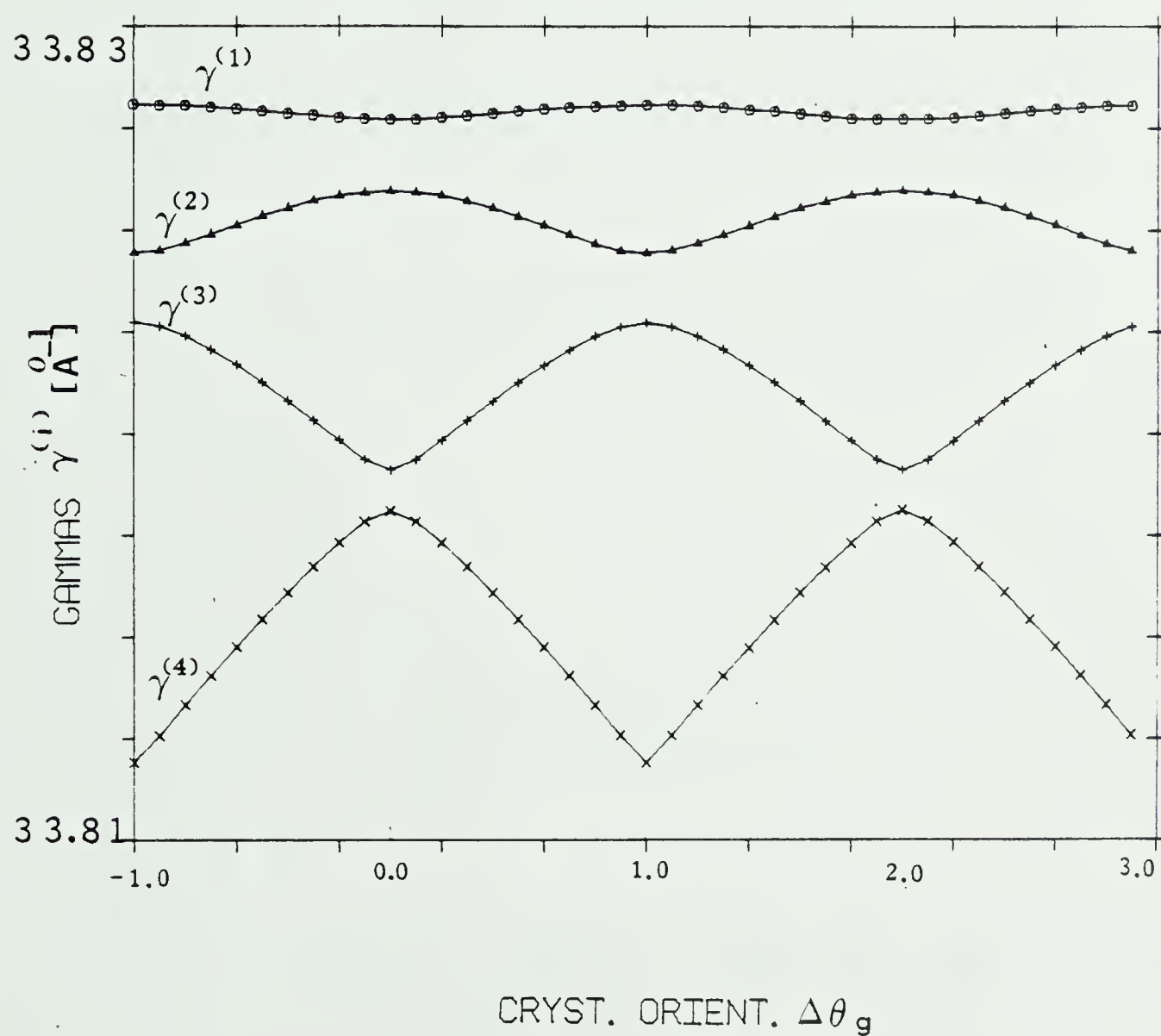


Figure 4.14 Branches of the dispersion surface for Bloch waves 1 to 4 in the (1 0 0) systematic set.



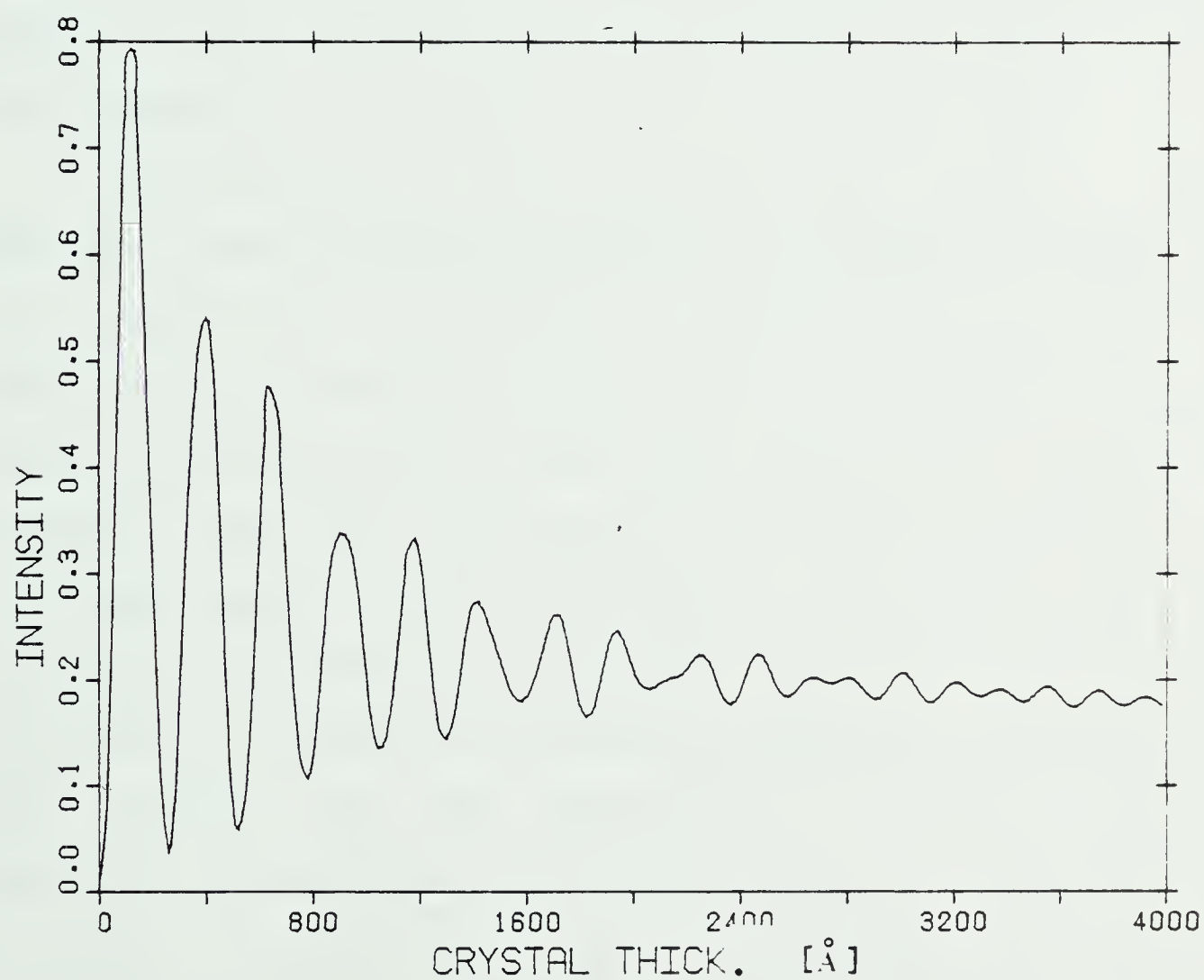


Figure 4.15 An intensity profile showing the decrease in fringe contrast as the thickness of the crystal is increased.



anomalous absorption. The effects of anomalous absorption on electron microscope images containing lattice defects have been studied by various authors. Hashimoto et. al. (1962), for example, have shown that in the case of a stacking fault, the visibility of the fringes near the center of the fault decreases in thick crystals. Howie and Whelan (1963), indicated that the oscillatory contrast characteristic of dislocations inclined to the foil surface disappears in thick crystals except when the dislocation is close to the foil surface.

Previous work in cubic materials (see Sheinin, 1970), has shown that in the case where only systematic reflections are assumed to be present, the effects of anomalous absorption are strongly dependent on the deviation from the Bragg condition of the lowest order reflection. Thus, for example, when the reflection  $g$ , of a systematic set is in the exact Bragg condition, pronounced effects of anomalous absorption can normally be observed. However, if the crystal is tilted to values of the deviation parameter greater than that required for the reflection  $3g$  to be at its Bragg condition, the effects of anomalous absorption are found to be small. Clearly, in order to understand the effects of absorption on the visibility of thickness fringes and on the image contrast of lattice defects, the absorption coefficients  $q^{(i)}$ , of the various Bloch waves must be known.

The effects of anomalous absorption in HCP materials have not received much attention in the literature. Bonnet



(1976) carried out theoretical investigations on the effects of systematic reflections on image contrast in different materials. As part of this work, he studied the dependence of the absorption coefficients for different crystalline structures as a function of the deviation parameter. One of the materials used in his theoretical calculations was HCP cobalt. However, he only obtained values for  $q^{(2)}$ ,  $q^{(3)}$  and  $q^{(4)}$  and therefore no analysis was made of the relationship between these values and the anomalous absorption characteristics.

#### 4.4.1 BLOCH WAVE ABSORPTION COEFFICIENTS FOR THE (1 0 0), (0 0 2) AND (1 -1 1) SYSTEMATIC REFLECTIONS

The variation of  $q^{(i)}$  with  $\Delta\theta_g$  is periodic with a period equal to twice the Bragg angle of the lowest order systematic reflection (see for example, Sheinin, 1970). The magnitudes of  $q^{(i)}$  for Bloch waves 1, 2, 3 and 4 for the three different systematic sets in HCP cobalt have been calculated and are plotted in Figs. 4.16, 4.17 and 4.18 for values of  $\Delta\theta_g$  in the range of  $-1.0$  to  $1.0$  (symmetry orientation to  $2g$  in its Bragg condition). It is clear in comparing these figures that the dependence of the absorption coefficients  $q^{(i)}$  on  $\Delta\theta_g$  is very similar for the (0 0 2) and (1 -1 1) systematic sets. However, appreciable differences between the (1 0 0) set and these two sets can clearly be seen. Thus, for example, Figs. 4.17 and 4.18 show that when the (1 -1 1) and (0 0 2) systematic sets are





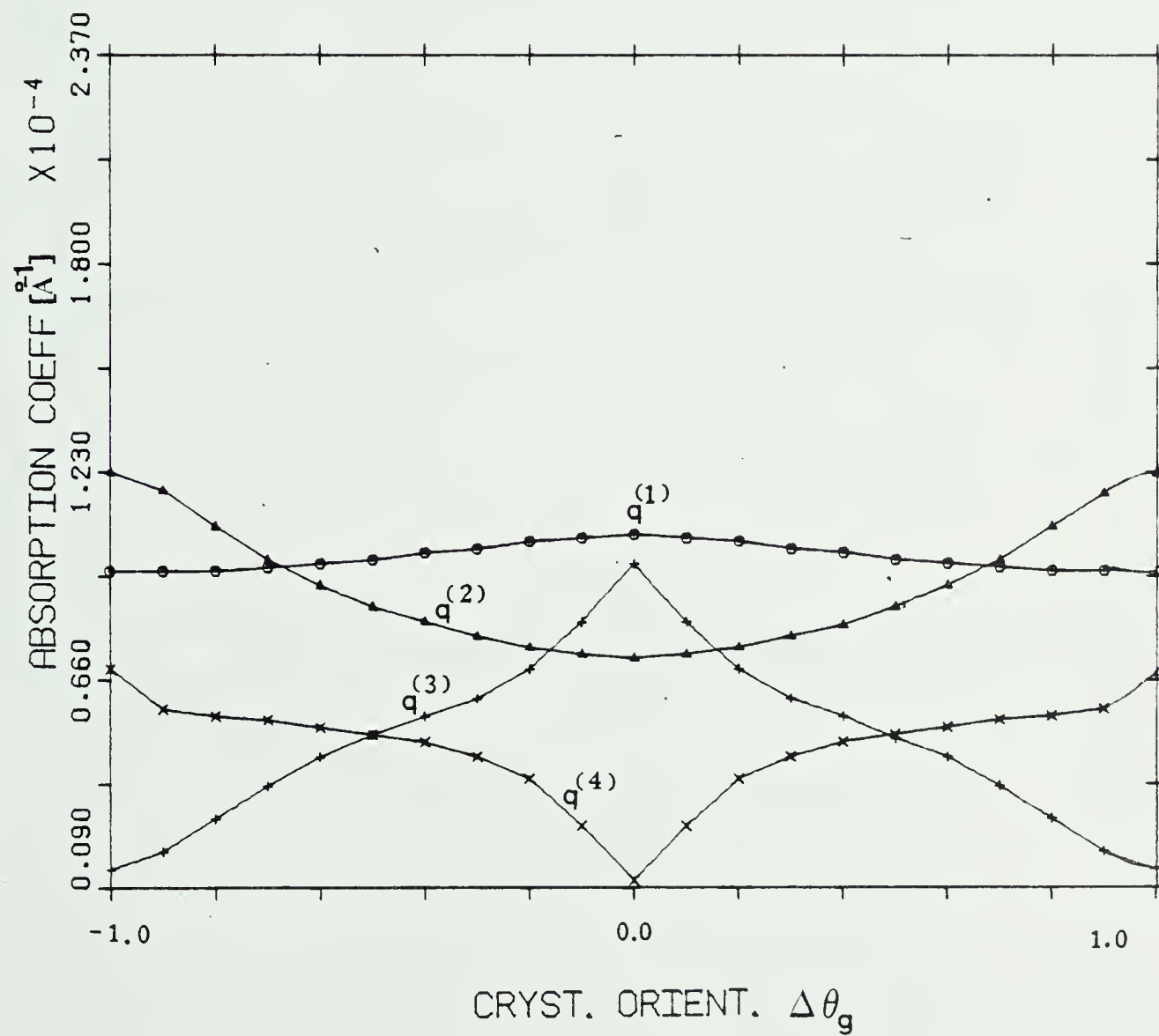


Figure 4.16 Bloch wave absorption coefficients  $q^{(i)}$  as a function of the crystal orientation for the (1 0 0) set.



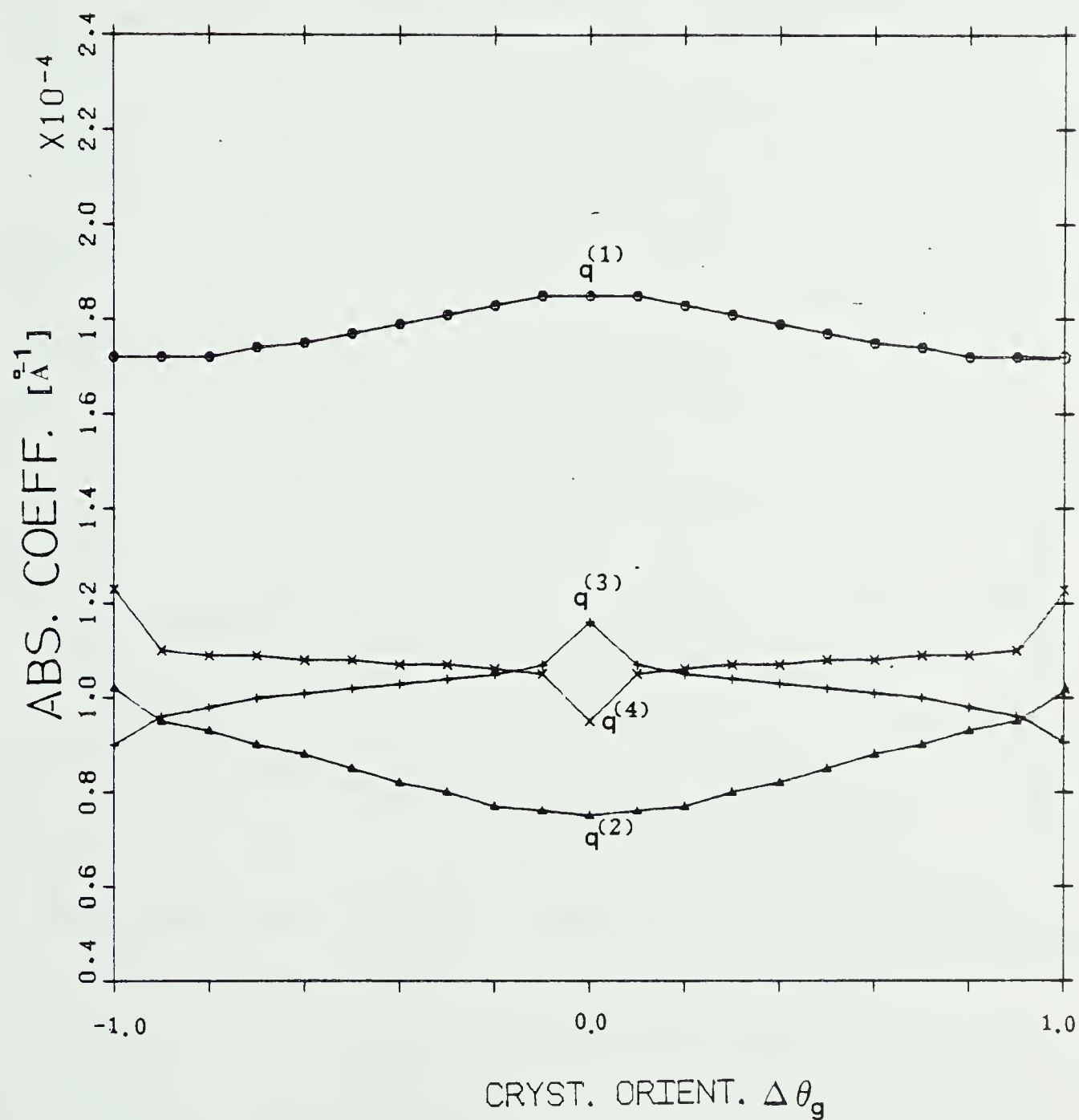


Figure 4.17 Bloch wave absorption coefficients  $q^{(i)}$  as a function of the crystal orientation for the (1 -1 1) set.



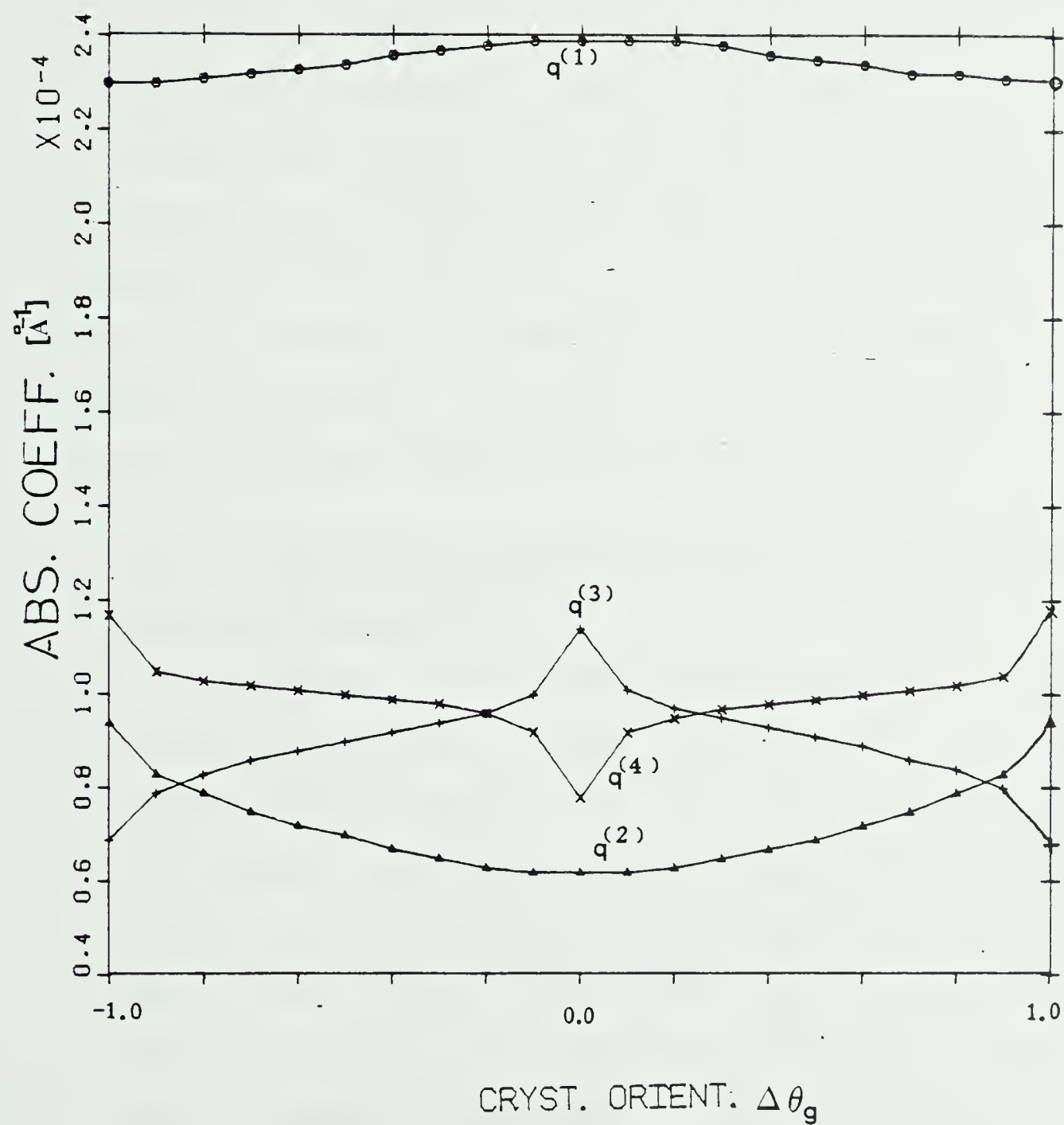


Figure 4.18 Bloch wave absorption coefficients  $q^{(i)}$  as a function of the crystal orientation for the (0 0 2) set.



excited at the orientation where the lowest order reflection satisfies its Bragg condition ( $\Delta\theta_g=0.0$ ), the absorption coefficient  $q^{(1)}$ , corresponding to Bloch wave 1 is much larger than the absorption coefficient  $q^{(2)}$  for Bloch wave 2. Therefore, strong anomalous absorption similar to that obtained in FCC materials would be expected in HCP cobalt for these systematic sets. However, for the (1 0 0) systematic set of reflections, Fig. 4.16 shows that the absorption coefficient  $q^{(1)}$  is approximately equal to  $q^{(2)}$  and thus, anomalous absorption is not expected to be important at  $\Delta\theta_g=0.0$ , provided that Bloch waves 1 and 2 are the only important Bloch waves excited.

#### 4.4.1.1 RELATIONSHIP BETWEEN ABSORPTION COEFFICIENTS AND BLOCH WAVE CHANNELING.

In order to understand differences in absorption coefficients a plot of the intensity of each of the Bloch waves excited,  $|b^{(i)}|^2$ , as a function of the interplanar position between the lattice planes is sometimes very useful (see for example, Amelinckx et. al. 1978). Figs. 4.19 and 4.20 show many-beam calculations of the intensity distribution of the two most important Bloch waves for the (0 0 2) and (1 0 0) systematic sets when the lowest order reflection in the set satisfies its Bragg condition. Notice, that the origin of coordinates chosen for the dynamical calculations is the midpoint between the two atoms in the HCP unit cell. The vertical dotted lines denote the





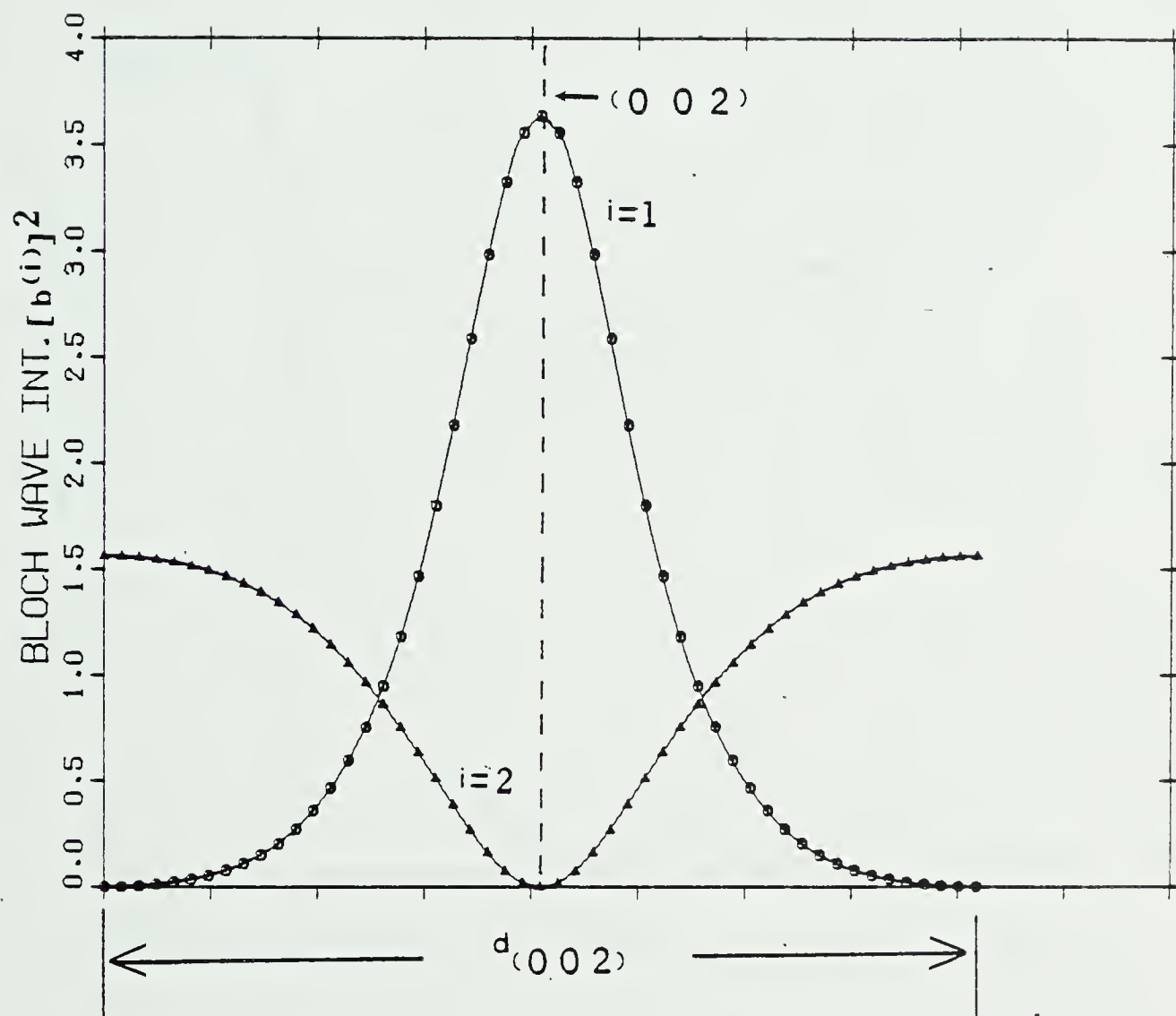


Figure 4.19 Bloch wave intensities for the two most important Bloch waves at the Bragg condition of the  $(0\ 0\ 2)$  reflection as a function of the interplanar distance  $d_{(002)}$ .



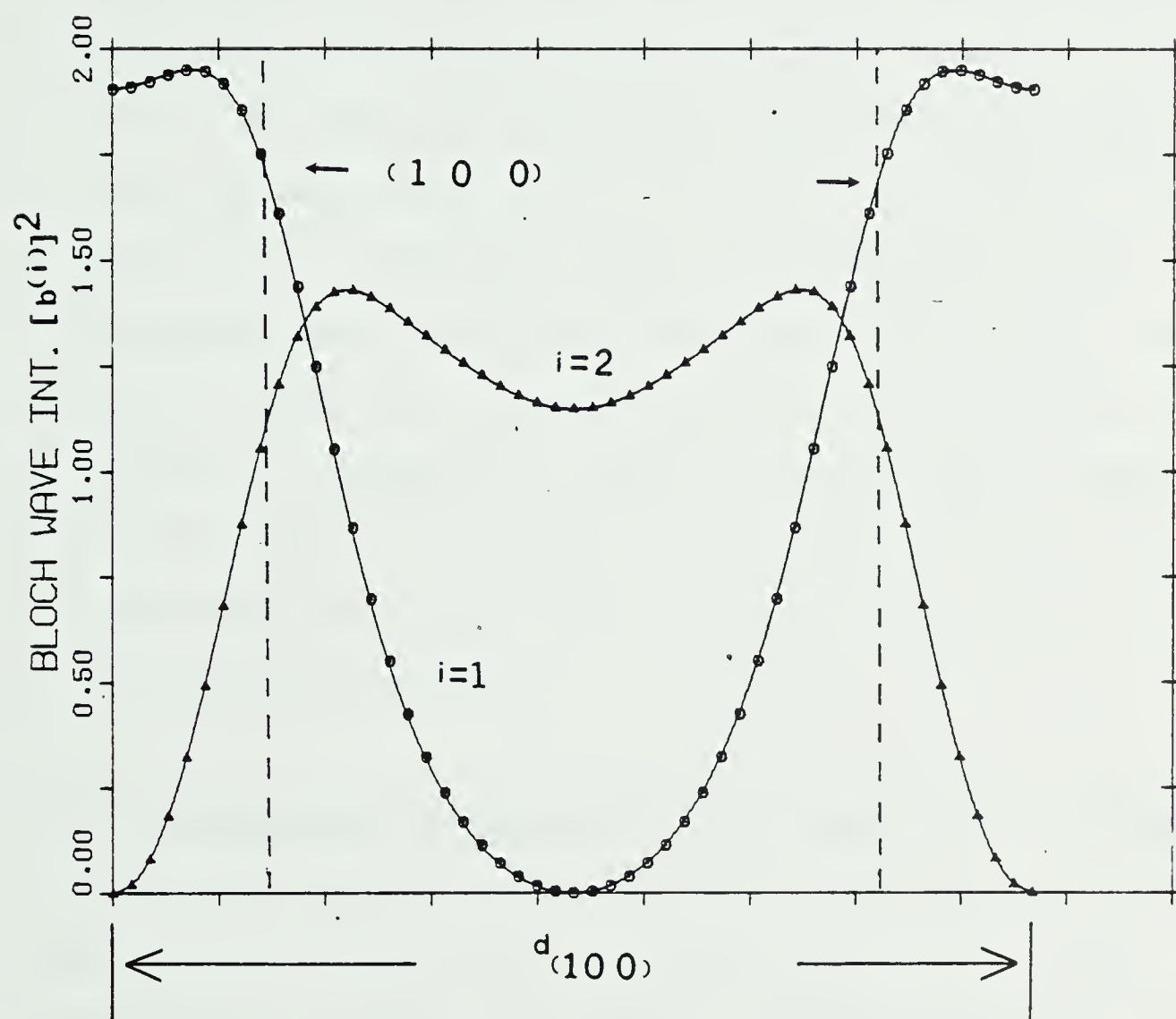


Figure 4.20 Bloch wave intensities for the two most important Bloch waves at the Bragg condition of the  $(1\ 0\ 0)$  reflection as a function of the interplanar distance  $d_{(100)}$ .



positions of the (0 0 2) atomic planes in Fig. 4.19 and the (1 0 0) atomic planes in Fig. 4.20. Fig. 4.19 shows quite clearly that when the (0 0 2) systematic set is excited Bloch wave 1 has a maximum in intensity peaked at the atomic planes whereas Bloch wave 2 has a minimum in intensity at these positions. Bloch wave 1 is therefore highly absorbed and its absorption coefficient  $q^{(1)}$  is large, whereas Bloch wave 2 is well transmitted and its absorption coefficient  $q^{(2)}$  is small compared with  $q^{(1)}$ . However, when the (1 0 0) systematic set is excited, Fig. 4.20 shows that the Bloch waves 1 and 2 both have the equal intensity close to the atomic planes. Therefore, their respective absorption coefficients  $q^{(1)}$  and  $q^{(2)}$  are approximately equal in magnitude and both Bloch waves are expected to be similarly absorbed.

#### 4.4.2 TRANSMISSION PROPERTIES FOR HCP SYSTEMATIC REFLECTIONS

In the past, investigations have been carried out to obtain the crystal orientations for the best beam transmission. Thus, for example, Humphreys et. al. (1971), have shown that for FCC materials and for 100KV electrons the best transmission orientation in the bright field is slightly positive of the first-order Bragg position. For higher electron energies ( 1000KV ) the best transmission orientations were found to depend on the atomic number of the elements. Thus, for example, for medium atomic number



elements, the best transmission was obtained at the symmetry position or slightly positive of the second-order Bragg position.

In order to gain some insight into the transmission properties for the three systematic sets in HCP cobalt, theoretical calculations of rocking curves have been carried out. These profiles give information of the diffracted beam intensity as a function of the deviation parameter ( $\Delta\theta_g$ ) at constant crystal thickness. Figs. 4.21a, b show the bright field rocking curves obtained when the (0 0 2) and (1 0 0) systematic sets are excited. The crystal thickness assumed was 4000Å and the accelerating voltage was taken to be 100KV. It is clear from this figure that for the (0 0 2) set, the best transmission is obtained at a value of  $\Delta\theta_g$  slightly positive of the first order reflection at its Bragg condition ( $\Delta\theta_g=0.0$ ). This result is similar to that obtained for FCC materials (see Humphreys et. al.1971). However, in the (1 0 0) case, the best transmission is obtained at a value of  $\Delta\theta_g$  slightly positive of the second order reflection in its Bragg condition ( $\Delta\theta_g=1.0$ ). On the other hand, for higher accelerating voltages (1000KV), Figs. 4.22a, b show that the orientation for best transmission in the (0 0 2) case is slightly positive of the second order reflection at its Bragg condition. However, for the (1 0 0) the transmission characteristics are similar at both low and high accelerating voltages.





In the dark field case, Humphreys et. al. (1971), have shown that for FCC materials and for 100KV electrons, the best transmission orientation corresponds to the exact Bragg condition of the first order reflection. As the electron energy is increased (1000KV) and for medium atomic number elements, the best transmission is obtained slightly positive of the second order Bragg position or slightly negative of the symmetry position ( $\Delta\theta_g = -1.0$ ). Similar results to these are obtained when the (0 0 2) systematic set in HCP materials is excited. However, for the (1 0 0) case, the best transmission at 100KV was found to be slightly positive of the second order Bragg position. This result remains unchanged for accelerating voltages up to 1000KV. It is important to mention that the transmission characteristics for the (1 -1 1) systematic set are very similar to those for the (0 0 2) set and are therefore not presented in this section.

#### 4.5 ON THE RELATIONSHIP BETWEEN THE EFFECTS OF SYSTEMATIC REFLECTIONS AND ACCELERATION VOLTAGE.

It is commonly assumed in calculations of diffraction contrast that many-beam interactions become more important as the electron energy increases. This conclusion is based on the increase in the radius of the Ewald sphere which occurs as the accelerating voltage is raised. Experimental evidence that under certain conditions many-beam interactions become more important as the accelerating



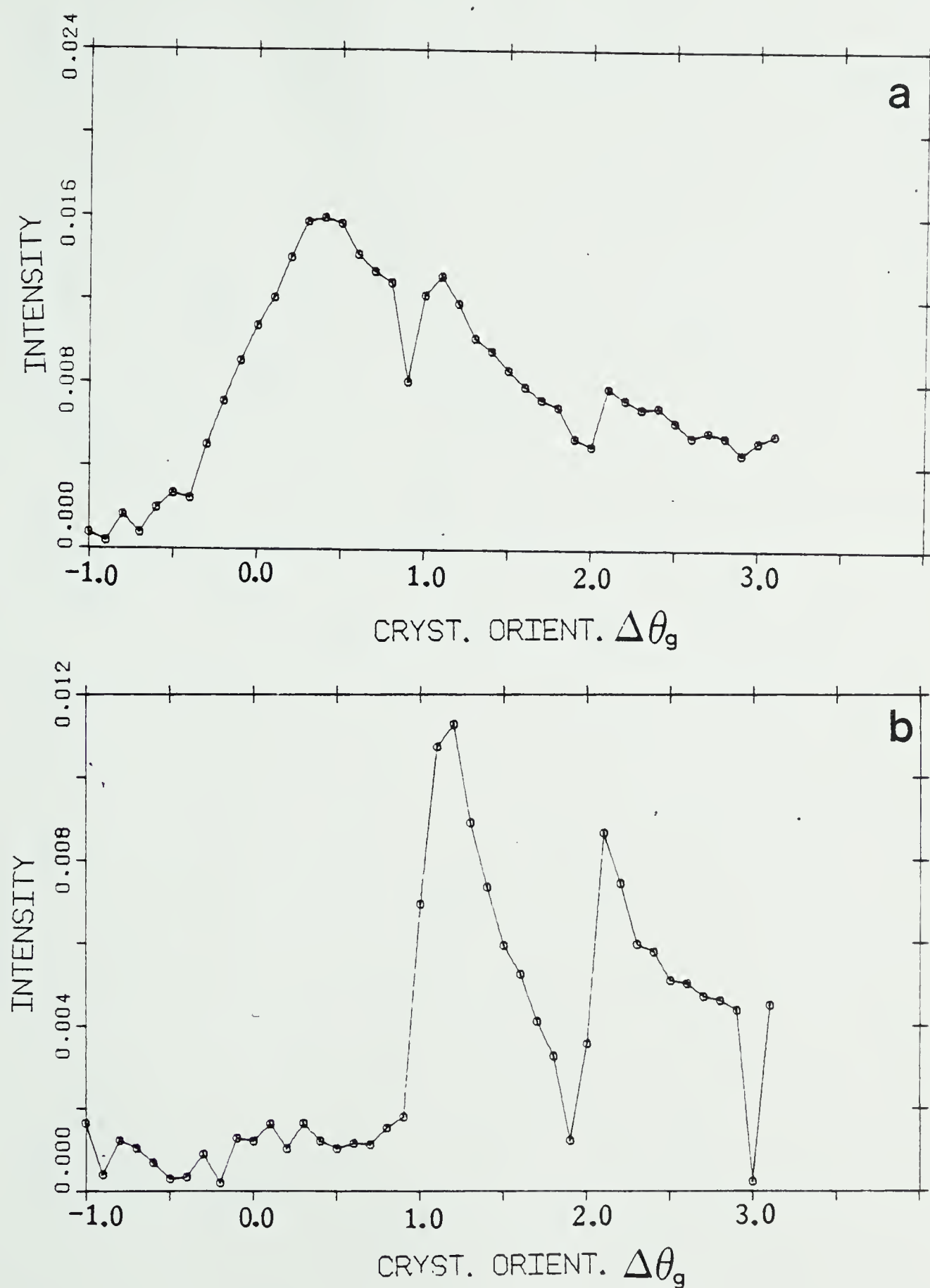


Figure 4.21 Bright field rocking curves at an accelerating voltage of 100KV and crystal thickness of 4000Å. a) (0 0 2) systematic case, b) (1 0 0) systematic case.



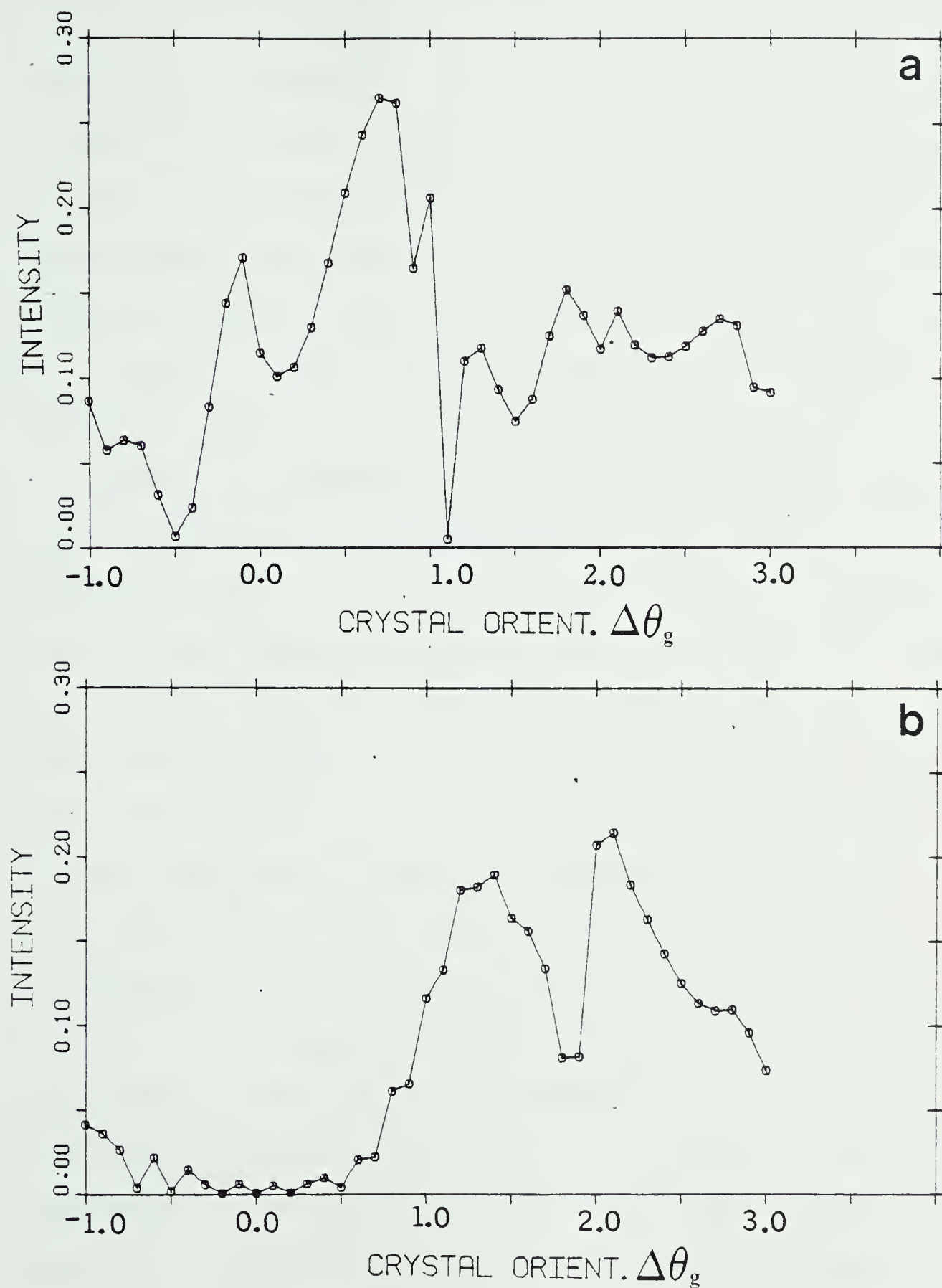


Figure 4.22 Bright rocking curves at an accelerating voltage of 1000KV and crystal thickness of 8000Å. a) (0 0 2) systematic case, b) (1 0 0) systematic case.



voltage increases was first obtained by Dupouy et. al. (1965). These authors studied the variation of the extinction distance as a function of the accelerating voltage in single crystals of MgO. As the accelerating voltage was increased, appreciable differences between the experimental extinction distances and the two-beam theoretical predictions were obtained. However, Goringe et. al (1966) found good agreement with experiment when systematic reflections were taken into account.

These considerations however do not offer any insight into the qualitative differences in the behavior of some systematic sets of reflections such as those which have been found in HCP cobalt (see sections 5.3 and 5.4). In order to gain some understanding of these differences, the relationship between the effects of systematic reflections and the critical voltage has been considered. The critical voltage effect was discovered by Nagata and Fukuhara (1967) and Uyeda (1968). These authors found that at an orientation corresponding to the second order reflection in a systematic set in its Bragg condition ( $\Delta\theta_g=1.0$ ), and at a certain accelerating voltage the intensity of a second order reflection became very weak. In order to explain this phenomenon an approach based on Bloch wave symmetries was presented by Metherell and Fisher (1969) and Lally et. al. (1972). This approach can be understood by writing the expression for the diffracted beam intensity as:





$$I_{2g}(z) = \left| \sum_{i=2,3} C_o^{(i)} C_{2g}^{(i)} \exp[2\pi i \gamma^{(i)} z] \exp[-2\pi q^{(i)} z] + \nabla \right|^2$$

(4.8)

where  $\nabla$  represents the contribution of all Bloch waves except 2 and 3. The magnitude of  $\nabla$  is very small unless the crystal is very thin.

The reduction in intensity which occurs at the critical voltage can be understood by examining the excitation amplitudes and the eigenvalues of Bloch waves 2 and 3 in the above mentioned equation. The values of these parameters at the exact Bragg condition of the (0 0 4) reflection in HCP cobalt and close to the critical voltage are shown in Fig.4.23. It can be seen from this figure that as the accelerating voltage is increased from 150KV to 450KV, the excitation amplitudes of Bloch waves 2 and 3 remain nearly equal in magnitude and of opposite sign while the eigenvalues of these Bloch waves approach each other in value. At approximately 300KV the eigenvalues are degenerate and the excitation amplitudes of Bloch wave 2 and 3 interchange resulting in a change in symmetry of these Bloch waves. Lally et. al. (1972), have defined the voltage at which this change in symmetry occurs to be the critical voltage. The reason for the reduction in the diffracted beam intensity can now be understood by noting that at the critical voltage  $\gamma^{(2)} = \gamma^{(3)}$  while the excitation amplitudes



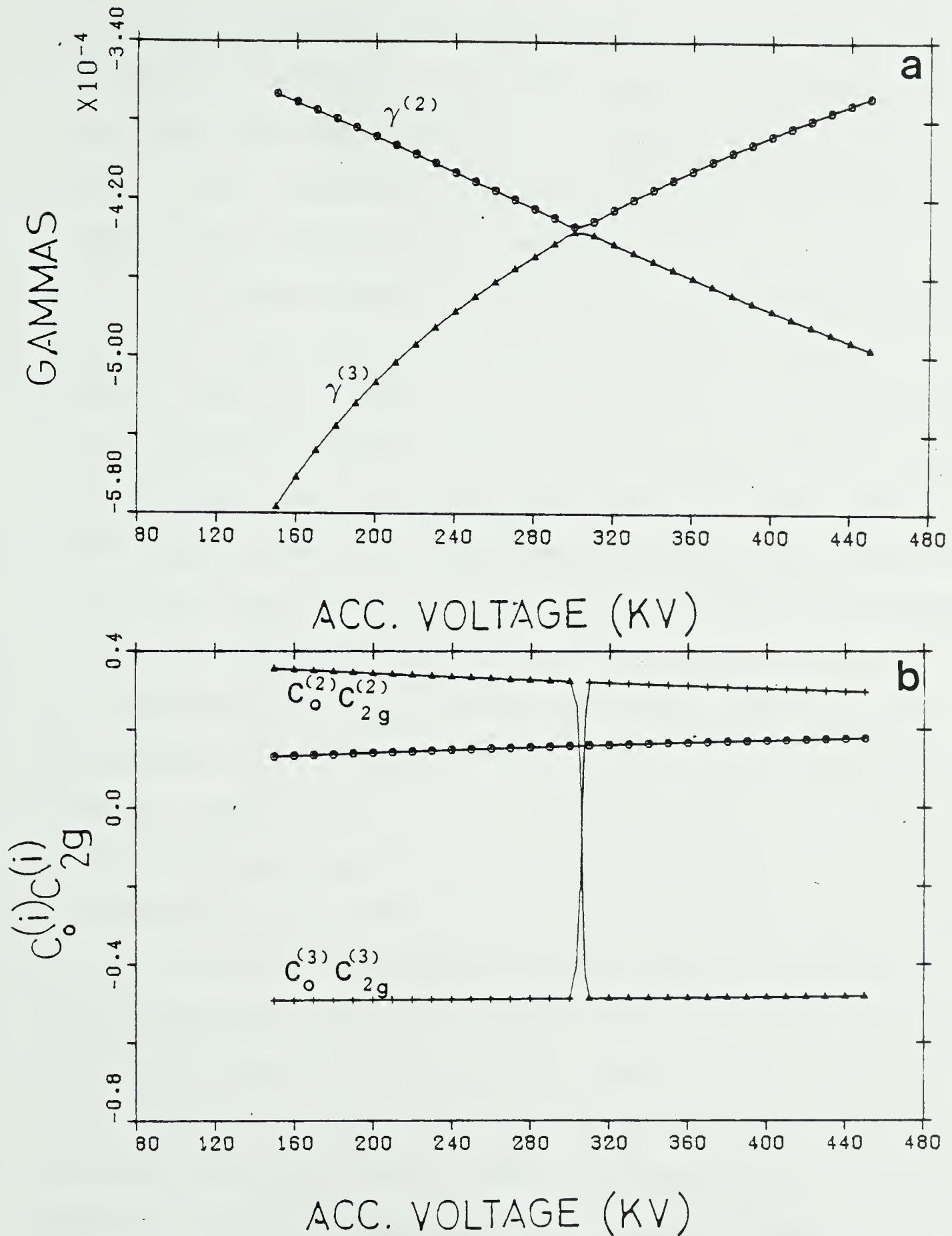


Figure 4.23 This figure shows a) the eigenvalues and b) the excitations amplitudes for Bloch waves 2 and 3 closed to the critical voltage. 13 beams from the (0 0 2) systematic set were taken into account and  $\Delta\theta=0.0$ .



of these Bloch waves are nearly equal in magnitude and are of opposite sign. It can be seen from equation 4.18, therefore, that the contributions made by these two Bloch waves will interfere destructively and an appreciable reduction in intensity will result.

The significance of the critical voltage effect on the effects of systematic reflections in first order dark field images such as those discussed in section 4.3 can now be seen from the following arguments (see, for example Botros et al. 1979). Howie (see Amelinckx et. al. 1978.), has shown that based on the three-beam approximation of the dynamical theory has shown that when the reflection  $2g$  of a systematic set is in the Bragg condition, two of the Bloch waves will be symmetric ( $C_0 = C_{2g}$ ) with  $C_g \neq 0$  while one Bloch will be antisymmetric ( $C_0 = -C_{2g}$ ) with  $C_g = 0$ . Below the critical voltage Bloch wave 3 is antisymmetric while above the critical voltage Bloch wave 2 is antisymmetric. It can therefore be concluded that below the critical voltage  $C^{(3)}_g = 0$  and the two important Bloch waves contributing to the diffracted beam intensity of the first order reflection when the reflection  $2g$  is in the Bragg condition must be Bloch waves 1 and 2. On the other hand, above the critical voltage where  $C^{(2)}_g = 0$  the important Bloch waves must be 1 and 3. Since the important Bloch waves at  $\Delta\theta_g = 0.0$  are 1 and 2, it is not unreasonable to expect that Bloch waves 1 and 2 would be the only important Bloch waves in the entire range  $0.0 \leq \Delta\theta_g \leq 1.0$  below the critical voltage. As a result the





variation of extinction distance with  $\Delta\theta_g$  for this range should be two beam in character.

Above the critical voltage the important Bloch waves at  $\Delta\theta_g=0.0$  would again expected to be 1 and 2. However, as noted above, at  $\Delta\theta_g=1.0$  the important Bloch waves must be 1 and 3. A drop in extinction distance from  $1/(\gamma^{(1)}-\gamma^{(2)})$  to  $1/(\gamma^{(1)}-\gamma^{(3)})$  must therefore occur somewhere in the range  $\Delta\theta$  from 0.0 to 1.0. This drop can only occur as a result of an interchange in the importance of Bloch waves 2 and 3, implying that at some value of  $\Delta\theta_g$  in this range, Bloch waves 2 and 3 must contribute equally to the diffracted beam intensity. Together with Bloch wave 1, this gives three important Bloch waves and therefore complex intensity profiles will in general result.

The reciprocal lattice vectors  $\vec{g}_{(100)}$ ,  $\vec{g}_{(002)}$  and  $\vec{g}_{(1-11)}$  are very nearly the same in magnitude (0.46, 0.49 and 0.52  $\text{\AA}^{-1}$  respectively). However, the results presented in the dark field case in Figs. 4.6, 4.7 and 4.8 have shown that the effects of systematic reflections in the (1 0 0) case are different from these effects in the other two systematic sets. One of the most important differences in their behavior being in the range of  $\Delta\theta_g$  closed to 1.0 (i. e. the second order reflection closed to its Bragg condition). This result can now be understood by estimating the critical voltages for the (2 0 0), (0 0 4) and (2 -2 2) reflections. The critical voltage for the (2 0 0) was found to be large in magnitude but negative. Thus for the (1 0 0)





systematic set the accelerating voltage (150KV) is higher than the critical voltage and the many beam effects associated with the strong excitation of Bloch wave 3 at  $\Delta\theta_g=1.0$  would be expected, as was in fact, found to be the case. For the (0 0 4) reflection, the critical voltage was found to be approximately 300KV (see Fig. 4.23) which is above the accelerating voltage used in obtaining the results presented in section 4.3. From the previous discussion two-beam like behavior should, therefore, be obtained for the (0 0 2) systematic set in the range of  $\Delta\theta_{(002)}$  from 0.0 to 1.0 as was in fact found to be the case. The critical voltage for the (2 -2 2) reflection was found to be small in magnitude (approximately 8KV). Thus, following the arguments of the (1 0 0) case, it would be expected that as the crystal is tilted from  $\Delta\theta_{(1-11)}=0.0$  to 1.0 a change in extinction distance from  $1/(\gamma^{(1)}-\gamma^{(2)})$  to  $1/(\gamma^{(1)}-\gamma^{(3)})$  must occur. However, the results shown in Fig.4.6 do not indicate that such a change takes place. This can be understood from the many-beam dispersion surface for this systematic set which indicates that close to  $\Delta\theta_g=1.0$ , the wave vectors of Bloch waves 2 and 3 are nearly the same in magnitude and thus  $1/\gamma^{(1)}-\gamma^{(2)} \cong 1/\gamma^{(1)}-\gamma^{(3)}$ .

The main conclusion which can be drawn from this discussion is that in assessing the significance of the accelerating voltage in determining whether or not effects of systematic reflections will be important at orientations close to strong beam conditions, it is not the accelerating



voltage itself but rather its value relative to the critical voltage that should be considered.

#### 4.6 DISCUSSION

Of the results presented in the previous sections of this chapter the most important practical implications are concerned with defect imaging using the commonly occurring (1 0 0) set of systematic reflections. As has been mentioned in section 5.4 under strong beam conditions the image intensity and the beam transmission are unusually low and the extinction distance is very large compared to typical values obtained in FCC materials for low order reflections (see Hirsch et al. 1977). As a result for the (1 0 0) case, the maximum specimen thickness in which defects can easily be observed is small and defects such as dislocations will have unusually wide images (see for example, Jones 1978). Furthermore, because anomalous absorption effects are weak, the conventional methods for identifying the nature of stacking faults can not be used since they are based on strong anomalous absorption effects being present (see Hirsch et al. 1977). Although the beam transmission can be improved by tilting the crystal to the Bragg position of the second order reflection (2 0 0), the extinction distance, in the bright field case at least, is even larger than when the reflection (1 0 0) satisfies its Bragg condition. Another commonly occurring systematic set of reflections in HCP materials to which an electron microscopist might resort is



the  $(0\ 0\ 2)$  systematic set. However, choosing the  $(0\ 0\ 2)$  reflections might render defects such as stacking faults virtually invisible owing to the values of the phase angle  $\alpha$  ( $0$  or  $\pm 2\pi$ ), (see chapter 5 for a detailed discussion). Therefore, a number of imaging problems can be seen to remain if the  $(1\ 0\ 0)$  or the  $(0\ 0\ 2)$  systematic sets are excited. The work presented in this chapter has shown however that by choosing the  $(1\ -1\ 1)$  systematic set some of the difficulties can be overcome. Thus, for example, under strong beam conditions ( $\Delta\theta_{(1\ -1\ 1)}=0.0$ ), strong anomalous absorption and good beam transmission are obtained (see section 4.4.1) and the imaging problems mentioned for the  $(1\ 0\ 0)$  set are not present in this case. Also, the phase angles  $\alpha$  obtained for the different types of stacking faults in HCP materials are different and therefore the nature of these defects might be obtained from a single electron microscope image (see chapter 5 for a detailed discussion).





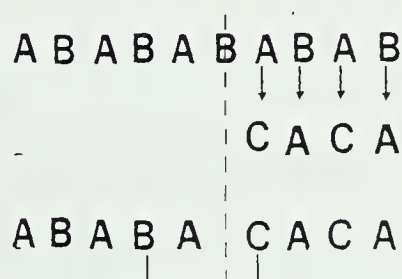
## CHAPTER V

### EFFECTS OF SYSTEMATIC REFLECTIONS ON THE STACKING FAULT

#### IMAGE CONTRAST IN HCP COBALT

##### 5.1 INTRODUCTION

In the hexagonal close packed structures the closed packed planes are the (0 0 2) planes. These basal planes are also the most frequently occurring slip planes in HCP crystals. In these types of materials there are three kinds of stacking faults. Two of them are intrinsic,  $I_1$  and  $I_2$  and the other is extrinsic, E (see for example Hirth and Lothe 1968). The intrinsic fault  $I_1$  can be formed by the removal of a basal plane and a shear, as is illustrated below:

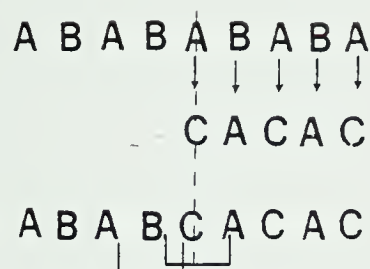


An estimate of the stacking fault energy can be obtained using a scheme giving by Hirth and Lothe (1968). In this scheme the number of pairs of second nearest neighbor planes which are not in the proper stacking sequence are counted. Thus, as is indicated above, for the intrinsic fault  $I_1$ , there is one pair of second nearest neighbor planes in the wrong stacking sequence. The fault  $I_2$  can be formed directly by shear as is illustrated

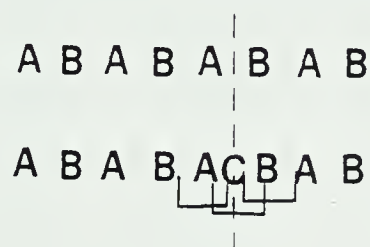




below:



As can be seen from this diagram, there are two violations of the second nearest neighbor sequence and therefore the relative stacking fault energy is about twice that for the  $I_1$  case. The extrinsic fault  $E$  is formed by inserting a C plane in the perfect crystal AB sequence



There are in this case, three violations of the second nearest neighbor sequence and therefore the stacking fault energy of this fault is about three times the energy of an  $I_1$  and one and a half that of an  $I_2$  fault. (see Hirth and Lothe 1968).

## 5.2 DISPLACEMENT VECTORS AND PHASE ANGLES OF STACKING FAULTS IN HCP STRUCTURES

The displacement vectors  $\vec{R}$  corresponding to the three different types of stacking faults in HCP materials can be obtained by using a representation given by Berghezan et. al. (1961) which is shown in Fig 5.1. The displacement vectors using this representation are given by:



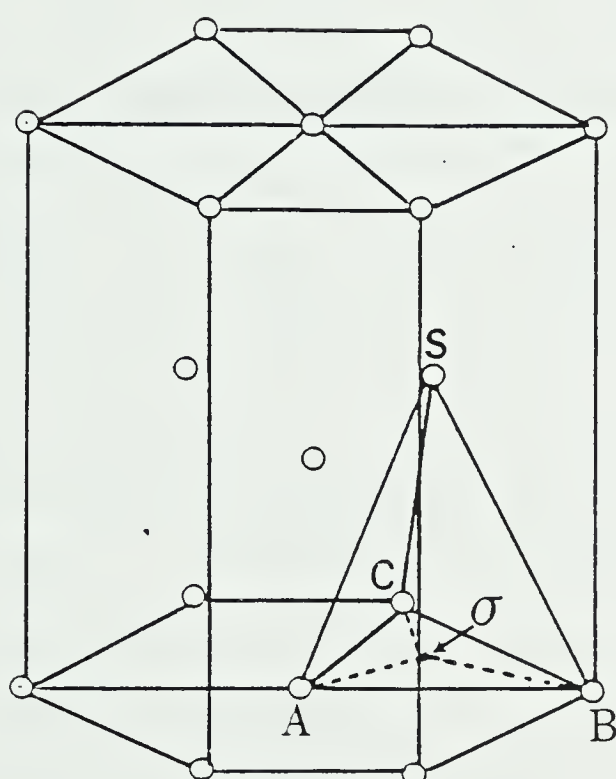


Figure 5.1 Displacement vectors  $R$  in the hexagonal close packed lattice



$$\begin{array}{l}
 \begin{array}{c} \rightarrow \rightarrow \quad \rightarrow \rightarrow \\ I_1 : R = A\sigma + \sigma S = AS \end{array} \\
 \begin{array}{c} \rightarrow \rightarrow \\ I_2 : R = A\sigma \end{array} \\
 \begin{array}{c} \rightarrow \rightarrow \\ E : R = \sigma S \end{array}
 \end{array}$$

On the other hand, some of the most commonly occurring sets of systematic reflections in HCP structures are the  $(1\ 0\ 0)$ ,  $(0\ 0\ 2)$  and  $(1\ -1\ 1)$  sets. One of the most important parameters influencing the role that systematic reflections play on stacking fault image contrast is the phase angle of the fault,  $\alpha = 2\pi \mathbf{g} \cdot \mathbf{R}$ . The stacking fault phase angle  $\alpha$ , obtained for each of the above mentioned types of stacking faults ( $I_1$ ,  $I_2$  and  $E$ ) using the HCP low order systematic sets of reflections ( $(1\ 0\ 0)$ ,  $(0\ 0\ 2)$  and  $(1\ -1\ 1)$ ) are given in Fig. 5.2. Fig. 5.2 shows, for example, that by using the commonly occurring  $(1\ 0\ 0)$  set of systematic reflections, the intrinsic stacking faults,  $I_1$  and  $I_2$  have the same phase angle  $\alpha$ , and therefore the image contrast exhibited by these two types of faults would be identical under these diffraction conditions. On the other hand, the extrinsic stacking fault produces a phase angle  $\alpha = 0$ , and therefore this type of fault would be invisible.

When the  $(0\ 0\ 2)$  set of systematic reflections is excited Fig. 5.2 shows that all three types of stacking faults produce the same phase angle  $\alpha$  ( $\pm 2\pi$  or  $0$ ) and therefore under these diffraction conditions all stacking faults in HCP materials will be invisible.

The most interesting systematic set from the point of view of imaging stacking faults is the  $(1\ -1\ 1)$  set of



	$I_1$	$I_2$	E
$(1\ 0\ 0)$	$\pm 2\pi/3$	$\pm 2\pi/3$	0
$(0\ 0\ 2)$	$\pm 2\pi$	0	$\pm 2\pi$
$(1\ -1\ 1)$	$\pm \pi/3$	$\pm 2\pi/3$	$\pm \pi$

Figure 5.2 TABLE 2.-Stacking fault phase angles  $\alpha$  obtained using the HCP low order reflections  $(1\ 0\ 0)$ ,  $(0\ 0\ 2)$  and  $(1\ -1\ 1)$ .





reflections. Fig. 5.2 shows that for this set each one of the stacking faults ( $I_1$ ,  $I_2$  and  $E$ ) gives rise to a different phase angle  $\alpha$ . Thus, for example, the extrinsic fault  $E$  produces a value of  $\alpha = \pm\pi$  and the intrinsic stacking faults  $I_1$  and  $I_2$  give rise to different phase angles  $\alpha$ ;  $\pm\pi/3$  and  $\pm 2\pi/3$  respectively. This result suggests the possibility that stacking faults images obtained using the  $(1 \ -1 \ 1)$  set can be used to distinguish between the three different types of stacking faults in HCP materials. The work presented in this chapter explores this possibility.

### 5.3 IMAGE CONTRAST CHARACTERISTICS OF STACKING FAULTS WHEN THE $(1 \ -1 \ 1)$ SYSTEMATIC SET IS EXCITED

In order to investigate the image contrast characteristics of the three types of stacking faults in HCP materials when the  $(1 \ -1 \ 1)$  systematic set is excited, theoretical calculations have been carried out for strong beam diffraction conditions (i. e. the  $(1 \ -1 \ 1)$  reflection at its Bragg condition) and for both bright and dark field images. The bright field results obtained from these two-beam calculations for  $\alpha = \pi/3$ ,  $2\pi/3$  and  $\pi$  stacking faults are shown in Figs. 5.3, 5.4 and 5.5. The profiles were all obtained for a crystal thickness equal to  $1710 \text{ \AA}$  ( $\cong 5.5\xi_0$ ), and an accelerating voltage of 150KV. These figures clearly show that there are significant differences between the profiles corresponding to the three types of stacking faults suggesting a possible method of fault identification.



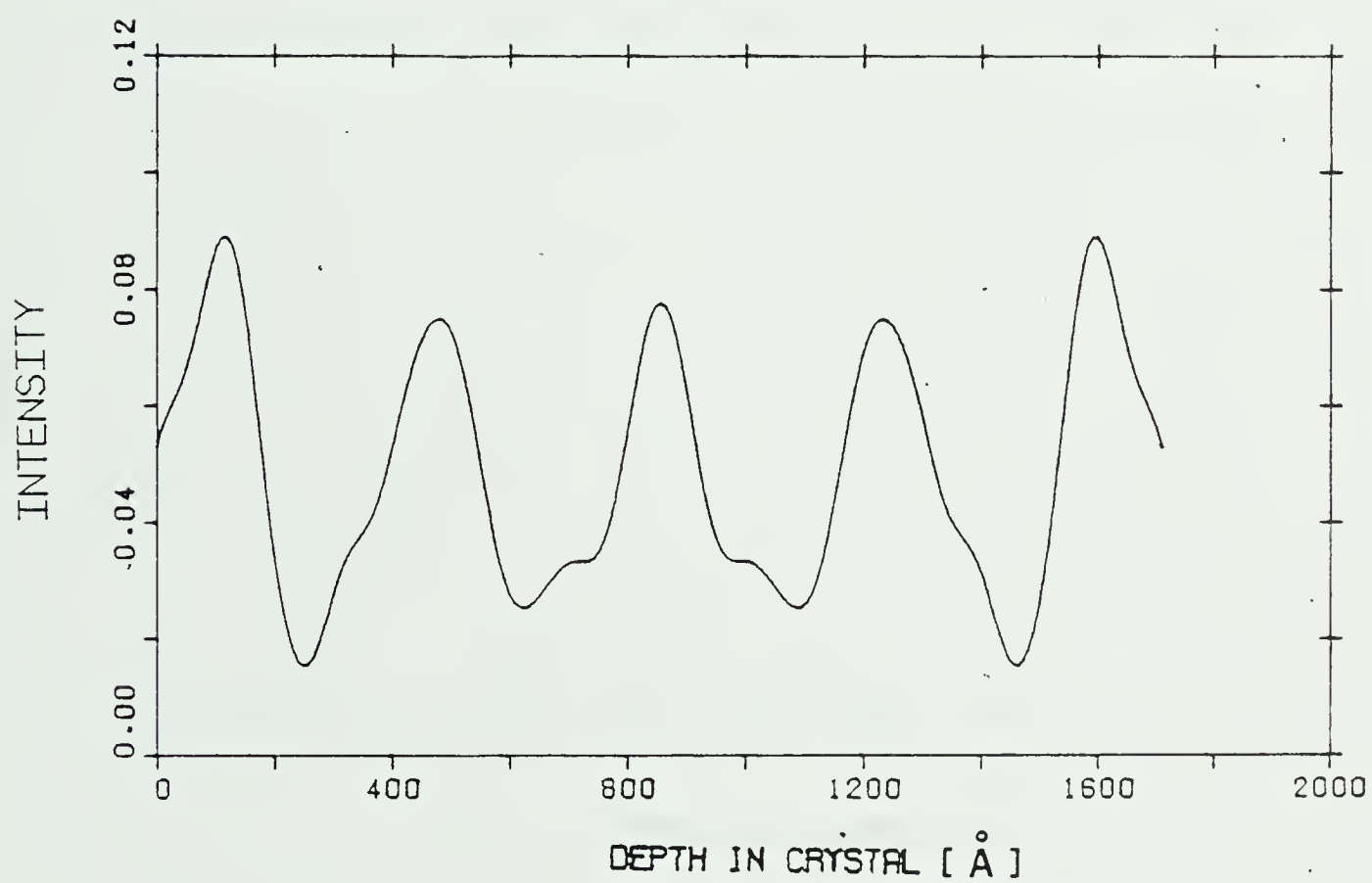


Figure 5.3 Stacking fault profile obtained when the  $(1 \ -1 \ 1)$  reflection satisfies its Bragg condition and for a crystal thickness of 1710Å. The phase angle  $\alpha = \pi/3$ .



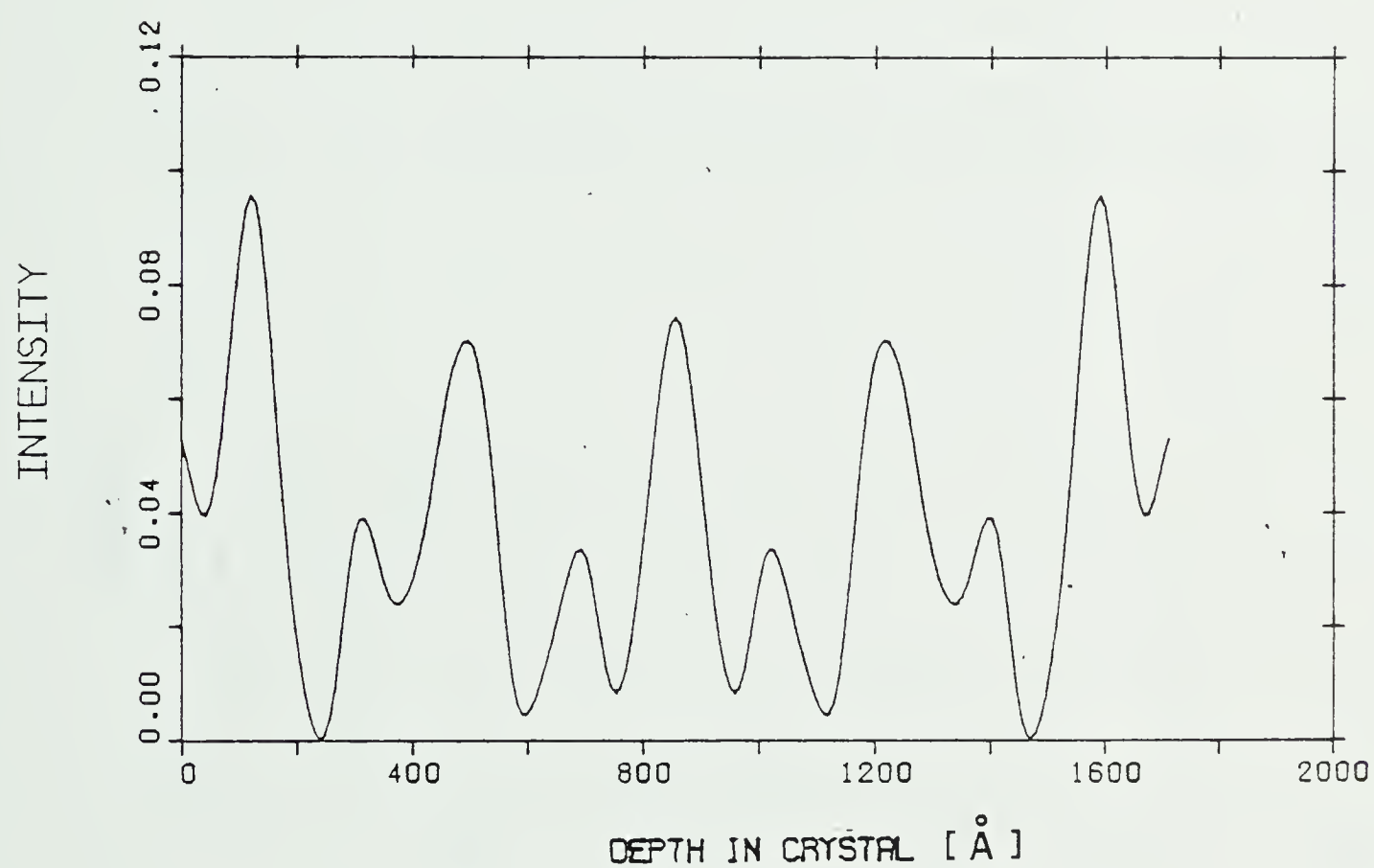


Figure 5.4 Stacking fault profile under the same conditions of the one in Fig. 5.3 but  $a=2\pi/3$ .



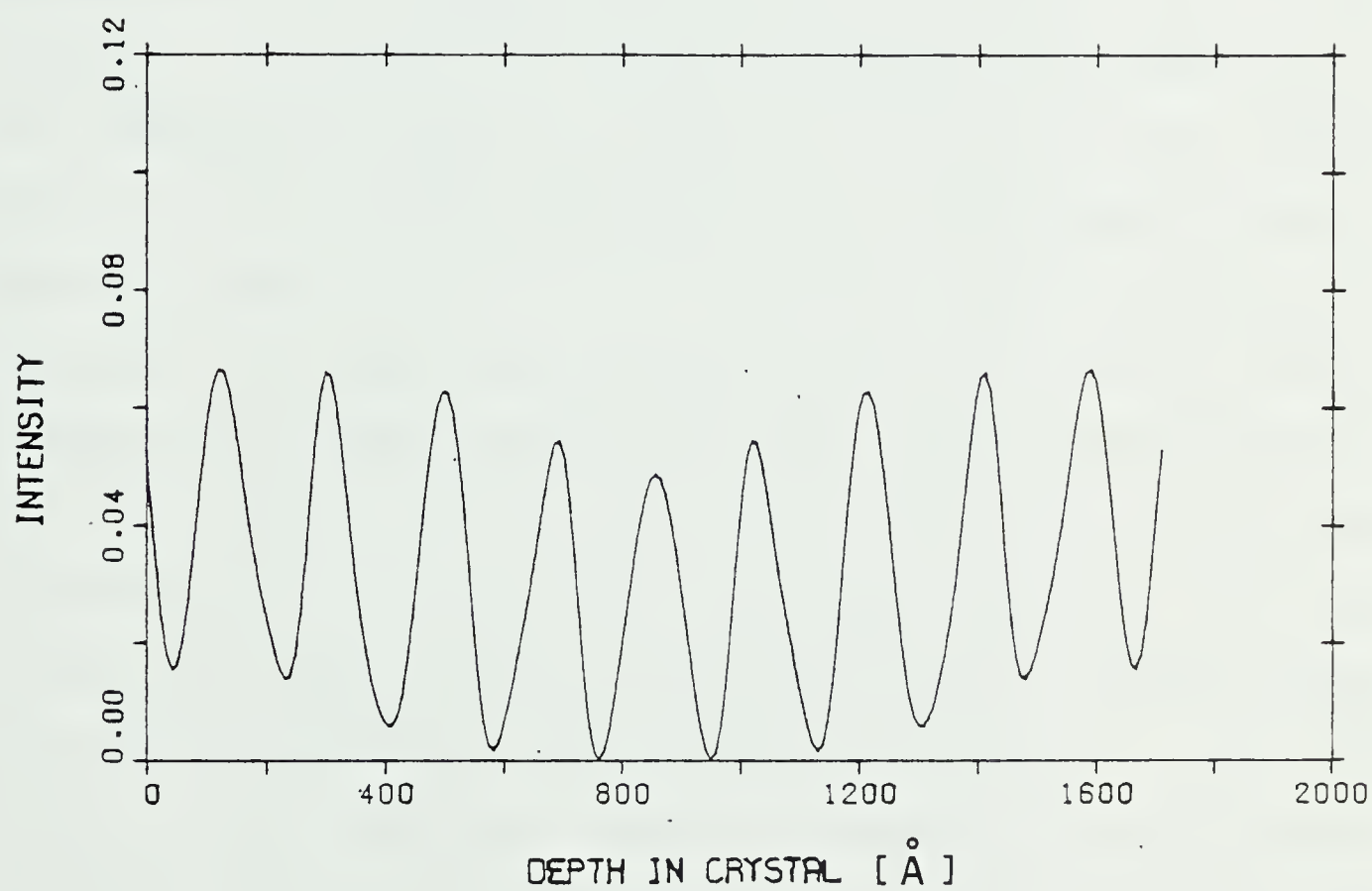


Figure 5.5 Stacking fault profile under similar conditions to that in Fig. 5.3 but  $a=\pi$ .





However, this approach has the disadvantage that the thickness of the specimen in which the fault lies must be known. Also, subsidiary peaks are strongly dependent on the values of the absorption coefficients used in the calculations (see for example Sheinin et. al. 1970) and inaccuracies in these coefficients could result in incorrect conclusions being drawn. An alternative method for fault identification in HCP materials might be to carry out observations in a wedge crystal specimen rather than one of constant thickness. In order to explore this possibility a two-dimensional display of theoretical stacking fault images based on the two-beam approximation of the dynamical theory has been used. Figs. 5.6, 5.7 and 5.8 show the results obtained for bright field images of  $\alpha=\pi/3$ ,  $2\pi/3$  and  $\pi$  faults respectively. These calculations have been obtained assuming that the fault lies in a wedge crystal and the excited reflection  $(1\ -1\ 1)$  satisfies its Bragg condition. It can clearly be seen from these figures that the overall image contrast of the three types of stacking faults ( $I_1$ ,  $I_2$  and  $E$ ) are quite different. Thus, for example, the (extrinsic,  $E$ ) fault in Fig. 5.8 displays parallel fringes which do not change appreciably as the crystal thickness is increased. The image of a  $2\pi/3$  (intrinsic,  $I_2$ ) fault shown in Fig. 5.7 indicate that the fringes in this case are similar to the image of a  $\pi$  fault except that each of the fringes is modulated strongly as the thickness is increased. The  $\pi/3$  (intrinsic,  $I_1$ ) fault shown in Fig. 5.6, on the other hand,



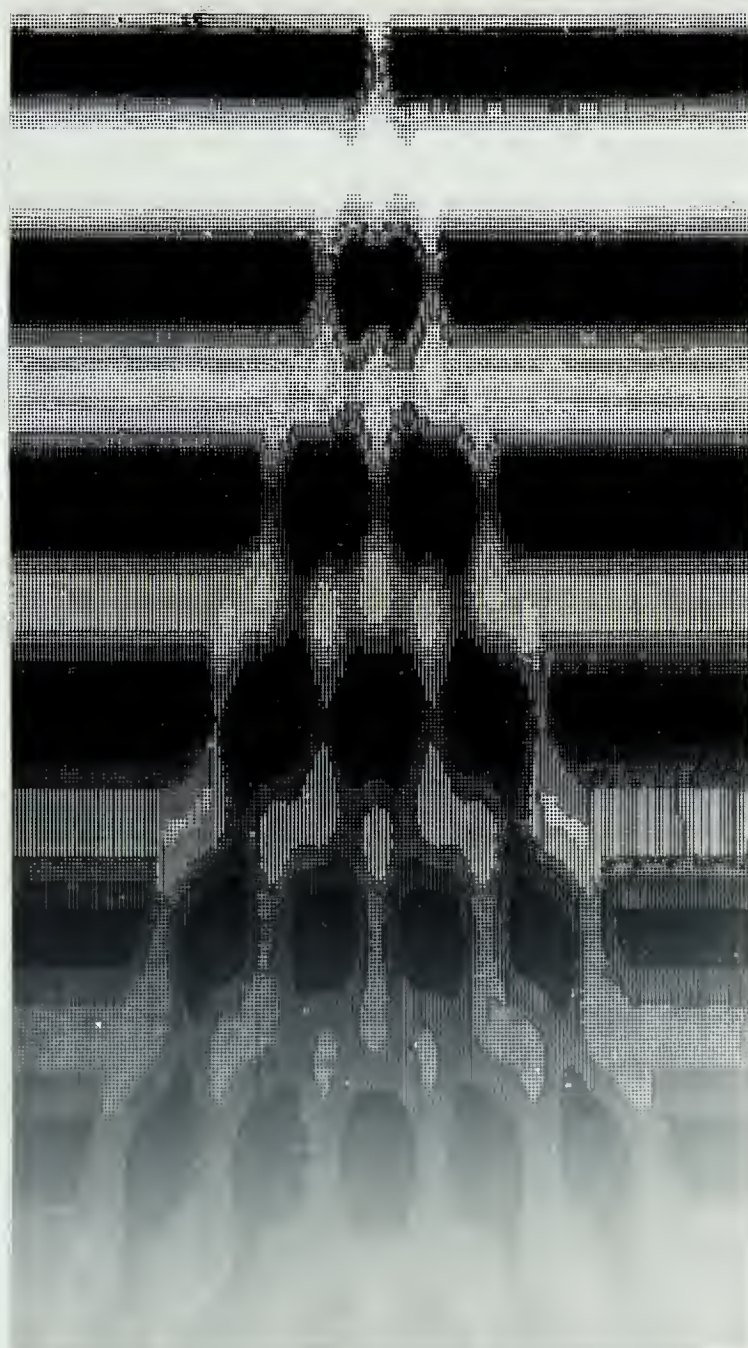


Figure 5.6 Two-dimensional displays of theoretical stacking faults obtained when  $(1 \ -1 \ 1)$  reflection satisfies its Bragg condition in a wedge crystal and  $a=\pi/3$ .





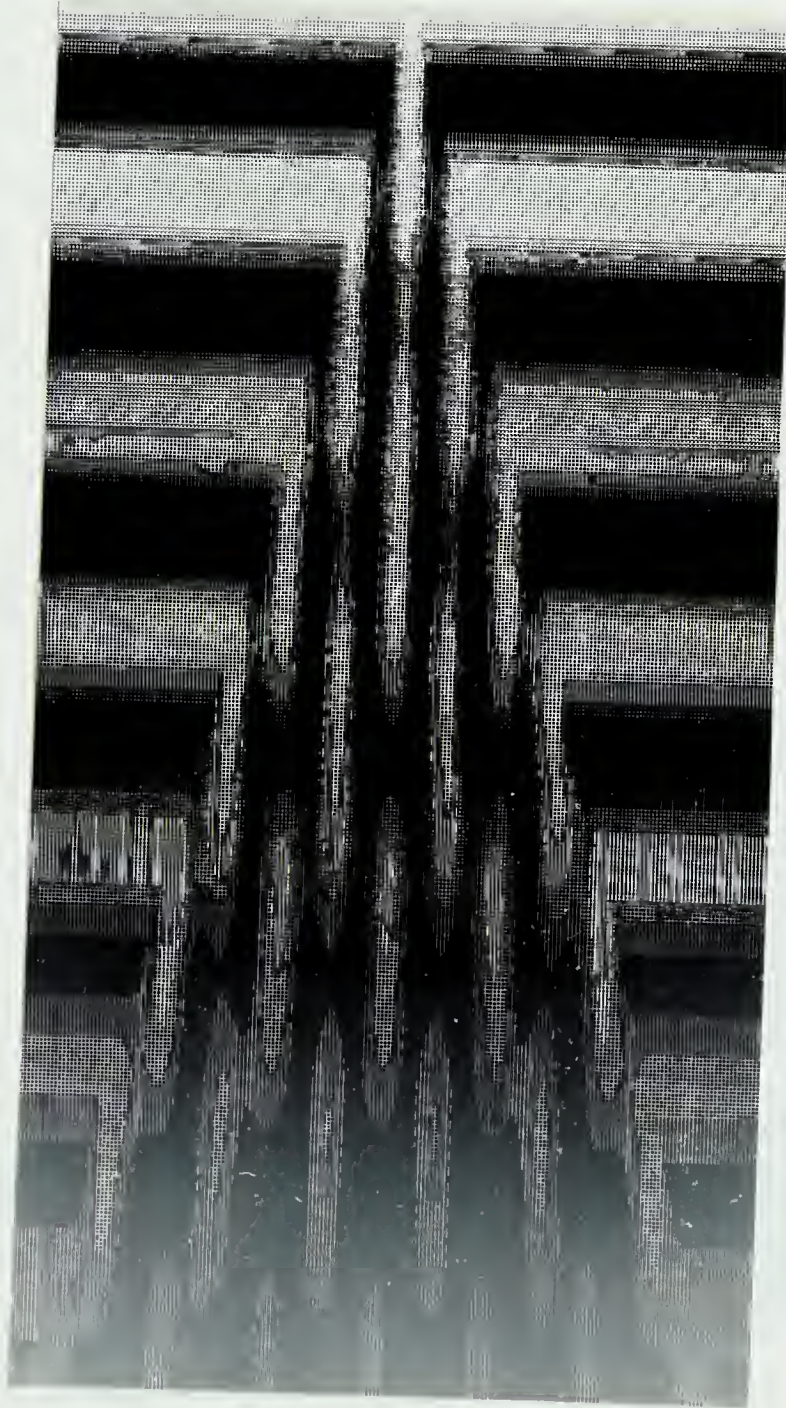


Figure 5.7 Two-dimensional display of a theoretical stacking fault obtained when the  $(1\ -1\ 1)$  reflection satisfies its Bragg condition in a wedge crystal and  $\alpha=2\pi/3$ .



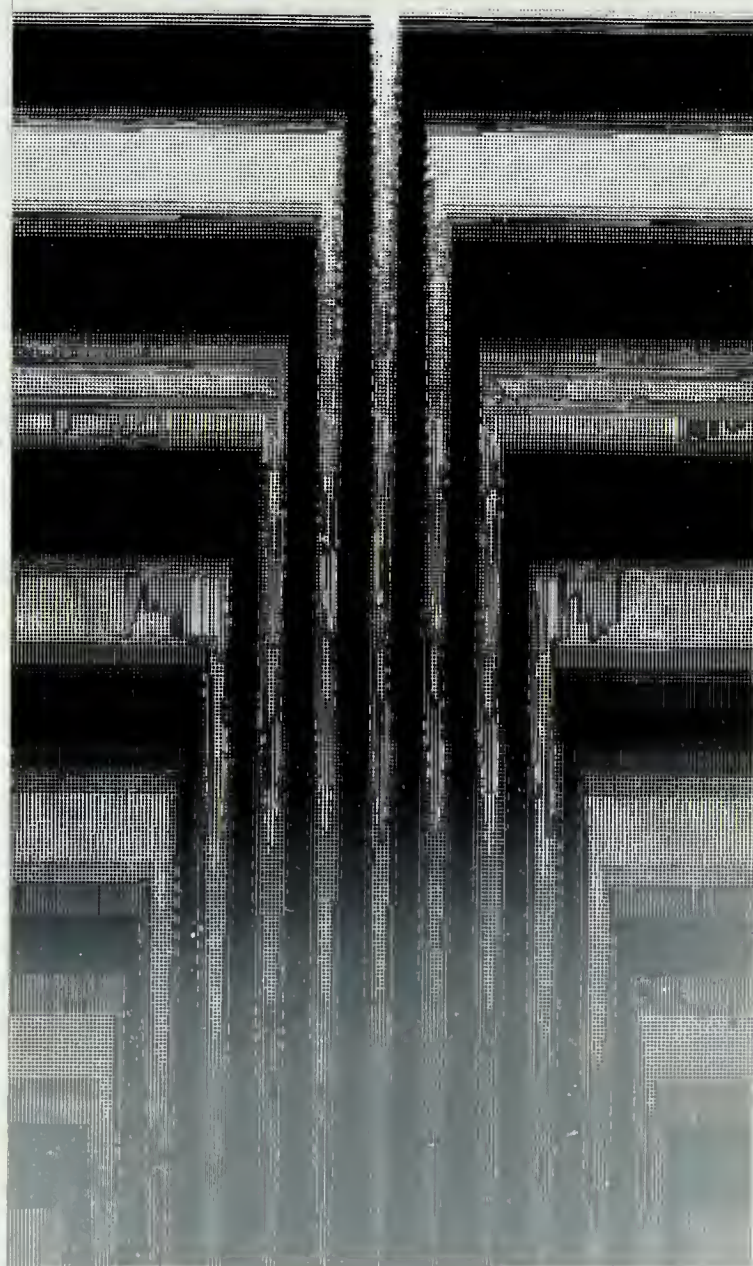


Figure 5.8 Two-dimensional display of a theoretical stacking fault obtained when the reflection  $(1 \ -1 \ 1)$  satisfies its Bragg condition in a wedge crystal and  $a=\pi$ .





can be seen to be quite different from either of the images shown in Figs. 5.7, 5.8. These differences can be seen to be due to a modulation of the fringes with increasing thickness which gives rise to regions of high contrast at thickness of about  $n\xi_0$  and regions of low contrast at thicknesses of about  $(n+1/2)\xi_0$ .

#### 5.4 EXPERIMENTAL RESULTS

In order to test this method of identification experimental stacking faults have been obtained in wedge crystals of HCP cobalt. The experimental procedures are the same as those explained in chapter 4. Fig 5.9 shows a bright field image of a stacking fault obtained when the  $(1 \ -1 \ 1)$  reflection satisfies its Bragg condition. A comparison between this micrograph and the theoretical images, (see Figs. 5.6, 5.7 and 5.8) suggests a reasonable agreement with the  $2\pi/3$  stacking fault case shown in Fig. 5.7. Therefore, this experimental stacking fault should be an intrinsic fault of type  $I_2$ . On the other hand, a comparison between the experimental stacking fault in Fig. 5.10 (obtained under the same diffraction conditions as that in Fig. 5.9), suggests a reasonable agreement with the  $\pi/3$  fault shown in Fig. 5.6. Therefore, this stacking fault must be an intrinsic of type  $I_1$ . It is important to note that extrinsic faults were not observed in our specimens. This is probably related to the high stacking fault energy which this fault possesses (see, for example, Hirth and Lothe 1968 and



Berghezan et. al. 1961).

## 5.5 ANALYSIS OF THE RESULTS IN TERMS OF THE TWO-BEAM APPROXIMATION

The theoretical images of the three types of stacking faults in HCP materials presented in Figs. 5.6, 5.7 and 5.8 can be understood by considering an expression for the bright field stacking fault intensity  $I_0(z)$ , which was obtained by Whelan and Hirsch (1957a). This expression is based on the two-beam approximation when the lowest order reflection  $g$  satisfies its Bragg condition. Also absorption is not taken into account. It is important to note, as can be seen from sections 5.3 and 5.4, that the differences in image contrast for the three types of stacking faults are more pronounced in thin regions of the specimen. Under these circumstances, absorption can be neglected and therefore an analysis in terms of a two-beam approximation without absorption might give a qualitative description of image contrast.

The transmitted beam intensity can be written as:

$$I_0(t, z) = \cos^2\left(\frac{\alpha}{2}\right) \cos^2\left(\frac{\pi t}{\xi_0}\right) + \sin^2\left(\frac{\alpha}{2}\right) \cos^2\left(\frac{2\pi z}{\xi_0}\right) \quad (5.1)$$

where  $\xi_0$  is the extinction distance,  $z$  the crystal thickness and  $t$  is the distance measured from the centre of the crystal to the fault in a direction perpendicular to the surface.





Figure 5.9 Micrograph showing a bright field image of a stacking fault in a wedge crystal of HCP cobalt. The operating voltage was 150KV and  $\Delta\theta_{(1-11)}=0.0$ .





Figure 5.10 Micrograph showing a bright field image of a stacking fault in a wedge crystal of HCP cobalt. The operating voltage was 150KV and  $\Delta\theta_{(1-11)}=0.0$ .





Taking  $t=0$  or  $n\xi_0/2$  where  $n$  is an integer, equation 5.1 can be written for the three types of stacking faults as:

$\pi/3$ .

$$I_O(0 \text{ or } \frac{n\xi_0}{2}, z) = \frac{3}{4} \cos^2\left(\frac{\pi z}{\xi_0}\right) + \frac{1}{4} \quad (5.2)$$

$2\pi/3$ .

$$I_O(0 \text{ or } \frac{n\xi_0}{2}, z) = \frac{1}{4} \cos^2\left(\frac{\pi z}{\xi_0}\right) + \frac{3}{4} \quad (5.3)$$

$\pi$ .

$$I_O(0 \text{ or } \frac{n\xi_0}{2}, z) = 1 \quad (5.4)$$

Thus according to equation 5.4, the centre of a  $\pi$ -fault (and other points for which  $t=n\xi_0/2$ ) should have the same intensity, independent of the crystal thickness. However, the  $2\pi/3$ -fault should show intensity modulations (with thickness) between  $3/4$  to  $1$  (assuming  $1$  to be the incident intensity). In the  $\pi/3$  case the same intensity modulations in the stacking fault fringes are present but in this case the modulation is much stronger, between  $1/4$  to  $1$ . Therefore the behavior of the stacking fault fringes as the thickness of the crystal is increased for the three different types of stacking faults ( $I_1$ ,  $I_2$  and  $E$ ) can be qualitatively understood.



## 5.6 CONCLUSIONS

In a FCC material the basis for determining the nature of stacking faults depends on strong anomalous absorption being present (see, for example, Hirsch et. al. 1977).

In HCP cobalt, when the commonly occurring (1 0 0) set of systematic reflections is excited and  $\Delta\theta_{(100)}=0.0$  (i. e. the reflection (1 0 0) satisfies its Bragg condition), anomalous absorption is almost absent. The stacking faults obtained under these diffraction conditions are therefore symmetric with respect to the middle of the foil both in the bright and dark field cases. Furthermore, the phase angle  $\alpha$  obtained for both types of intrinsics ( $I_1$  and  $I_2$ ) is the same and therefore the same image contrast is obtained. Clearly, the identification of the nature of these defects under these particular circumstances presents serious difficulties. On the other hand, when the (0 0 2) systematic set of reflections are excited the phase angle  $\alpha$  obtained for the different types of stacking faults are  $\pm 2\pi$  or 0, and therefore they are invisible and nothing can be learned about their nature.

The work presented in this chapter leads to the obvious conclusion that when the identification of the nature of the stacking fault in HCP cobalt is required, the best systematic set of reflections which can be used is the (1 -1 1). It is important to point out that these results are more general and can be applied to different HCP metals. Also the same properties presented in this chapter for the (1 -1 1)



set are found in other systematic sets of reflections which are in the same class ( as defined by Jones (1978). ), (like for example  $(0\ 1\ -1)$ ,  $(-1\ 0\ 1)$ ). Therefore there is a number of other systematic sets of reflections commonly found in HCP materials which can be used in the identification procedure.



## CHAPTER VI

### DYNAMICAL THEORY OF TWIN BOUNDARY CONTRAST INCLUDING EFFECTS OF COMMON REFLECTIONS

#### 6.1 INTRODUCTION

Past investigations, (see for example, Vitek 1970, Bristowe et. al. 1975, Yamaguchi et. al. 1976.), based on computer simulation of twin boundary structure assuming empirical interatomic potentials, have shown that a relative translation of one crystal with respect to the other may exist (see Fig. 6.1). A problem of considerable interest to the materials scientist is the development of an experimental method for the determination of the rigid body translation vector  $\vec{T}$  for twins in various materials. The method first proposed in the literature was based on the assumption that only common reflections are excited (see Pond et. al. 1976, Pond 1978.). In this method theoretical images of twin boundaries can be obtained by using the conventional form of the dynamical theory applicable to stacking faults where the phase factor  $\alpha$  is taken to be  $2\pi\vec{g}\cdot\vec{T}$  (where  $\vec{g}$  is the diffracted beam vector and  $\vec{T}$  is the rigid body translation vector). However, as was indicated in chapter 3, non-common and forbidden reflections are, in general, also excited when a twin boundary is present. These reflections can have a significant effect on the contrast in electron microscope images of twin boundaries and it is, therefore, clearly desirable that their effect be taken into





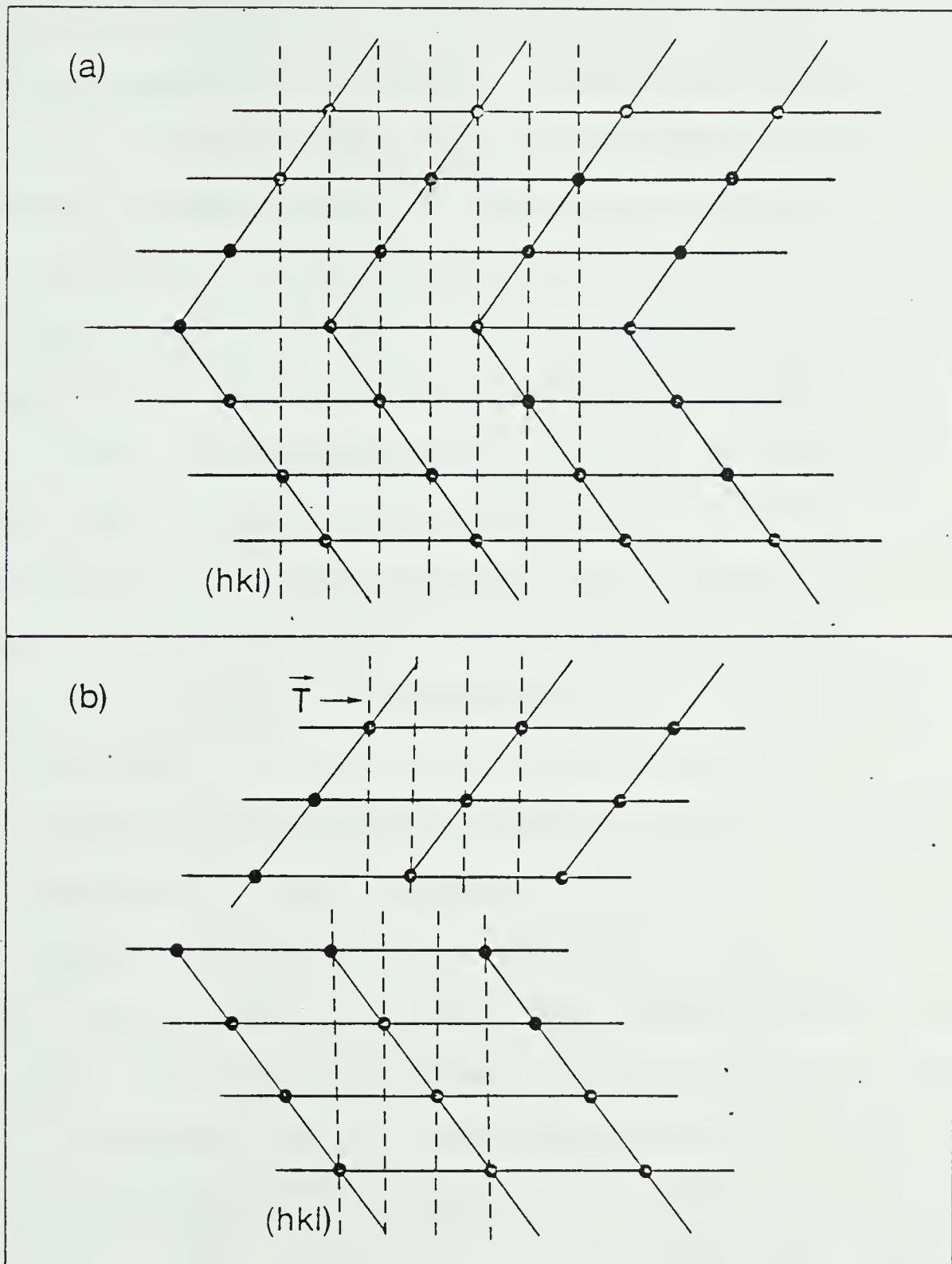


Figure 6.1 Two possible structures for a twin boundary. a) the symmetrical boundary and b) the displaced boundary. The broken lines denotes the reflecting planes which give rise to common reflections.



step in developing a theory which would take all three types of reflections into account was taken by Sheinin and Corbett (1976), who presented a theory of twin boundary contrast in which non-common and forbidden reflections only could be taken into account. Their theory was based on the concept of dynamically coupled sets of diffracted beams, each set being associated with a reflection incident on the lower twin from the upper matrix (see Fig. 6.2). An extension of the theory of Sheinin and Corbett which also permits common reflections to be taken into account was first given by Sutton and Pond (1979), who noted that contributions to the diffracted beam amplitude in the twin may arise from a number of diffracted beams in the matrix. Sutton and Pond took this into account through a linear superposition of each of these contributions.

The method of Sutton and Pond has been criticized in the literature from a number of points of view. Gomez et. al. (1980), for example, have pointed out that the method of Sutton and Pond involves the diagonalization of one dynamical matrix for each beam incident on the twin from the matrix crystal. As a result they feel that the method of Sutton and Pond is not suitable if a large number of beams are taken into account or if more than two crystals are considered. In addition Gomez et. al. have suggested that there are errors in the dynamical matrices of Sutton and Pond (1978) which become more serious as the number of beams taken into account becomes smaller. Gratias and Portier



(1980) have made what appears to be a more fundamental criticism of the method of Sutton and Pond. They indicate that when the diffracted sets in the theory of Sheinin and Corbett are used to describe the case where common reflections are taken into account, as was done by Sutton and Pond, some dynamical couplings are ignored. They argue that the method of Sutton and Pond could be extended to the common reflection case but would require that the diffracted sets be differently defined. In preference to this approach Gratias and Portier have chosen to derive their own formulation of the theory based on a Darwin equation approach.

The situation which at the present confronts the electron microscopist who is attempting to understand the image contrast obtained from twin boundaries can be summarized as follows: 1) If no common reflections are strongly excited then no difficulty appears to be present. The theory of Sheinin and Corbett, which is applicable in this case, has not been disputed in the literature and has been verified experimentally (see for example Sheinin et. al. 1976, Corbett et. al. 1976.). 2) If common reflections are to be taken into account, the electron microscopist is confronted with two quite different forms of the theory (see Sutton et. al. 1978, Gratias et. al. 1980.). The question as to whether or not these two forms of the theory are equivalent or, in fact, whether one form is correct while the other is incorrect remains. It is evidently important





that this situation be clarified. In order to accomplish this we first noted that a form of the theory of twin boundary contrast including effects of common reflections and based on a Bloch wave approach has not been presented in the literature. Therefore, we undertook to derive a form of the theory applicable to this case which is based on this approach. The results obtained are presented in the next section, In following sections, these results are compared to the methods of Sutton and Pond (1978), and Gratias and Portier (1980) and some conclusions are drawn.

## 6.2 DYNAMICAL THEORY FOR TWIN BOUNDARY CONTRAST

### 6.2.1 BLOCH WAVES IN THE TWIN

The object of this section is to present a theory which permits the calculation of diffracted beam intensity at the bottom surface of the twinned crystal shown in Fig. 6.2. In order to carry out such calculations the wave functions describing electrons in the twin must first be known. These can be obtained by first noting that in the case of a single crystal specimen there is a diffracted beam associated with each reciprocal lattice vector. In the twinned crystal the situation is more complex since any reflection in the twin,  $\vec{r}_k$ , can be obtained by the diffraction of a matrix reflection by the twin crystal. This can be expressed in the following way:





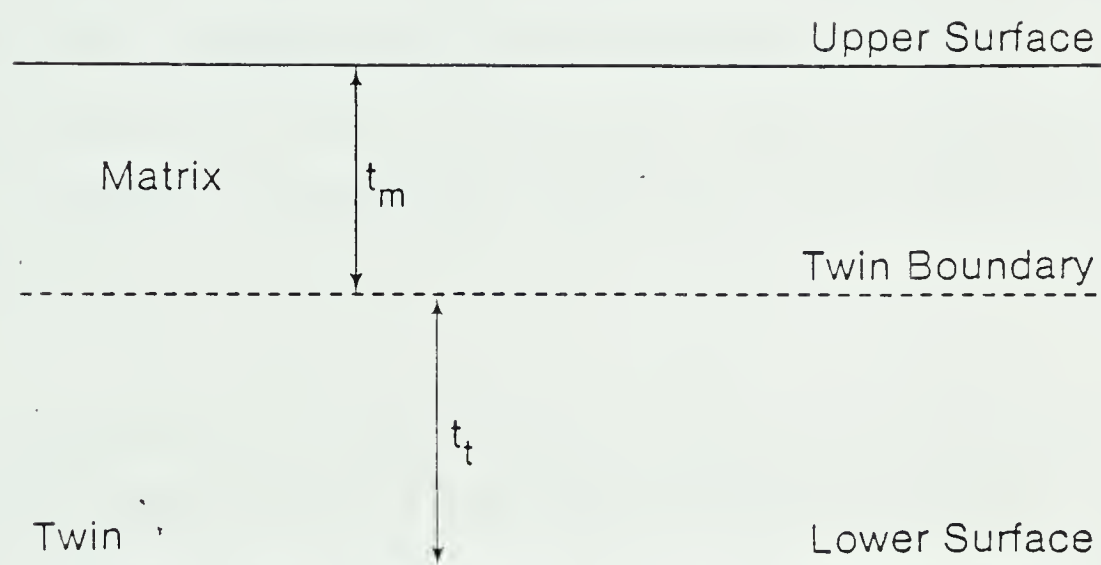


Figure 6.2 Schematic diagram showing a twin boundary in a specimen of total thickness  $t$ . The twin boundary is shown in a configuration appropriate to the column approximation being made.



$$\vec{r}_K = \vec{g}_j + \vec{q}_m + \vec{h}_n \quad (6.1)$$

where  $\vec{q}_m$  is a reciprocal lattice vector in the coincidence lattice,  $\vec{h}_n$  is a reciprocal lattice vector in the twin and  $\vec{g}_j$  is a reciprocal lattice vector in the matrix. Since any reflection in the twin can be represented by eq. 6.1, it follows that a Bloch wave describing electrons in the twin should have components in the directions  $\vec{g}_j + \vec{q}_m + \vec{h}_n$ . The most general function which satisfies these requirements and still retains the essential characteristics of a Bloch wave is given by:

$$b^{(i)} = \exp[2\pi i(\vec{k}^{(i)} + \vec{g}_j) \cdot \vec{r}] \sum_m \sum_n C_{\vec{g}_j + \vec{q}_m + \vec{h}_n}^{(i)} \exp[2\pi i(\vec{q}_m + \vec{h}_n) \cdot \vec{r}] \quad (6.2)$$

where the sum over  $m$  is the sum over all reciprocal lattice vectors in the coincidence lattice and the sum over  $n$  is the sum over all reciprocal lattice vector in the twin. It is important to note that the double sum in 6.2 has the periodicity of the twin lattice since  $\vec{q}_m$  is also a reciprocal lattice vector in the twin. 6.2 is therefore an acceptable Bloch wave for the twin since it consists of a plane wave:

$$\exp[2\pi i(\vec{k}^{(i)} + \vec{g}_j) \cdot \vec{r}] \quad (6.3)$$

modulated by a double sum which is a function having the periodicity of the twin lattice.



### 6.2.2 DYNAMICALLY COUPLED SETS OF DIFFRACTED BEAMS

It is next of interest to ask what diffracted beams are generated by the various Bloch wave components in 6.2. The answer to this question can best be seen by referring to Fig. 6.3 and by considering a particular matrix reciprocal lattice vector,  $\vec{g}_j$ , in 6.1. For example, if  $\vec{g}_j = \vec{g}_1$ , it can readily be seen that the reflections corresponding to  $\vec{g}_1 + \vec{q}_m + \vec{h}_n$  (where  $m, n$  can assume any value) must lie in the set defined by the net of dotted lines. Further, it can be seen that dynamical coupling exists between all reflections in this set and that there is no dynamical coupling between reflections in this set with any reflections outside the set. Clearly, therefore, a particular matrix reciprocal lattice vector,  $\vec{g}_j$ , in 6.2 defines a Bloch wave which is associated with only one dynamically coupled set. Further it should be noted that the same dynamically coupled set is defined regardless of which reciprocal lattice vector in the matrix,  $\vec{g}_j$ , in that set is chosen. Thus for example,  $\vec{g}_j = \vec{g}_1$  or  $\vec{g}_j = \vec{g}_3$  in Fig. 6.3 define the same dynamically coupled set of reflections.

### 6.2.3 DYNAMICAL EQUATIONS FOR THE TWIN

The usual method for deriving the dynamical equations is to substitute the expression for the Bloch wave into the Schrodinger wave equation. The dynamical equations are then obtained by equating the coefficients of each different exponential term to zero. When this procedure is adopted by



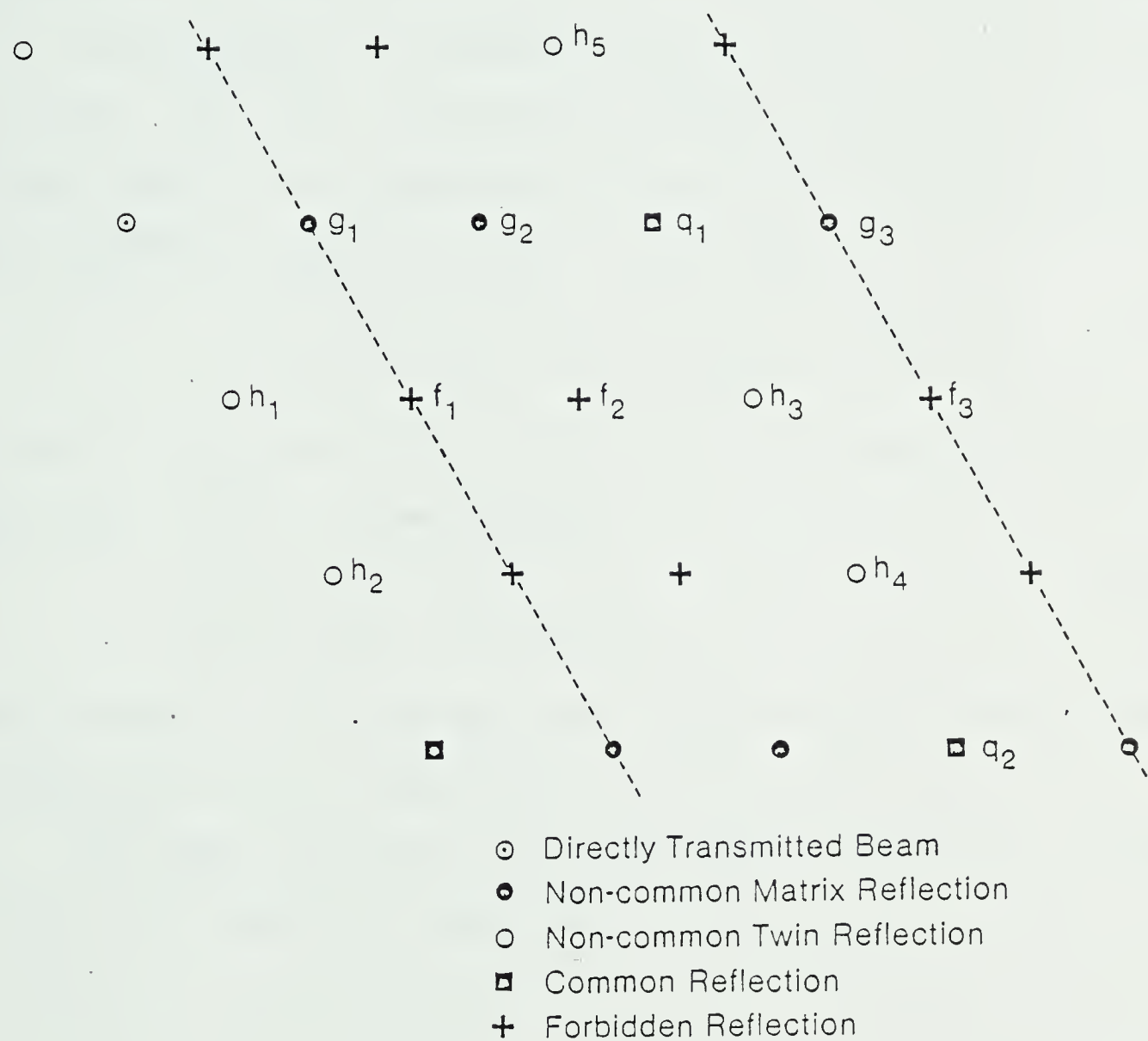


Figure 6.3 Schematic diagram showing the diffraction pattern obtained from a twinned crystal such as the one shown in Fig. 6.2. The dotted lines indicates those reflections which are in the coupled set.





substituting 6.2 into the Schrodinger wave equation a number of exponential terms involving different  $\vec{q}_m$  and  $\vec{h}_n$ , but whose argument are in fact equal, are obtained. This arises because there are, in general, a number of Bloch waves components in the direction of a particular diffracted beam,  $\vec{r}_k$ , corresponding to different combinations of coincidence lattice and twin reciprocal lattice vectors,  $\vec{q}_m + \vec{h}_n$ . As a result when 6.2 is substituted into the Schrodinger equation the dynamical equations take on the form:

$$[K^2 - (\vec{k}^{(i)} + \vec{r}_k)^2] C_{r_k}^{(i)} + \sum_{j \neq 0} U_{h_j} C_{r_k - h_j}^{(i)} = 0 \quad (6.4)$$

where  $\vec{r}_k$  is a particular reflection in a dynamically coupled set and  $C_{r_k}^{(i)}$  is defined by:

$$C_{r_k}^{(i)} = \sum_{m'} \sum_{n'} C_{\vec{g}_j + \vec{q}_{m'} + \vec{h}_{n'}}^{(i)} \quad (6.5)$$

The primes in 6.5 indicate that  $m$  and  $n$  take on only those values for which  $\vec{g}_j + \vec{q}_m + \vec{h}_n = \vec{r}_k$ .

The usual approach can now be used to cast 6.4 in the form of an eigenvalue equation:

$$\underline{A} \underline{C}^{(i)} = \gamma \underline{C}^{(i)} \quad (6.6)$$

where  $\underline{C}^{(i)}$  is a column vector whose elements are  $C_{r_k}^{(i)}$ ,  $\gamma^{(i)} = k_z^{(i)} - K_z$ ,  $z$  is the direction perpendicular to the upper surface in Fig. 6.2,  $\underline{A}$  is a square matrix whose diagonal elements  $A_{jj} = S_{r_j}$ ,  $S_{r_j}$  is the deviation parameter for the reflection  $r_j$  and  $r_j$  is the  $j$ -th reflection in the dynamically coupled set defined by a



matrix reciprocal lattice vector,  $\vec{g}_j$ . The off-diagonal elements of  $\underline{A}$  are given by  $A_{jk} = U_{\vec{r}_j - \vec{r}_k} / 2K$ , where it should be noted that  $\vec{r}_j - \vec{r}_k$  is a reciprocal lattice vector in the twin.

#### 6.2.4 DIFFRACTED BEAM AMPLITUDE

An expression for the diffracted beam amplitude can be obtained by writing down the total wave function for all electrons in the dynamically coupled set defined by a matrix reciprocal lattice vector,  $\vec{g}_j$ , as follows:

$$\Psi = \sum_i X^{(i)} b^{(i)} = \sum_i \sum_m \sum_n X^{(i)} C_{\vec{g}_j + \vec{q}_m + \vec{h}_n}^{(i)} \exp[2\pi i (\vec{k}^{(i)} + \vec{g}_j + \vec{q}_m + \vec{h}_n) \cdot \vec{r}] \quad (6.7)$$

where  $X^{(i)}$  is the excitation coefficient of Bloch wave  $b^{(i)}$ . The diffracted beam amplitude for a reflection  $\vec{r}_j$  can be obtained by adding all the terms in 6.7 which involve wave vectors in the direction of this diffracted beam. This gives:

$$\phi_{\vec{r}_j} = \sum_i X^{(i)} C_{\vec{r}_j}^{(i)} \exp[2\pi i \gamma^{(i)} z] \quad (6.8)$$

where the phase factor  $\exp[2\pi i (\vec{K} + \vec{r}_j) \cdot \vec{r}]$  which appears outside the summation has been neglected since it does not affect diffracted beam intensity. In order to obtain an expression for the excitation coefficients,  $X^{(i)}$  a procedure



similar to the one adopted in chapter 2 can be used. This gives

$$\underline{\phi} = \underline{C} \{ \exp(2\pi i \gamma^{(i)} z) \} \underline{X} \quad (6.9)$$

where  $\underline{\phi}$  is a column vector whose elements are  $\phi_{r_j}$ ,  $\underline{X}$  is a column vector whose elements are  $X^{(i)}$ ,  $\{ \exp(2\pi i \gamma^{(i)} z) \}$  is a diagonal matrix whose elements are  $\exp(2\pi i \gamma^{(i)} z)$  and  $\underline{C}$  is square matrix whose columns are  $\underline{C}^{(i)}_{r_j}$ . Premultiplying 6.9 by  $\underline{C}^{-1}$ , then by  $\{ \exp(2\pi i \gamma^{(i)} z) \}^{-1}$  and evaluating at  $z=t_m$  (see Fig. 6.2) gives:

$$\underline{X} = \{ \exp(-2\pi i \gamma^{(i)} t_m) \} \underline{C}^{-1} \underline{\phi}(t_m) \quad (6.10)$$

or

$$X^{(i)} = \exp(-2\pi i \gamma^{(i)} t_m) \sum_{\ell} C^{(i)}_{g_{\ell}, r_j} \phi_{g_{\ell}}(t_m) \quad (6.11)$$

and

$$\phi_{r_j}^{\rightarrow}(t) = \sum_i \sum_{\ell} \phi_{g_{\ell}}(t_m) C^{(i)}_{g_{\ell}, r_j} \exp(2\pi i \gamma^{(i)} t_t) \quad (6.12)$$

where the prime in 6.11 and 6.12 indicates that the summation is over all  $g_j$  in a particular dynamically coupled set and  $t$  is the total thickness of the twinned crystal in Fig. 6.2. In order to take a possible translation of the twin with respect to the matrix into account the lattice potential in the twin,  $V(\vec{r})$  can be written as  $V(\vec{r}-\vec{T})$  where  $\vec{T}$  is the body translation vector. As a result  $U_{h_j}$  in 6.4 becomes



$$U_{h_j} \exp(-2\pi i \vec{T} \cdot \vec{r}) \quad (6.13)$$

and  $C_{\vec{r}_K - \vec{h}_j}$  becomes

$$C_{\vec{r}_K - \vec{h}_j} \exp(2\pi i \vec{h}_j \cdot \vec{T}) \quad (6.14)$$

When this is taken into account in 6.10, 6.12 becomes:

$$\phi_{\vec{r}_j}^{\vec{T}}(t) = \sum_i \sum_{\ell} \phi_{g_{\ell}}(t_m) C_{g_{\ell}}^{(i)} C_{\vec{r}_j}^{(i)} \exp(2\pi i \gamma^{(i)} t_t) \exp(2\pi i \vec{g}_{\ell} \cdot \vec{T}) \quad (6.15)$$

where the phase factor  $\exp(-2\pi i \vec{r}_j \cdot \vec{T})$ , which appears outside the double sum, has been neglected since it does not affect diffracted beam intensity.

### 6.3 COMPARISON OF BLOCH WAVE APPROACH WITH METHOD OF GRATIAS AND PORTIER

The approach of Gratias and Portier (1980), as noted in the introduction, is based on the use of the Darwin equations. The basis for this formulation of the dynamical theory is the incorporation of a dynamical matrix in a set of differential equations (see Howie et. al. 1961, Gevers 1963.). Except for a factor of two, the elements of this dynamical matrix are of precisely the same form as the elements of the A matrix in the eigenvalue formulation of the dynamical theory (see section 6.2.3 in this chapter ). The approach adopted by Gratias and Portier in deriving the form of this matrix for the twin crystal in Fig. 6.2 was based on the fact that any reflection in the twin,  $\vec{r}_k$ , can





be written as:

$$\vec{r}_K = \vec{g}_j + \vec{h}_n \quad (6.16)$$

where, as in section 6.2 of this chapter,  $\vec{g}_j$  is any reciprocal lattice vector in the matrix and  $\vec{h}_n$  is any reciprocal lattice vector in the twin. Since the off-diagonal elements of the dynamical matrix in the Darwin approach are the same, except for a factor of two, as those in the A matrix of the eigenvalue approach they can be written as

$$U_{\vec{r}_i - \vec{r}_j} / K = \left( \frac{2m e}{h^2} \right) V_{\vec{r}_i - \vec{r}_j} / K \quad (6.17)$$

where the requirement that  $V_{\vec{r}_i - \vec{r}_j}$  must be a Fourier coefficient of the lattice potential in the twin must be met. However, if  $\vec{r}_i, \vec{r}_j$  are defined as in 6.16 above, then  $\vec{r}_i - \vec{r}_j$  is not necessarily a reciprocal lattice vector in the twin. Gratias and Portier overcame this difficulty by defining the off-diagonal elements of their dynamical matrix as

$$[U_{\vec{r}_i - \vec{r}_j} / K] \delta[(\vec{r}_i - \vec{r}_j), \vec{h}_n] \quad (6.18)$$

where

$$\delta[(\vec{r}_i - \vec{r}_j), \vec{h}_n] = 0 \quad \text{if} \quad (\vec{r}_i - \vec{r}_j) \neq \vec{h}_n \quad (6.19)$$

and



$$\delta[(\vec{r}_i - \vec{r}_j), \vec{h}_n] = 1 \quad \text{if} \quad (\vec{r}_i - \vec{r}_j) = \vec{h}_n \quad (6.20)$$

Using this approach, Gratias and Portier were able to write a single dynamical matrix for the twin as opposed to one dynamical matrix for each coupled set in the Bloch wave approach (see section 6.2 in this chapter). However, their dynamical matrix has zeroes embedded in it for those off-diagonal elements for which  $\delta[(\vec{r}_i - \vec{r}_j), \vec{h}_n]$  equals zero. An important point noted by Gratias and Portier is that if the correct order is chosen for the reflections taken into account in the twin, then their dynamical matrix can be cast in block or sub-matrix form. In order to illustrate this point and to see the relationship between the method of Gratias and Portier and the Bloch wave approach described in section 6.2, a specific example will be considered. Suppose for example, that the diffraction pattern obtained from the twinned crystal is as shown in Fig. 6.3 and that the following eight reflections are to be taken into account  $\vec{r}_0=0, \vec{r}_1=\vec{h}_1, \vec{r}_2=\vec{q}_1, \vec{r}_3=\vec{h}_3, \vec{r}_4=\vec{g}_1, \vec{r}_5=\vec{f}_1, \vec{r}_6=\vec{g}_3$  and  $\vec{r}_7=\vec{f}_3$ . If the reflections are taken in the order given above, then the dynamical matrix in the method of Gratias and Portier becomes the matrix shown in Fig. 6.4. It can be seen that this dynamical matrix is indeed in block form and as noted by Gratias and Portier each sub-matrix is associated with a particular dynamically coupled set. An important point to note is that the choice of the order of the reflections used



$$\begin{bmatrix}
 0 & U_{-h_1}/K & U_{-q_1}/K & U_{-h_3}/K & 0 & 0 & 0 & 0 \\
 U_{h_1}/K & 2S_{h_1} & U_{-h_5}/K & U_{-q_1}/K & 0 & 0 & 0 & 0 \\
 U_{q_1}/K & U_{h_5}/K & 2S_{q_1} & U_{-h_1}/K & 0 & 0 & 0 & 0 \\
 U_{h_3}/K & U_{q_1}/K & U_{h_1}/K & 2S_{h_3} & 0 & 0 & 0 & 0 \\
 \hline
 0 & 0 & 0 & 0 & 2S_{g_1} & U_{-h_1}/K & U_{-q_1}/K & U_{-h_3}/K \\
 0 & 0 & 0 & 0 & U_{h_1}/K & 2S_{f_1} & U_{-h_5}/K & U_{-q_1}/K \\
 0 & 0 & 0 & 0 & U_{q_1}/K & U_{h_5}/K & 2S_{g_3} & U_{-h_1}/K \\
 0 & 0 & 0 & 0 & U_{h_3}/K & U_{q_1}/K & U_{h_1}/K & 2S_{f_3}
 \end{bmatrix}$$

Figure 6.4 Gratiias and Portier dynamical matrix showing the sub-matrices associated with the dynamically coupled set of reflections.



in defining the elements of the dynamical matrix is important if the final result is to appear in this form. Thus, in the example above, the first four reflections must be chosen from one dynamically coupled set and the second four from another in order that the matrix in Fig. 6.4 appears in block form.

A comparison of the method of Gratias and Portier with the Bloch wave approach described in section 6.2 of this chapter can now be made. As noted in section 6.2.2, a given choice of  $\vec{g}_j$  in a Bloch wave in the twin (see 6.2) defines a particular dynamically coupled set. The set of dynamical equations 6.6 obtained by inserting this Bloch wave into the Schrodinger equation must, therefore, also be associated with that particular set. Thus, for example, the dynamically coupled set defined by the choice  $\vec{g}_j = \vec{g}_1$  is indicated by the net of dotted lines in Fig. 6.3 and the four reflections  $\vec{g}_1$ ,  $\vec{f}_1$ ,  $\vec{g}_3$  and  $\vec{f}_3$  reside in this set. From 6.1 these reflections can be written as:

$$\begin{aligned} \vec{r}_4 &= \vec{g}_1 + (0 + 0) & \vec{r}_5 &= \vec{g}_1 + (0 + \vec{h}_1) \\ \vec{r}_6 &= \vec{g}_1 + (\vec{q}_1 + 0) & \vec{r}_7 &= \vec{g}_1 + (\vec{q}_1 + \vec{h}_1) \end{aligned} \quad (6.21)$$

Using these reflections to define the elements of the A matrix in 6.6 gives a matrix which is identical except for a factor of two, to the lower sub-matrix in Fig. 6.4. It can be shown, as a result of this equivalence, that the method of Gratias and Portier and the Bloch wave approach presented





in this chapter give identical values for diffracted beam amplitude. This can most easily be seen by noting that, in order to calculate the intensity of a particular diffracted beam Gratias and Portier need only to diagonalize the sub-matrix in which this beam is taken into account. Precisely the same matrix, except for a factor of two are, therefore, obtained from the two methods. When this factor of two is taken into account in the arguments of the complex exponentials which appear in expressions for diffracted beam amplitude, it can be shown that the two methods do, in fact, give identical results.

#### 6.4 COMPARISON OF BLOCH WAVE APPROACH WITH METHOD OF SUTTON AND POND

The method of Sutton and Pond (1978), is based on the use of the expression for diffracted beam amplitude given by Sheinin and Corbett (1976), which was developed for the case in which common reflections are not taken into account. This expression can be written as:

$$\phi_{\vec{r}_K}^+(t) = \phi_{\vec{g}_\ell}^+(t_m) \sum_i C_{\vec{g}_\ell}^{(i)} C_{\vec{r}_K}^{(i)} \exp(2\pi i \gamma^{(i)} t_t) \quad (6.22)$$

where  $\phi_{\vec{r}_K}^+$ ,  $\phi_{\vec{g}_\ell}^+$  are the diffracted beam amplitudes of the reflections  $\vec{r}_K$  and  $\vec{g}_\ell$  and  $\gamma^{(i)}$ ,  $C_{\vec{r}_K}^{(i)}$  are eigenvalues and elements of eigenvectors obtained by diagonalizing an A matrix whose elements are



$$A_{ii} = S_{r_i}$$

$$A_{ij} = U_{\vec{r}_i - \vec{r}_j} / 2K = U_{\vec{h}_i - \vec{h}_j} / 2K \quad (6.23)$$

In 6.23, the reflections used to define the elements of the A matrix are given by

$$\vec{r}_n = \vec{g}_{\ell'} + \vec{h}_n \quad (n = 1; N_t) \quad (6.24)$$

where  $N_t$  is the number of reflections taken into account in the twin and the reflection  $\vec{r}_k$  in 6.22 is given by:

$$\vec{r}_K = \vec{g}_{\ell'} + \vec{h}_{n'} \quad (6.25)$$

where  $n'$  is a particular value of  $n$ . In order to take common reflections into account Sutton and Pond noted that there will be other possible combinations of matrix and twin reciprocal lattice vectors (i. e. other possible values of  $\ell'$  and  $n'$  in 6.25), which give the same  $\vec{r}_k$ . They argued that each of these possible combinations will result in a contribution to the diffracted beam amplitude similar to the one given in 6.22 and that the total diffracted beam amplitude can, therefore, be obtained by superimposing each of these contributions to give



$$\phi_{r_K}^+(t) = \sum_i \sum_{\ell'} \phi_{g_{\ell'}}(t) C_{g_{\ell'}}^{(i)} C_{r_K}^{(i)} \exp[2\pi i \gamma^{(i)} t_t] \quad (6.26)$$

It can be seen that this expression is, in fact, identical in form to 6.12 in this chapter and it is clear, therefore, that the method of Sutton and Pond will give the same values for diffracted beam amplitude as the method presented in this chapter if the eigenvalues  $\gamma^{(i)}$  and eigenvectors  $\underline{C}^{(i)}$ , used in evaluating 6.12 and 6.26 are the same. The answer to this question is not immediately obvious. The reason for this lies in the fact that the eigenvalues and eigenvectors used to evaluate 6.12 were obtained by diagonalizing a single  $\underline{A}$  matrix whose elements were defined by the reflections in a particular dynamically coupled set. On the other hand, the method of Sutton and Pond requires a number of  $\underline{A}$  matrices to be diagonalized, one corresponding to each value of  $l'$  in 6.26. It was assumed by Sutton and Pond that each of these  $\underline{A}$  matrices would be different giving different eigenvalues and eigenvectors. If this assumption is correct, then the method of Sutton and Pond and the method presented in this chapter would indeed, give different results. It can be shown, however, that this assumption is, in fact, not correct, as can be seen from the following argument. Consider two sets of values of  $l'$ ,  $n'$  which satisfy 6.25, namely  $p$ ,  $q$  and  $p'$ ,  $q'$ . From 6.25



$$\vec{g}_p + \vec{h}_q = \vec{g}_{p'} + \vec{h}_{q'} \quad (6.27)$$

and

$$\vec{g}_p - \vec{g}_{p'} = \vec{h}_{q'} - \vec{h}_q \quad (6.28)$$

6.28 can only be satisfied if  $\vec{g}_p - \vec{g}_{p'}$  is a reciprocal lattice vector of the coincidence lattice so that

$$\vec{g}_p = \vec{g}_{p'} + \vec{q}_m \quad (6.29)$$

The two sets of reflections which define the  $\underline{A}$  matrices corresponding to  $l'=p, l'=p'$  can now be obtained from 6.25 and 6.29 and are given by:

$$(\vec{r}_n)_{p'} = \vec{g}_{p'} + \vec{h}_n \quad (n = 1, N_t) \quad (6.30)$$

and

$$(\vec{r}_n)_p = \vec{g}_{p'} + (\vec{q}_m + \vec{h}_n) \quad (n = 1, N_t) \quad (6.31)$$

In comparing these two sets of reflections, it is important to emphasize that  $\vec{q}_m$  is a reciprocal lattice vector of the coincidence lattice and so must also be a member of the set of reciprocal lattice vectors of the twin  $\vec{h}_n$ . The sets of reciprocal lattice vectors  $\vec{h}_n$  and  $(\vec{q}_m + \vec{h}_n)$  in 6.30 and 6.31 are therefore, identical, if  $n$  is allowed to range over all possible values. As a result the two sets of reflections given by 6.30 and 6.31 are identical and, therefore, the  $\underline{A}$  matrices which these sets of reflections define must also be





the same. These arguments can easily be extended to all values of  $l'$  in 6.26 leading to the conclusion that, in order to evaluate this expression, only a single A matrix has to be diagonalized. In addition, the discussion in paragraph 6.2 indicates that the sets of reflections defining this A matrix, and given by relationships such as 6.30 or 6.31, are all members of the same dynamically coupled set. It can finally be concluded, therefore, that 6.12 and 6.26 will in fact give identical results and that the method of Sutton and Pond is completely equivalent to the method presented in this chapter.

## 6.5 DISCUSSION AND CONCLUSIONS

The work presented in this chapter has shown that the methods for taking common reflections into account in calculations of diffracted beam intensity at the bottom surface of a twinned crystal, developed independently by Sutton and Pond (1978), Gratias and Portier (1980) and in this chapter are completely equivalent. It should be emphasized that the analysis in paragraph 6.2, 6.3 and 6.4 which has led to this conclusion is based on an examination of general forms of the theory involving an infinite number of beams in the twin. It is, of course, evident that one of the central problems which must be addressed before any practical calculation of image contrast can be undertaken is a determination of which reflections in the twin should be taken into account. The procedure involved in making this



determination is more complex than the usual N-beam approximation made in the case of a single crystal and problems can arise if an incorrect approach is adopted. In order to illustrate this point, one approach which might be adopted is to first choose matrix reflections  $\vec{g}_p$  and twin reflections  $\vec{h}_i$  which are considered important and should be taken into account. Additional reflections which should be taken into account in the twin would then be of the form  $\vec{g}_p + \vec{h}_i$ . If this procedure is adopted then the A matrices corresponding to each value of  $l'$  in 6.26 will indeed be different as suggested by Sutton and Pond, and the critical comments about their method which were referred to in the introduction of this chapter, can be justified. This procedure is, however, incorrect for the following reason. It has been assumed that if  $\vec{g}_p$  and  $\vec{h}_i$  are strongly excited reflections in the matrix and twin respectively, then  $\vec{g}_p + \vec{h}_i$  is also strongly excited reflection. This, of course, needn't necessarily be so since both  $\vec{g}_p$  and  $\vec{h}_i$  can be close to the Bragg condition while at the same time  $\vec{g}_p + \vec{h}_i$  may be far from the Bragg condition. The corollary of this also follows, namely that  $\vec{g}_p + \vec{h}_i$  may be a strongly excited reflection in the twin even if  $\vec{h}_i$  is not. It is clear from these remarks that great caution should be taken in choosing the beams to be taken into account in the twin if problems of the kind referred to in the literature are to be avoided.



## CHAPTER VII

# EXPERIMENTAL EVIDENCE SHOWING THAT THE USE OF SYMMETRICAL LAUE DIFFRACTION CONDITIONS IN THE DYNAMICAL THEORY OF ELECTRON DIFFRACTION CAN GIVE SIGNIFICANT ERRORS IN DIFFRACTION CONTRAST CALCULATIONS

### 7.1 INTRODUCTION

Calculations of contrast in electron microscope images of crystals have, in the past, been based almost exclusively on the assumption that symmetrical Laue (SL) diffraction conditions (see chapter 3 for a detailed discussion), obtain. The basis for this approach has been the widely accepted view that the Bloch waves excited under non-symmetrical Laue (NSL) diffraction conditions are not significantly different from those in the SL case for the range of diffraction conditions normally encountered in electron microscope examination of crystals. This view is supported by the work of Whelan and Hirsch (1957) who showed, on the basis of the two-beam theory, that for angles up to about  $80^\circ$ , the inclination of a stacking fault does not have a significant effect on diffracted beam intensity. More recently Saldin et. al. (see Saldin et. al. 1978.) employing an approach based on the Darwin equation formulation of the dynamical theory, have concluded that over a range of angles of inclination of the incident surface up to about  $70^\circ$ , only small errors are involved in the use of SL diffraction conditions. Sheinin and Jap (1979), however, have shown that





the errors involved in calculations of image contrast based on the assumption of SL diffraction conditions increase significantly with increasing deviation from the Bragg condition of the lowest order reflection in the systematic set excited. Thus, for example, they found that for weak beam diffraction conditions and an angle of inclination of the crystal surface of only  $30^\circ$  significant differences in SL and NSL dislocation profiles were obtained.

On the basis of theoretical considerations, therefore, there seems to be a strong indication that the widespread use of SL diffraction conditions in calculations of the contrast obtained in electron microscope images of crystals can give rise to serious errors. As yet, however, there has been no experimental evidence presented in the literature which supports this view. The main purpose of this chapter is to present such an evidence.

## 7.2 THEORETICAL BACKGROUND

### 7.2.1 DYNAMICAL THEORY FOR THE NSL CASE

A form of the dynamical theory of electron diffraction applicable to the NSL case has been reported in the literature by Spencer and Humphreys (1971) and Sheinin and Jap (1979). This form of the dynamical theory can give rise to significant errors under certain diffraction conditions since the high energy approximation is employed in its derivation (see Sheinin et. al. 1979.). In a recent paper





Kim and Sheinin (1982) have presented an exact form of the theory which overcomes this difficulty. Their form of the theory can be expressed as an eigenvalue equation:

$$\underline{A}_e \underline{C}_e^{(i)} = \gamma^{(i)} \underline{C}_e^{(i)} \quad (7.1)$$

where

$$\vec{\gamma}^{(i)} = \gamma^{(i)} \vec{n} = \vec{k}^{(i)} - \vec{K} \quad (7.2)$$

and

$$\underline{A}_e = \begin{bmatrix} -\underline{H} & \underline{I} \\ \underline{D} & \underline{O} \end{bmatrix} \quad \underline{C}_e^{(i)} = \begin{pmatrix} \underline{C}^{(i)} \\ \underline{X}^{(i)} \end{pmatrix} \quad (7.3)$$

and also

$$\underline{X}^{(i)} = (\underline{H} + \gamma^{(i)} \underline{I}) \underline{C}^{(i)} \quad (7.4)$$

$\underline{I}$  is the unit matrix,  $\underline{O}$  is the null matrix and the elements of the  $\underline{D}$  and  $\underline{H}$  matrices are given by:

$$D_{gg} = Q_g = -g^2 - 2\vec{K} \cdot \vec{g} \quad D_{gh} = U_{g-h} \quad (7.5)$$

and

$$H_{gg} = P_g = 2\vec{n} \cdot (\vec{K} + \vec{g}) \quad H_{gh} = 0 \quad (7.6)$$

It should be noted that  $\underline{H}$ ,  $\underline{I}$ ,  $\underline{D}$  and  $\underline{O}$  are  $N \times N$  matrices and  $\underline{A}_e$  is a  $2N \times 2N$  matrix where  $N$  is the number of beams taken into account. In the above expressions  $U_{g-h}$ ,  $\vec{K}$  and  $\vec{k}^{(i)}$  have the same meaning as those defined in chapter 2.  $\underline{C}^{(i)}$  is a column



vector containing the Bloch wave Fourier coefficients  $C_g^{(i)}$  and  $\vec{n}$  a unit vector normal to the entrance surface. (see Fig. 7.1 and 7.2). It should be noted that at the symmetry orientation:

$$Q_g = -g^2 \quad (7.9)$$

and

$$P_g = 2(K \cos \theta - g \sin \theta) \quad (7.10)$$

### 7.3 DIFFRACTED BEAM INTENSITY AT THE BOTTOM SURFACE OF A WEDGE CRYSTAL.

The diffracted beam amplitude  $\Phi_g$  at the bottom surface of a wedge crystal can be obtained from the total electron wave function in the crystal by summing all terms involving wave vectors in the direction of the diffracted beam to give:

$$\phi_g = \sum_i C_i^{-1} C_g^{(i)} \exp[2\pi i \vec{\gamma}^{(i)} \cdot \vec{R}_b] \quad (7.11)$$

where  $C_i^{-1}$  is the  $i$ -th element in the first column of the inverse of the matrix  $\underline{C}$  and the columns of  $\underline{C}$  are the columns vectors  $\underline{C}^{(i)}$ .  $\vec{R}_b$  is defined in Fig. 7.1 and the phase factor  $[2\pi i(K+g) \cdot r]$  has been neglected in 7.11 since it does not affect diffracted beam intensity. From Fig. 7.1 and 7.2 it can be seen that



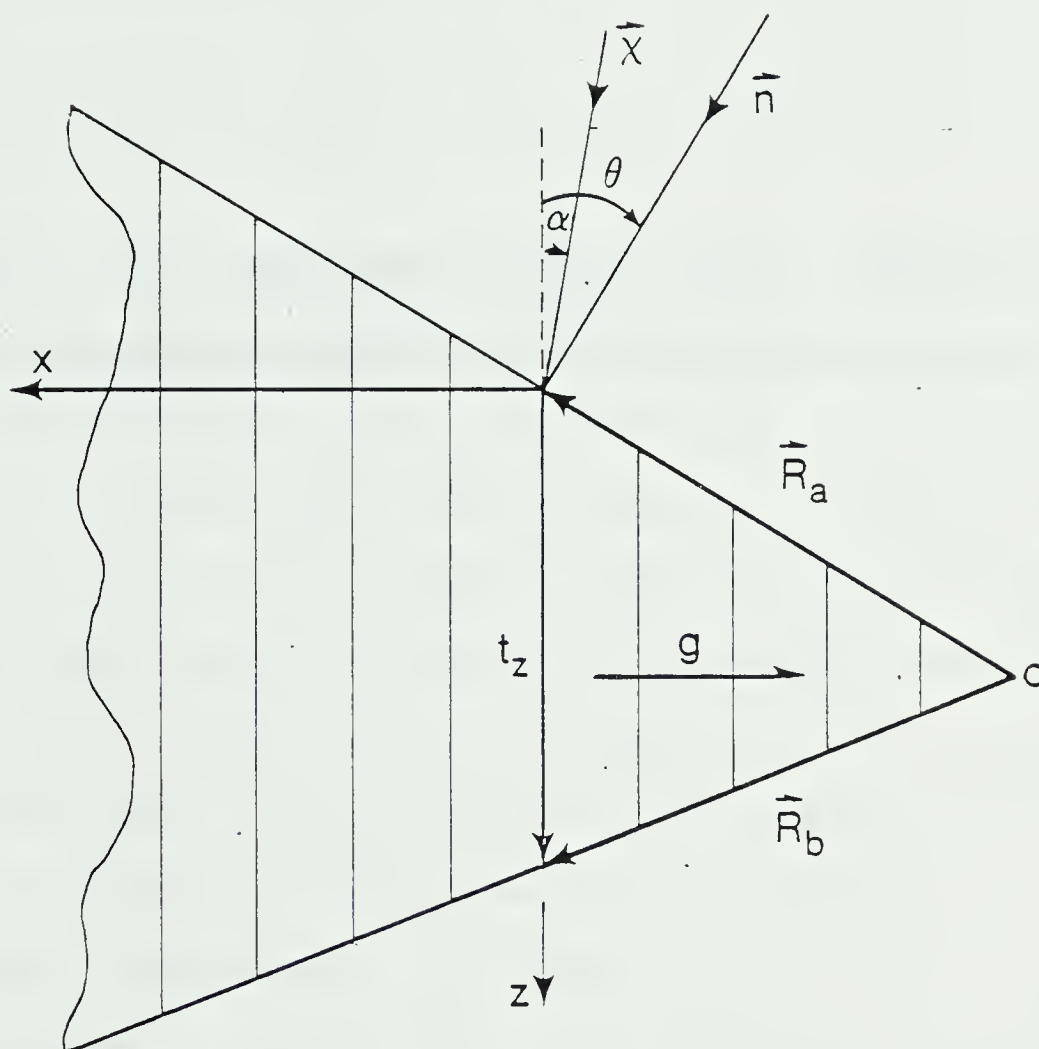


Figure 7.1 Schematic drawing of a wedge crystal.  $\vec{\chi}$  is the incident wave vector,  $\vec{n}$  is the surface normal and  $\theta$  is the angle between  $\vec{n}$  and the Brillouin zone boundary.



$$\vec{\gamma}^{(i)} \cdot \vec{R}_b = \gamma^{(i)} \vec{n} \cdot (\vec{R}_a + \vec{t}_z) = \gamma_z^{(i)} t_z \quad (7.12)$$

Substituting 7.12 into 7.11 gives the following expression for diffracted beam intensity:

$$I_g = |\phi_g|^2 = \left| \sum_i C_i^{-1} C_g^{(i)} \exp[2\pi i \gamma_z^{(i)} t_z] \right|^2 \quad (7.13)$$

#### 7.4 ANALYSIS OF IMPORTANT BLOCH WAVES CONTRIBUTING TO DIFFRACTED BEAM INTENSITY AT THE SYMMETRY POSITION.

In order to carry out an experiment which would provide a test of the theoretical differences in image contrast obtained in the SL and NSL cases, suitable diffraction conditions must first be chosen. To this end an analysis of the important Bloch waves contributing to diffracted beam intensity has been carried out for both cases and for a variety of diffraction conditions (the importance of a Bloch wave has been determined from the value of  $C^{-1}_i C^{(i)}_g$  in 7.13). Systematic reflections only were taken into account in the calculations and the crystal was taken to be oriented at the symmetry position. In the SL case, assuming that there are only 3 important Bloch waves, the following relations hold:  $C^{-1}_i = C^{(i)}_0$  ( $i=1, 2$  and  $3$ )  $C^{(i)}_g = C^{(i)}_{-g}$  ( $i=1, 2$ ) and  $C^{(3)}_g = -C^{(3)}_{-g}$ . In addition  $C^{(3)}_0 = 0$  and therefore in this case 7.13 gives  $I_g = I_{-g}$ . On the other hand, in the NSL case at the symmetry position  $|C^{(i)}_g| \neq |C^{(i)}_{-g}|$  ( $i=1, 2$  and  $3$ ) and therefore  $I_g \neq I_{-g}$ . These considerations suggested





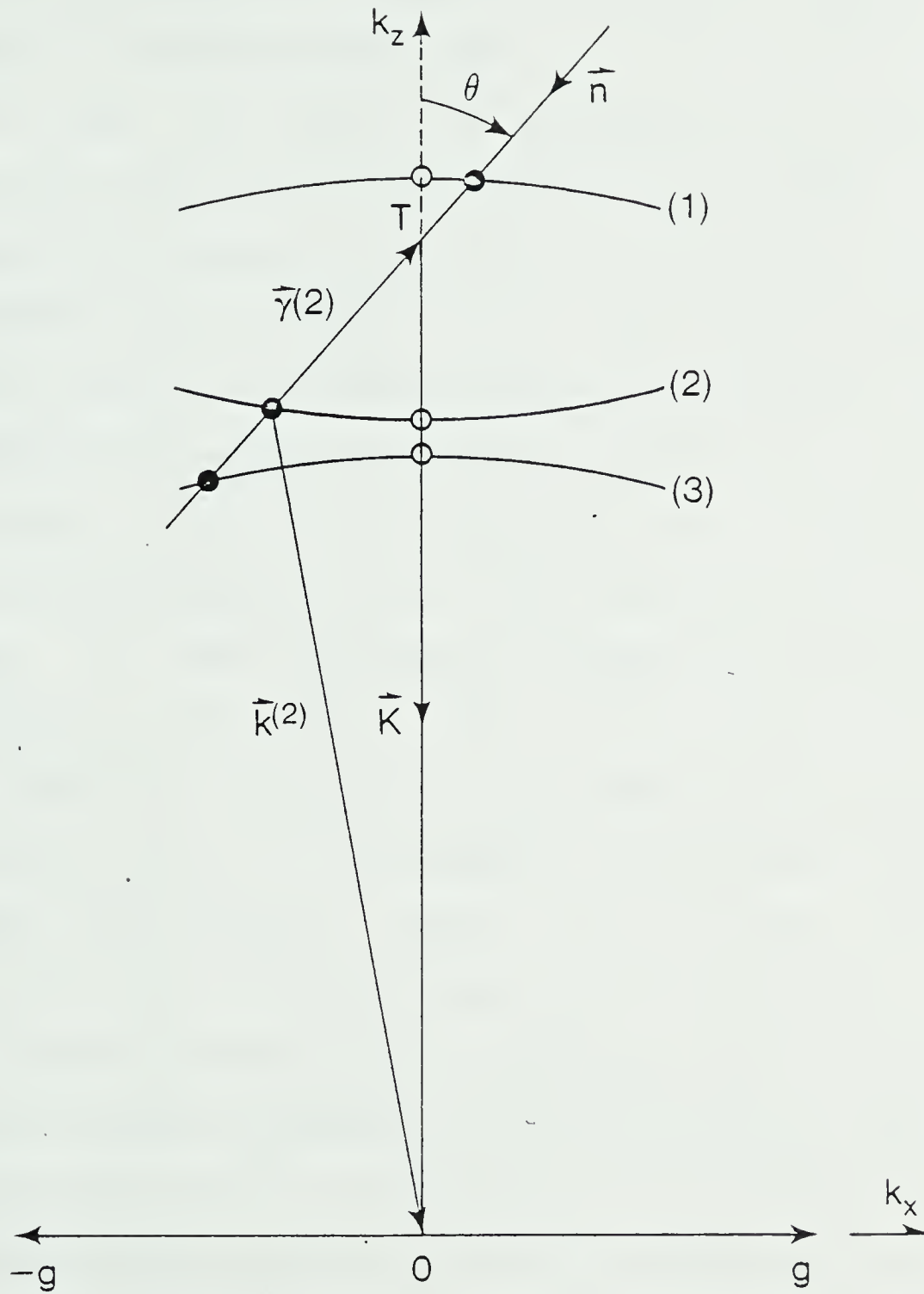


Figure 7.2 Schematic drawing of the dispersion surface in the three beam approximation. The wave points obtained in the SL and NSL cases are indicated by the open and solid circles respectively.



that a comparison of thickness fringes in the  $g$  and  $-g$  dark field images obtained at the symmetry position might provide a good illustration of the differences in image contrast obtained in the SL and NSL cases.

In order to choose an inclination of the incident surface for which significant differences between  $I_g$  and  $I_{-g}$  might be obtained, values of  $C^{-1}_i C^{(i)}_g$  and  $C^{-1}_i C^{(i)}_{-g}$  have been plotted as a function of  $\theta$ , the angle between the surface normal and the Brillouin zone boundary (see Figs. 7.1 and 7.2 for a definition of  $\theta$ ). Calculations have been carried out for the  $(0\ 2\ -2)$  systematic set in silicon where the reciprocal lattice vector  $\vec{g}$  was taken to be to the right in Fig. 7.4. The accelerating voltage in the calculations was taken to be 150KV. Both three beam (including reflections  $0$ ,  $g$  and  $-g$ ) and many-beam calculations (including up to 13 systematic reflections) have been performed and similar results were obtained. The results shown in Fig. 7.3, indicate that the contributions of Bloch wave 1 to the intensities  $I_g$  and  $I_{-g}$  are very nearly the same and virtually independent of  $\theta$ . At  $\theta=0$  (the SL case), the contributions of Bloch wave 2 to  $I_g$  and  $I_{-g}$  are also the same whereas the contributions of Bloch wave 3 to both diffracted beams is zero. Clearly therefore the SL case can be described in terms of only two important Bloch waves and thickness fringes should, as a result, be sinusoidal in character. As  $\theta$  increases there is no appreciable change in the contributions of Bloch waves 2 and 3 to  $I_{-g}$  and,



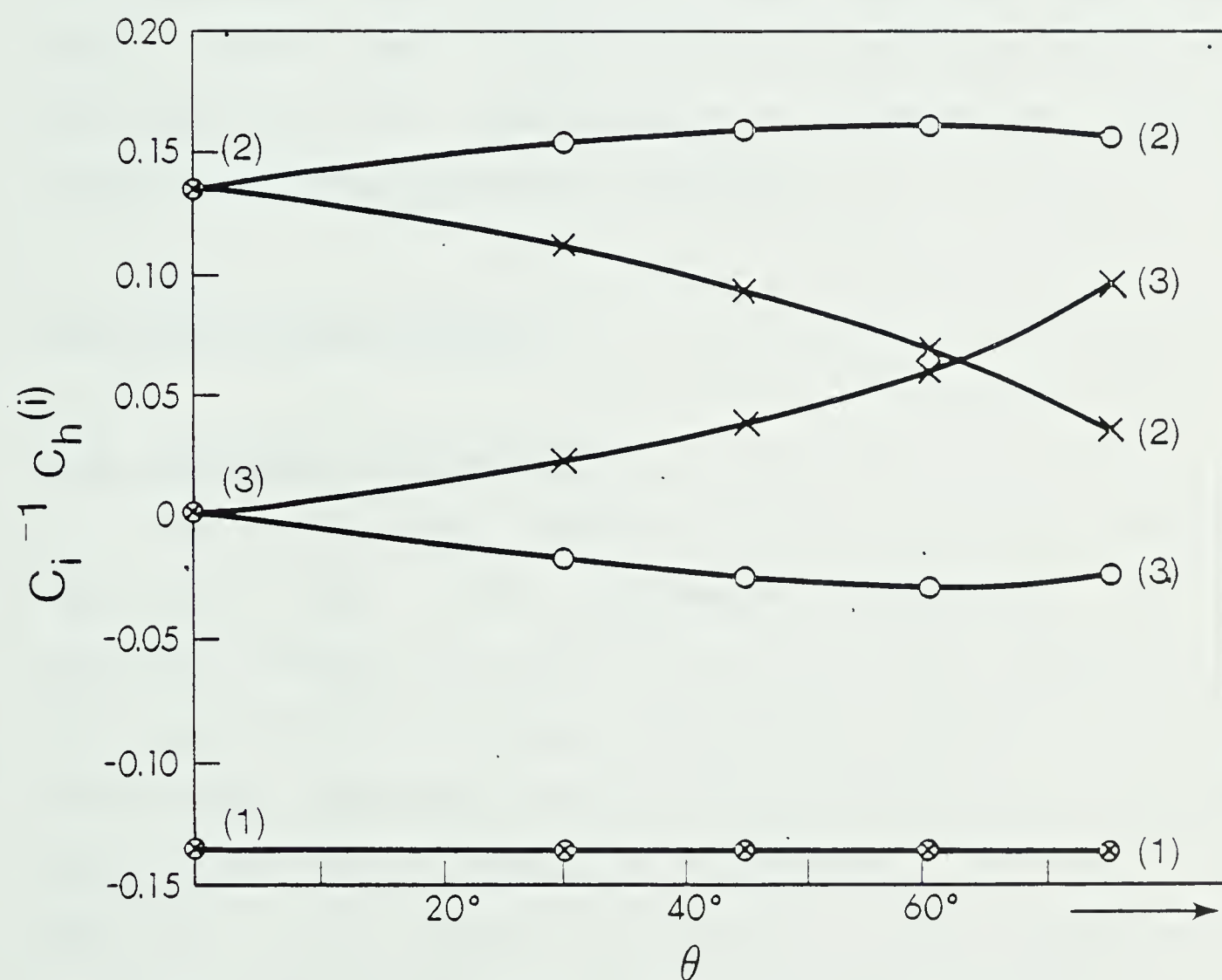


Figure 7.3 Excitation amplitudes  $C_i^{-1} C_h^{(i)}$  plotted as a function of  $\theta$  for silicon at the symmetry position of the systematic set. The circles correspond to  $h=-g$  and the crosses to  $h=g$ .



therefore, thickness fringes in the  $-g$  dark field image should be similar in both the SL and NSL cases. On the other hand thickness fringes in the  $g$  dark field image can be expected to be quite different in the two cases. This can be seen from the fact that the contribution of Bloch wave 2 to  $I_g$  decreases with increasing  $\theta$  while the opposite is true for Bloch wave 3. At  $\theta=60^\circ$ , these contributions become equal. There are, therefore, three important Bloch waves contributing to  $I_g$  under these circumstances and thickness fringes should be complex in character.

## 7.5 EXPERIMENTAL RESULTS

### 7.5.1 SPECIMEN REQUIREMENTS

The theoretical analysis in the previous section indicated that, when systematic reflections only are excited, thickness fringes in the SL case are identical in  $g$  and  $-g$  dark field images, provided the crystal is oriented at the exact symmetry position. This analysis also indicated that these fringes should be significantly different in the NSL case if  $g$  is chosen to be the  $(0\ 2\ -2)$  reflection in silicon, if  $\theta$ , the angle between the surface normal and the Brillouin zone boundary is about  $60^\circ$  and if the accelerating voltage is 150KV. In order to carry out an experiment which would determine if these differences between  $g$  and  $-g$  dark field images at the symmetry position are in fact obtained in the NSL case, suitable specimens must first be found.





Fortunately, certain types of silicon whiskers meet the requirements outlined above. Detailed studies carried out by Wagner et. al. (1964) have shown that these whiskers are of three main forms. The first is either a film or nodule like deposit attached to the walls of the reaction tube. The second form is a hexagonal needle growing in a  $(1\ 1\ 1)$  direction with well developed  $\{2\ 1\ 1\}$  lateral faces and the third form is a twinned ribbon growing in a  $[2\ 1\ 1]$  direction with  $\{1\ 1\ 1\}$  twinning planes parallel to the main faces. A cross section of a needle like whisker, such as was in fact used in this investigation, is shown in Fig. 7.4, from which it can be seen that  $\theta$  is  $60^\circ$  as required (the widths of these whiskers are typically of the order of several microns). In addition the  $(0\ 2\ -2)$  planes are parallel to the  $(-1\ 1\ 1)$  axis of the whisker, thus providing the systematic set of reflections required for the experiment. Also it should be noted that natural brittleness of silicon makes it an admirable test specimen since strains which might alter the form of the thickness fringes can easily be avoided.

#### 7.5.2 EXPERIMENTAL PROCEDURE

The experimental procedure involved initially orienting the whisker so that the  $(0\ 2\ -2)$  systematic set of reflections in a  $(2\ 1\ 1)$  diffraction pattern is strongly excited while the non-systematic reflections are only weakly excited. In order to record images at the exact symmetry



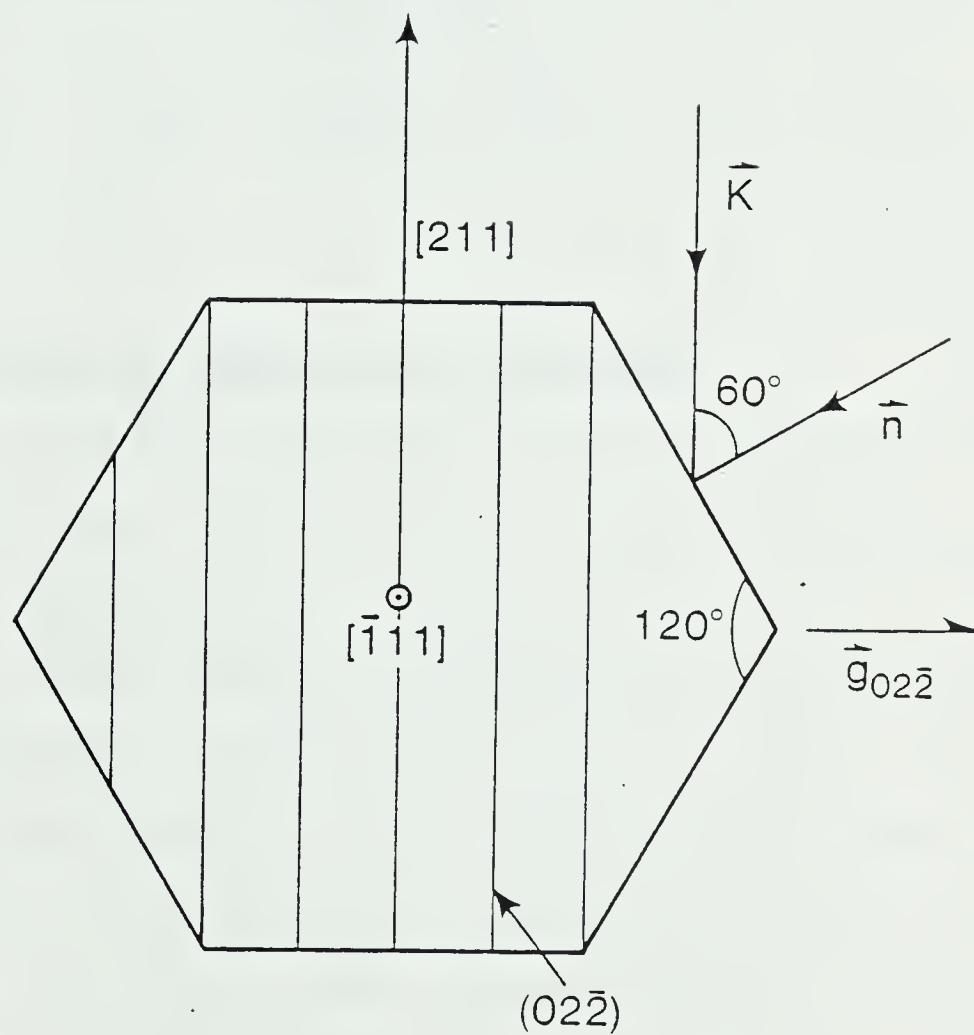


Figure 7.4 Schematic drawing showing a cross section of a silicon whisker. The Bragg reflecting planes are  $(0\ 2\ -2)$ . In this particular case the angle  $\theta$  between the surface normal  $\vec{n}$  and the Brillouin zone boundary is  $60^\circ$ .



position, the whisker was first oriented so that a higher order reflection, such as  $(0\ 6\ -6)$  was in the exact Bragg condition (as determined from the  $(0\ 6\ -6)$  Kikuchi line passing through the centre of the  $(0\ 6\ -6)$  spot). The specimen was then tilted through the required angle to orient the specimen at the exact symmetry position by using the high precision tilting stage mentioned in chapter 3.  $(0\ 2\ -2)$  and  $(0\ -2\ 2)$  dark field images were then recorded and densitometer traces showing the thickness fringes in each image were taken.

#### 7.6 COMPARISON OF THEORY WITH EXPERIMENT

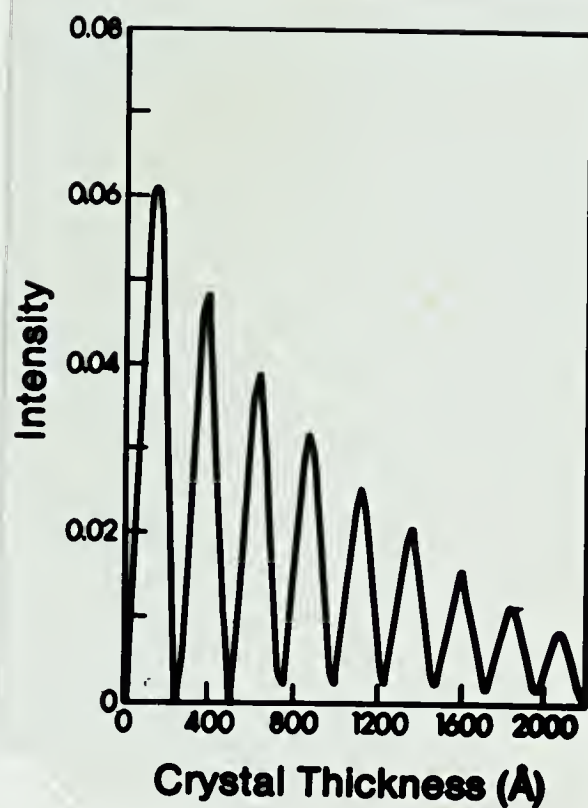
Figs. 7.5b and 7.6b show densitometer traces taken from  $g=(0\ 2\ -2)$  and  $-g=(0\ -2\ 2)$  dark field images using the procedure described in section 7.5. It is clear, in comparing these traces, that there are striking differences in the extinction contours obtained in these two images. In the  $-g$  image shown in Fig. 7.5b, it can be seen that the fringes are of high contrast and that 9 fringes can easily be seen. In the  $g$  image shown in Fig 7.6b, on the other hand, only 6 fringes can be seen with fringes in thicker crystal exhibiting contrast which is too weak to permit detection.

In order to compare these results with theory, calculations of intensity profiles for both the SL and NSL cases were carried out. The theoretical calculations were based on the theory outlined in section 7.2. In the





a



b

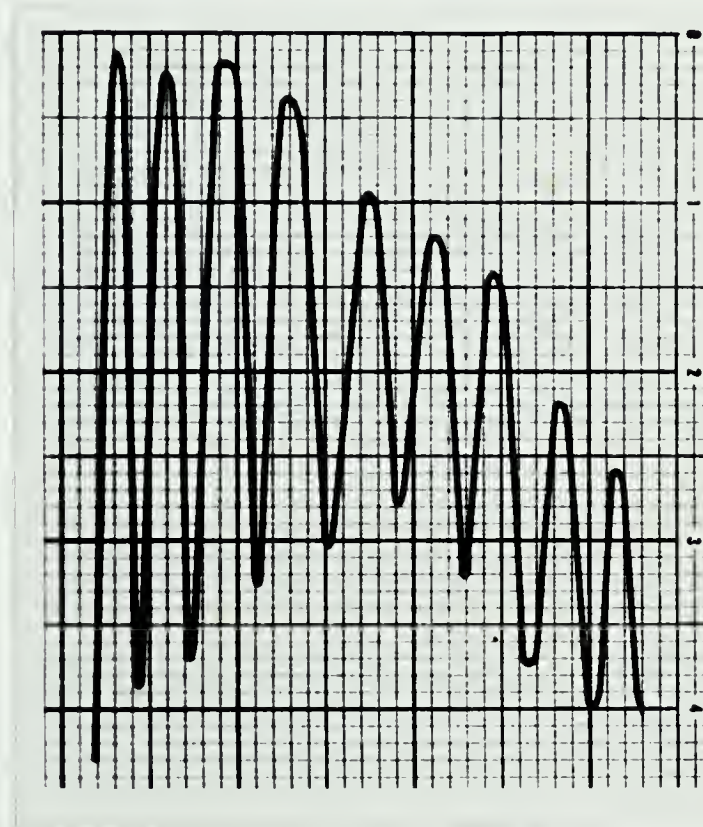


Figure 7.5 a) Show the theoretical profile obtained by using the  $-g=(0 \ -2 \ 2)$  reflection. Calculations were carried out for the NSL case . b) Show the experimental densitometer trace corresponding to a).





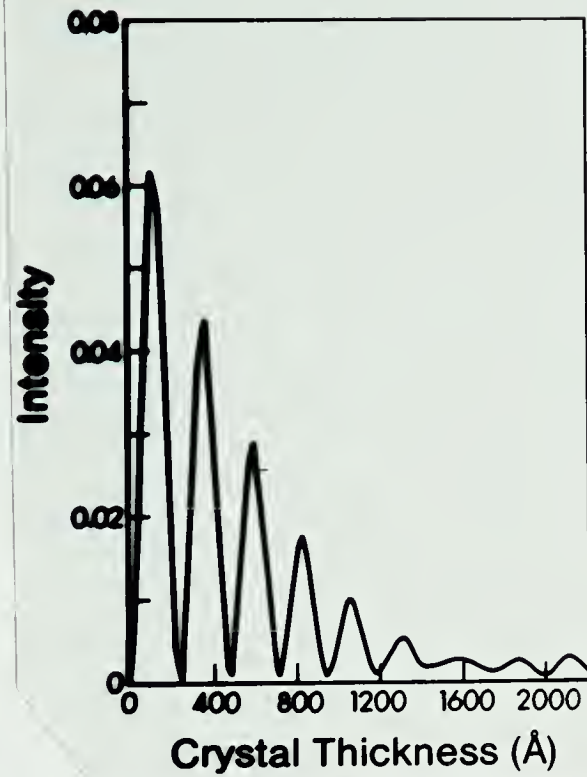
calculations for the SL case (for which  $\theta$  is set equal to zero) the intensity profiles for both the  $g$  and  $-g$  reflections were found to be identical and differed in only very minor respects from the profile shown in Fig. 7.5b. In the NSL case  $\theta$  was taken to be  $60^\circ$  and again intensity profiles for the  $g$  and  $-g$  diffracted beams were obtained. The results shown in Figs. 7.5a and 7.6a for the  $-g$  and  $g$  diffracted beams respectively indicate that high contrast fringes which are sinusoidal in character are obtained in the  $-g$  dark field image. It is clear from this figure that the first 9 fringes should be easily seen in the  $-g$  image, a result which is in excellent agreement with experiment. In the  $g$  dark field image, on the other hand, there is a strong modulation in the intensity maxima in the profile with the result that the first 6 fringes exhibit high contrast. Because of the strong modulation of the intensity maxima, fringes in thicker crystal will exhibit poor contrast and as a result only the first 6 fringes in the profile should be detected. Again this result is in excellent agreement with the experiment.

## 7.7 DISCUSSION

The differences between thickness fringes in the  $g$  and  $-g$  dark field images which have been discussed in the previous section can be understood by considering the characteristics of the Bloch waves which make important contributions to these diffracted beams. As indicated in



a



b

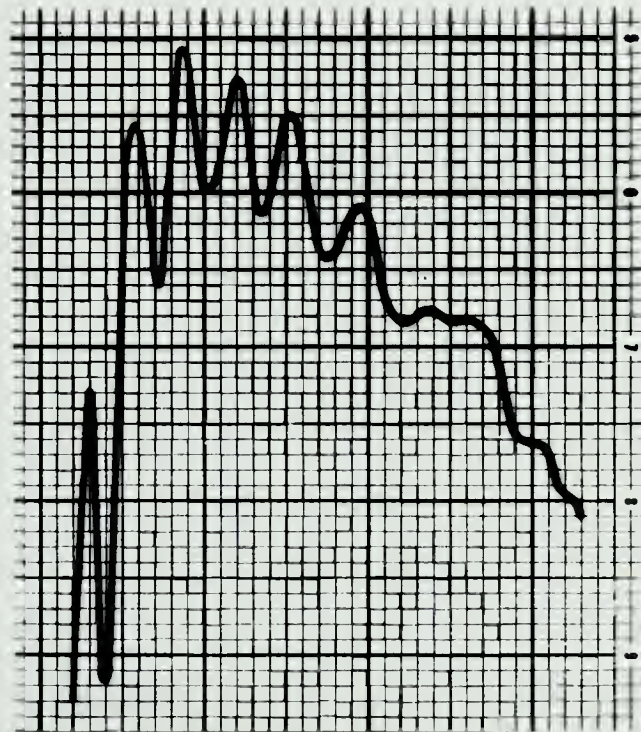


Figure 7.6 a) Shows the theoretical profile obtained by using the  $g=(0\ 2\ -2)$  reflection. Calculations were carried out for the NSL case. b) Shows the experimental densitometer trace corresponding to a).



section 7.3 and Fig. 7.3, the  $-g$  dark field image can to a good approximation be described in terms of two important Bloch waves, namely Bloch wave 1 and 2. The thickness fringes in this image will therefore arise from the presence of a cosine term in 7.13 which has a period of  $(k_z^{(1)} - k_z^{(2)})^{-1}$ . This extinction distance has a value of 236A, in agreement with the theoretical profile in Fig. 7.5a. In order to adequately describe the  $g$  dark field image, on the other hand, three important Bloch waves are required, namely Bloch waves 1, 2 and 3. The nature of the thickness fringes in this image will therefore be determined by the presence of three cosine terms in 7.13 with periods:

$$(k_z^{(1)} - k_z^{(2)})^{-1}, \quad (k_z^{(1)} - k_z^{(3)})^{-1} \quad \text{and} \quad (k_z^{(2)} - k_z^{(3)})^{-1} \quad (7.14)$$

From Fig. 7.2, which shows a schematic representation of the dispersion surface in the region of the symmetry position, it can be seen that

$$(k_z^{(2)} - k_z^{(3)})^{-1} \gg (k_z^{(1)} - k_z^{(3)})^{-1} \approx (k_z^{(1)} - k_z^{(2)})^{-1} \quad (7.15)$$

As a result the intensity profile for this diffracted beam will be characterized by an extinction distance approximately equal to  $(k_z^{(1)} - k_z^{(2)})^{-1}$  or 236A and the intensity will be modulated in a manner very similar to beats with the distance between a beat maximum and a beat





minimum equal to:

$$\frac{1}{2} (k_z^{(2)} - k_z^{(3)})^{-1} = 1590 \text{ \AA} \quad (7.16)$$

Both these values are in good agreement with the theoretical profile in Fig. 7.6a.

## 7.8 CONCLUSIONS

In order to gain some insight into the possible significance of the results obtained in this chapter for other materials, similar theoretical calculations to those presented in section 7.6 have been carried out for the (2 2 0) and (1 1 1) systematic sets in copper. Marked differences between the  $g$  and  $-g$  dark field images at the symmetry position, similar to those presented in section 7.6, were found at a value of  $\Theta=30^\circ$  for the (2 2 0) systematic set and  $\Theta=60^\circ$  for the (1 1 1) systematic set. On the other hand, for the (1 1 1) systematic set in silicon, significant differences between the  $g$  and  $-g$  dark field images at the symmetry position were not obtained for values of  $\Theta < 60^\circ$  and for accelerating voltages normally used in electron microscopy. It is clear from these results, that the errors which results when SL diffraction conditions are used to describe contrast at the symmetry orientation can occur over a wide variety of conditions depending on the material and systematic set involved.

Finally in assessing the results presented in this chapter it is important to note that previous theoretical





work (see, for example, Sheinin and Jap, 1979), has shown that significant differences can be expected if symmetrical Laue diffraction conditions are used to describe weak beam images. The symmetry position corresponds to a value of the deviation parameter which is closer to strong beam than to weak beam diffraction conditions, thus indicating that caution should also be taken in the use of the SL diffraction condition to describe images other than those obtained for the relatively large values of the deviation parameter required for weak beam imaging.



## CHAPTER VIII

### EXPERIMENTAL EVIDENCE OF A BREAKDOWN OF THE COLUMN APPROXIMATION IN CALCULATIONS OF CONTRAST IN ELECTRON MICROSCOPE IMAGES OF STACKING FAULTS

#### 8.1 INTRODUCTION

The column approximation (see chapter 3 for a detailed discussion), has been widely used in dynamical theory calculations of the contrast exhibited in electron microscope images of lattice defects. The validity of this approximation for weak beam diffraction conditions has been brought into question in theoretical calculations of dislocation profiles by the work of Howie and Sworn (1970), Humphreys and Drummond (1976) and Lewis and Villigrana (1979). In a recent paper Jap and Sheinin (1981) have also shown that the column approximation may not be valid when calculating weak beam images of stacking faults. On the basis of theoretical considerations, therefore, there seems to be a strong indication that, under certain circumstances, the column approximation is not valid. Direct experimental evidence for a breakdown of the column approximation has, however, not been presented in the literature. The purpose of this chapter is to present such an evidence. The approach is based on a comparison of experimental densitometer traces obtained from images of stacking faults in crystals of known thickness with theoretical non-column and column approximation profiles.



## 8.2 EXPERIMENTAL PROCEDURE

The experimental results to be presented in this paper were obtained from images of stacking faults in FCC cobalt. In order to carry out a comparison of non-column and column approximation calculations with experiment, the following information about the experimental stacking fault images must first be obtained: the crystal thickness in which the fault lies, the phase angle,  $a$ , of the fault ( $a = 2\pi \vec{g} \cdot \vec{R}$  where  $\vec{g}$  is the lowest order reflection in the systematic set excited and  $\vec{R}$  is the displacement vector of the fault), the edges of the image which correspond to the intersections of the fault with the top and bottom surfaces of the crystal and the angle of inclination of the fault plane with the crystal surfaces. In order to determine the crystal thickness in which the fault lies, wedge crystal specimens have been prepared. Since the wedge angles of the crystals were unknown, absolute values of crystal thickness could not be determined. However, for purposes of comparing experimental profiles with theoretical calculations, only the crystal thickness expressed in terms of extinction distance need be known. This can be easily determined from the thickness contours in the wedge crystal immediately adjacent to the image of the fault ( see, for example, Fig. 8.1 ). The phase angle  $a$  and the edges of the image which correspond to the intersections of the fault with the top and bottom surfaces of the crystal have been determined from bright and dark field images recorded under strong beam





diffraction conditions (with the deviation parameter  $s_g$  set close to zero, see for example Hirsch et. al. 1977). Finally the angle of inclination of the fault plane was determined from the projected width of the fault along the bottom surface of the crystal as obtained from the stacking fault image and the crystal thickness at this width (determined in extinction distances by the method described above and then multiplied by the theoretical extinction distance). The value so obtained was then checked by determining the angle of inclination of the fault from the orientation of the specimen obtained from the diffraction pattern, and by assuming that the fault lies on a  $\{1\ 1\ 1\}$  plane.

### 8.3 COMPARISON OF THEORY WITH EXPERIMENTAL RESULTS

Experimental stacking fault images have been obtained by first orienting the crystal so that the  $(1\ 1\ 1)$  systematic set was excited (orientations were chosen so that the effects of non-systematic reflections were minimized). The specimen was then tilted to weak beam diffraction conditions, and a dark field image was recorded (see for example Fig. 8.1). Microdensitometer traces were then obtained from these kinds of images, an example of which is shown in Fig. 8.2. Using the methods referred to in Section 8.2, it was found that the fault shown in Fig. 8.1 had a value of  $a = -2\pi/3$ . The most significant feature to note in the experimental profile in Fig. 8.2 is that there is a dark fringe at the side of the image corresponding to the





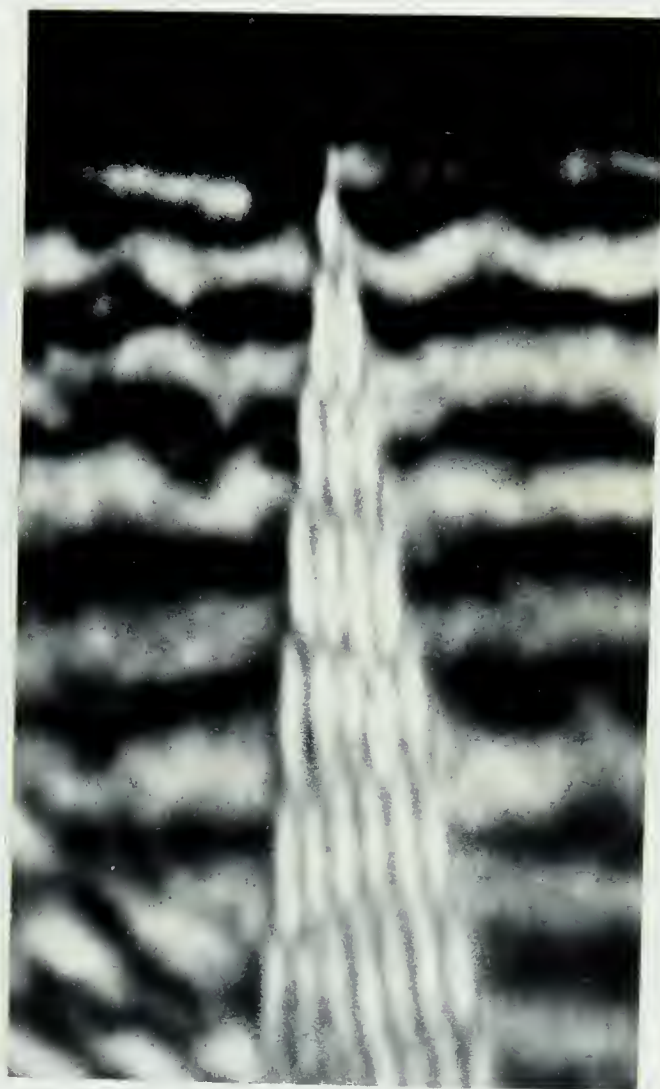


Figure 8.1 Experimental dark field of a stacking fault under weak beam diffraction conditions.



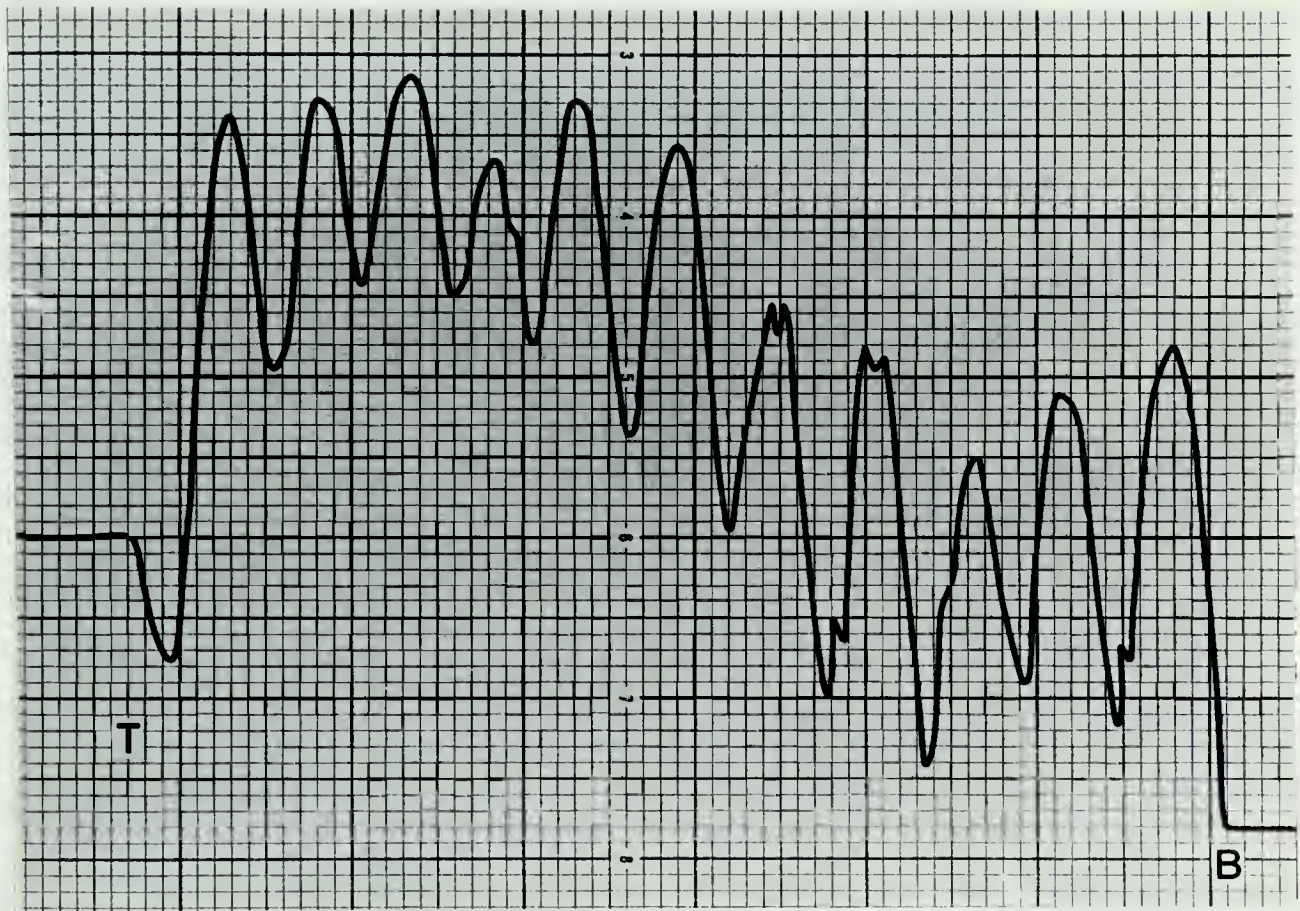


Figure 8.2 Experimental densitometer trace obtained from a weak beam stacking fault image.



intersection of the fault with the top surface while at the side of the image corresponding to the intersection of the fault with the bottom surface a bright fringe is obtained.

In order to compare the experimental results described above with theory, calculations of stacking fault profiles for both the non-column and column approximation cases were carried out. The calculations based on the column approximation were carried out by using the standard approach described extensively in the literature (see Hirsch et. al. 1977) while the non-column calculations employed the theory presented by Jap and Sheinin (1981). The results of the column approximation calculations are shown in Fig. 8.3a and indicate that a bright fringe should be obtained on both sides of the image. This is clearly in qualitative disagreement with the experimental profile in Fig. 8.2. The results of the non-column approximation calculation are shown in Fig. 8.3b and indicate that a dark fringe should be obtained at the side of the image corresponding to the intersection of the fault with the top surface while the other side should show a bright fringe. Clearly therefore, this profile is in excellent agreement with experiment.

It is important to note the following point with regard to the non-column profile in Fig. 8.3b. The dark fringe at the side of this profile corresponding to the intersection of the fault with the top surface arises from a discontinuity in the diffracted beam intensity as given by the non-column stacking fault calculation and the background





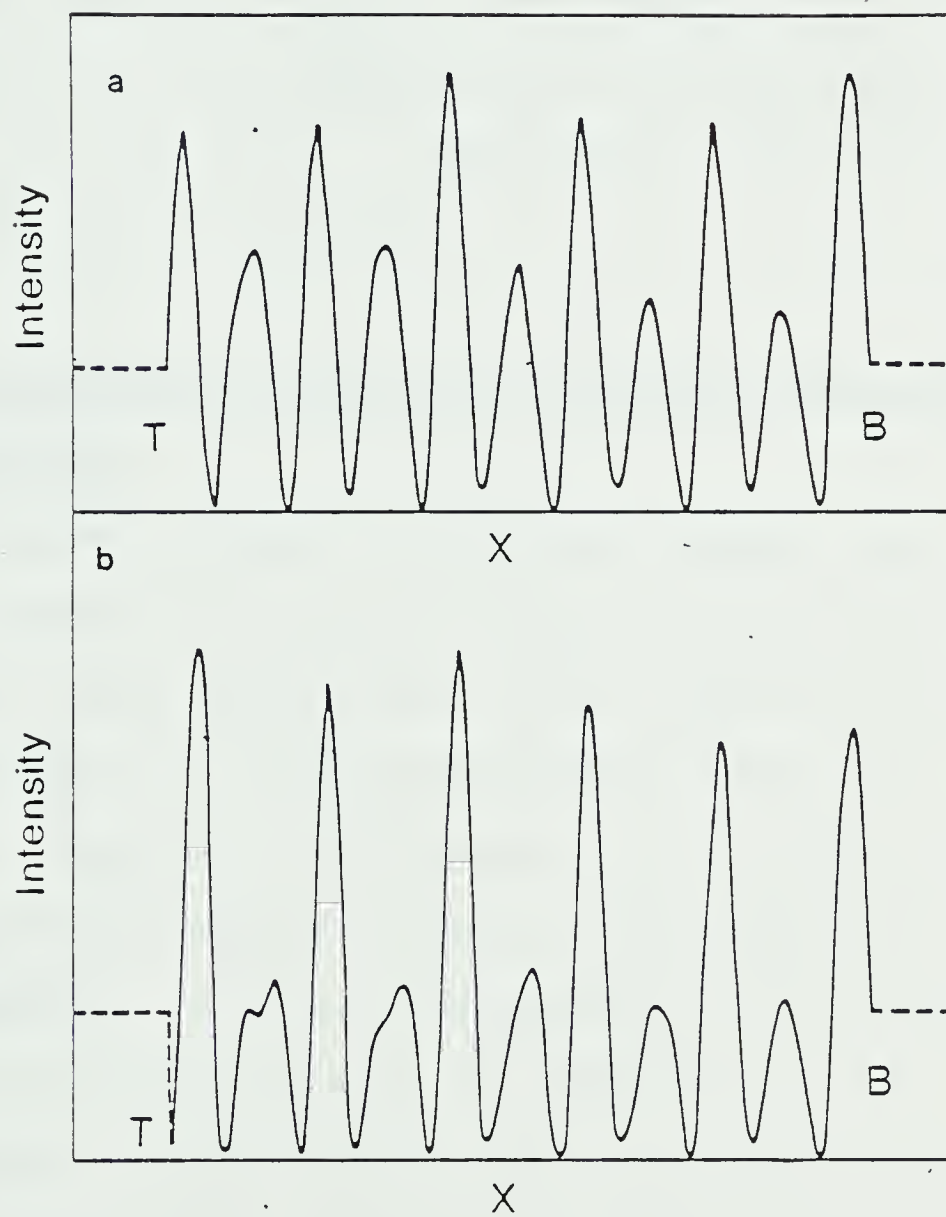


Figure 8.3 Theoretical stacking fault profiles based on a) column and b) non-column approximations.





intensity. It should be stressed that this dark fringe was in fact observed experimentally. This result is, of course, in complete contradiction to calculations based on the assumption that the column approximation is valid which always predicts the diffracted beam intensity at the edges of the profile will be continuous with background. An explanation of this significant difference between a theory based on the column approximation and one that is not is given in the next section.

#### 8.4 EXPLANATION OF DIFFERENCES BETWEEN COLUMN AND NON-COLUMN PROFILES

Stacking fault profiles based on the column approximation always give diffracted beam intensities equal to the background intensity at positions in the profile corresponding to the intersections of the fault with top and bottom surfaces. Non-column and column approximation profiles would appear to agree on the side of the profile corresponding to the intersection of the fault with the bottom surface ( see Fig. 8.3 and Jap et. al. 1981.). As mentioned in section 8.3, however, these intensities can be quite different on the side of the profile corresponding to the intersection of the fault with the top surface. In order to understand this behavior, it is useful to obtain the expressions for the diffracted beam amplitudes in the non-column and column approximation cases in comparable form.



This can be done in the column approximation case by using an expression given by Sheinin and Botros (1972) expressed in the following form:

$$\left[ \phi_g(t_1, t) \right]_C = \sum_j \sum_m x_C^{(j,m)} C_g^{(j)} \exp[2\pi i (\gamma^{(m)} - \gamma^{(j)}) t_1] * \exp[2\pi i \gamma^{(j)} t] \quad (8.1)$$

and

$$x_C^{(j,m)} = \underline{C}_O^m \underline{C}_T \{ \exp(2\pi i \vec{g} \cdot \vec{R}) \} \underline{C}_g^{(m)} \quad (8.2)$$

$t_1$  is the depth of the fault,  $t$  is crystal thickness,  $C_g^{(i)}$  is a Fourier coefficient appearing in the expression for the Bloch wave (see chapter 2).  $\underline{C}_g^m$  is a column vector whose elements are  $C_g^{(i)}$ ,  $\underline{C}$  is a square matrix whose columns are  $\underline{C}_g^m$  ( $i = 1, \dots, N$  where  $N$  is the number of beams taken into account), the subscript  $T$  indicates the transpose of a matrix and  $\{ \exp(2\pi i \vec{g} \cdot \vec{R}) \}$  is a diagonal matrix whose elements are  $\exp(2\pi i \vec{g} \cdot \vec{R})$ . The superscript  $(j,m)$  refers to a Bloch wave arising from interbranch scattering from dispersion surface branch  $m$  to  $j$  (see Fig. 8.4, noting that in the column case  $\Theta=0$  and the wave points  $(j,m)$  and  $(j,j)$  coincide). From 8.1, the diffracted beam amplitudes at positions in the profile corresponding to the intersections of the fault with the top ( $t_1=0$ ) and bottom ( $t_1=t$ ) surfaces are:

$$(\phi_g(t))_C = \sum_j \sum_m x_C^{(j,m)} C_g^{(j)} \exp[2\pi i \gamma^{(j)} t] \quad (8.3)$$

and



$$(\phi_g(t))_C = \sum_j \sum_m x_C^{(j,m)} C_g^{(j)} \exp[2\pi i \gamma^{(m)} t] \quad (8.4)$$

respectively. The corresponding non-column expressions can be obtained from the general expressions for diffracted beam amplitudes for this case (see Sheinin et. al. 1972.).

$$(\phi_g(\vec{r}_e))_{NC} = \sum_j \sum_m x_{NC}^{(j,m)} C_g^{(j,m)} \exp[2\pi i \vec{\gamma}^{(j,m)} \cdot \vec{r}_e] \quad (8.5)$$

$$x_{NC}^{(j,m)} = \underline{C}_O^{(m)} [\underline{C}^{(m)}]^{-1} \{ \exp 2\pi i \vec{g} \cdot \vec{R} \} \underline{C}_g^{(m)} \quad (8.6)$$

$C_g^{(j,m)}$  is a Fourier coefficient in the expression for a Bloch wave excited below the fault by interbranch scattering from dispersion surface branch  $m$  to  $j$ :

$$b^{(j,m)} = \sum_m C_g^{(j,m)} \exp[2\pi i (\vec{k}^{(j,m)} + \vec{g}) \cdot \vec{r}] \quad (8.7)$$

$\underline{C}^m$  is a square matrix whose columns are  $\underline{C}^{(j,m)}_g$  ( $j=1, \dots, N$ ) and  $\underline{C}^{(j,m)}_g$  is a column vector whose elements are  $C^{(j,m)}_g$ . The parameters  $\gamma^{(j,m)}$  and  $r_e$  are defined in Figs. 8.4 and 8.5. Using 8.5 and the fact that:

$$\gamma_X^{(j,m)} = (\gamma^{(m)} - \gamma_Z^{(j,m)}) \tan \theta \quad (8.8)$$

(see Fig. 8.4), the diffracted beam amplitudes at positions in the profile corresponding to the intersections of the fault with the top ( $x=0, z=0$ ) and bottom ( $x=t/\cos\theta, z=t$ ) surfaces are:



$$(\phi(t))_{NC} = \sum_j \sum_m X_{NC}^{(j,m)} C_g^{(j,m)} \exp[2\pi i \gamma^{(j,m)} t] \quad (8.9)$$

and

$$(\phi_g(t))_{NC} = \sum_j \sum_m X_{NC}^{(j,m)} C_g^{(j,m)} \exp[2\pi i \gamma^{(m)} t] \quad (8.10)$$

It is first of interest to compare the non-column and column approximations for the diffracted beam amplitude at the intersections of the fault with the bottom surface by comparing 8.4 and 8.10. It is clear from these equations that the phase angles in each case are the same and any difference in diffracted beam amplitude must therefore arise from differences in the amplitude terms:

$$X_{NC}^{(j,m)} C_g^{(j,m)}, \quad X_C^{(j,m)} C_g^{(j)} \quad (8.11)$$

It turns out in fact that these amplitude terms are very nearly the same over a wide range of conditions. Thus, for example, under weak beam diffraction conditions  $C^{(j,m)}_g$  and  $C^{(j)}_g$  typically differ by less than about 5% for angles of inclination of the fault,  $\theta$ , up to about  $75^\circ$ . Under these circumstances  $\underline{C}^m$  in eq. 8.6 is approximately equal to  $\underline{C}$  in eq. 8.2. Since  $\underline{C}$  is an orthogonal matrix:

$$[\underline{C}^m]^{-1} \cong \underline{C}^T \quad (8.12)$$

and therefore





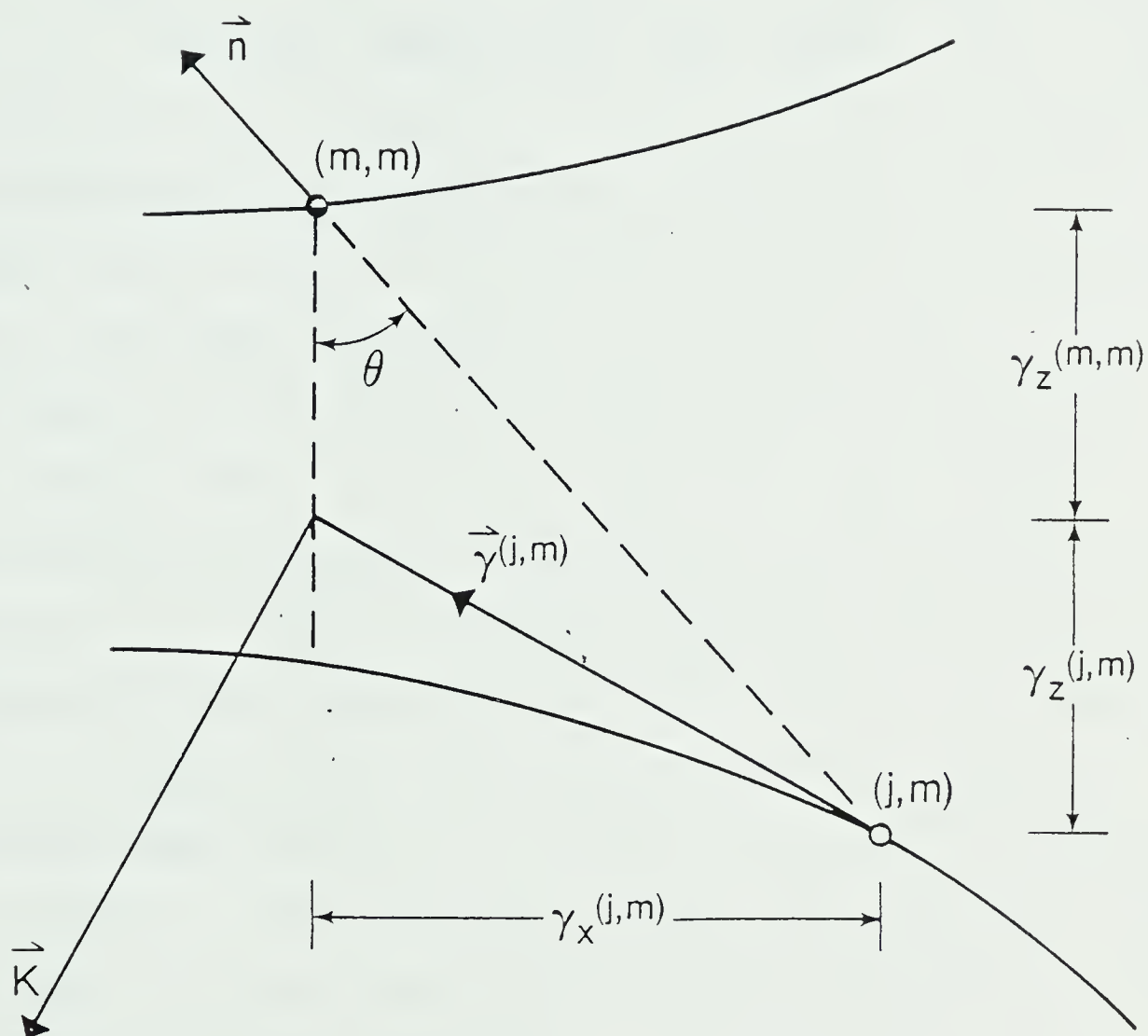


Figure 8.4 Schematic diagram in reciprocal space showing the wave points associated with Bloch waves excited below the stacking fault in Fig. 8.5



$$x_{NC}^{(j,m)} \approx x_C^{(j,m)} \quad (8.13)$$

The result that diffracted beam intensities at the intersection of the fault with the bottom surface are very nearly equal in the non-column and column approximation cases is therefore explained. The reason that these intensities are different at the position in the profile corresponding to the intersection of the fault with the top surface can now also be understood by comparing equation 8.3 and 8.9. The amplitude terms as discussed above, will be approximately the same for a wide range of conditions. The phase angle  $(2\pi\gamma^{(j,m)}t)$  and  $(2\pi\gamma^{(j)}t)$  can, however, be significantly different, even though the differences in the values of  $\gamma^{(j,m)}$  and  $\gamma^{(j)}$  may be relatively small. This can be seen by taking typical values of  $t$  and  $\gamma^{(j)}$  of  $1000\text{\AA}$  and  $5 \times 10^{-3}\text{\AA}^{-1}$  respectively. These values give a difference in the above phase angles of  $\pi$  for only a 5% difference between  $\gamma^{(j,m)}$  and  $\gamma^{(j)}$  with the result that the diffracted beam amplitudes in the non-column and column approximation cases can be significantly different.

### 8.5 DISCUSSION

The differences between non-column and column approximation calculations of stacking fault profiles discussed in section 8.4 can lead to serious interpretative errors if analysis is based on the column approximation



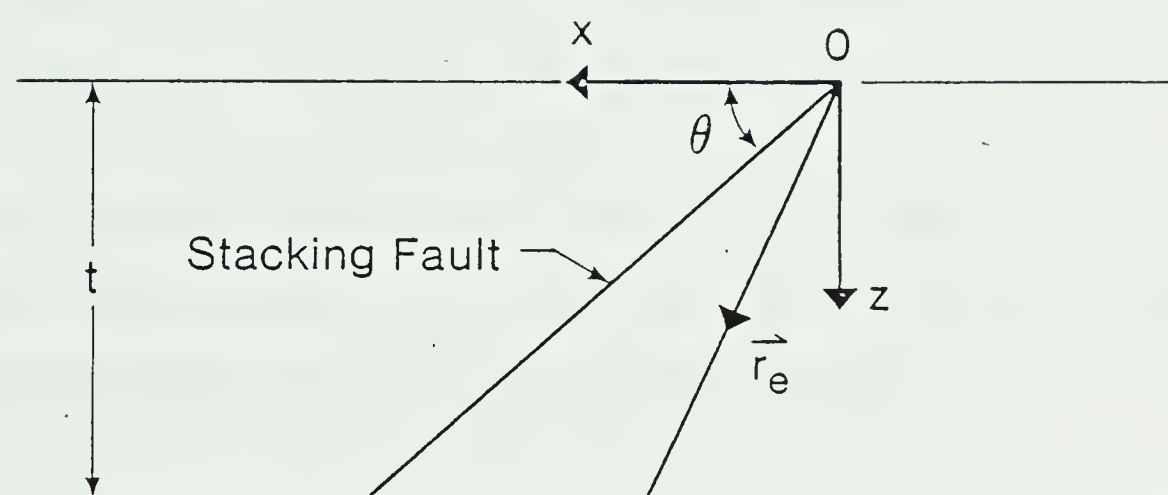


Figure 8.5 Schematic diagram in real space showing a stacking fault in a crystal of thickness  $t$ .  $O$  is the origin of the coordinate system and  $\vec{r}$  is a position vector terminating on the exit surface.



profile. Thus, for example, column approximation stacking fault profiles obtained for weak beam diffraction conditions are symmetrical for both  $a=\pm 2\pi/3$  faults in the sense that both edge fringes exhibit the same contrast. In section 8.3 it was shown that the experimentally observed profile for  $a=-2\pi/3$  is in fact asymmetrical. Thus interpretation based on the column approximation could lead the electron microscopist to suspect that the defect image does not have the usual values of displacement vector of the type  $1/6(1\ 1\ 2)$  and is therefore not one of the commonly occurring intrinsic or extrinsic faults in FCC materials. The fact is, of course, that the fault does have a value of  $a=-2\pi/3$  and the asymmetry arises from the fact that the column approximation fails. It is clear from these results that great care should be exercised in interpreting weak beam profiles based on the column approximation.





## CHAPTER IX

### SUGGESTIONS FOR FURTHER WORK

There are a number of areas in which the work presented in this thesis can be extended. The first of these follows from the assessment of the effects of systematic reflections in HCP crystals carried out in chapter 4. Past investigations (see, for example, Cann, 1973) has shown that non-systematic reflections can have an important effect on extinction distance, anomalous absorption and image intensity. It would therefore be of interest to carry out an experimental investigation of the effects of non-systematic reflections on the image contrast obtained in HCP perfect crystals.

A second possible extension of the work presented in this thesis is concerned with the image contrast obtained from twin boundaries when common reflections are excited. Experimental measurements of the body translation vector have been carried out in the past using the two-beam approximation of the dynamical theory, which assumes that only one common reflection is excited. However, the presence of non-common and forbidden reflections can have an important effect on the image contrast. The many-beam approximation of the dynamical theory which has been developed in chapter 6 includes common, non-common and forbidden reflections. It would therefore be of interest to carried out an experimental determination of the body translation vector based on theoretical calculations carried



out with a more exact form of the twin boundary image contrast theory.

The next point which is of considerable interest is the study of the nature of stacking fault contrast in the presence of non-systematic reflections in FCC and HCP materials. Some of the objectives of this study would be to answer questions such as what mechanisms give rise to stacking fault contrast in the presence of this particular kind of reflections.



## BIBLIOGRAPHY

Amelinckx, S., Gevers, R. and Van Landuyt, J. (1978),  
Diffraction and Imaging Techniques in Materials  
Science., North-Holland.

Bethe, M. A. (1928), Ann. Phys., Lpz. 87, 55

Berghezan, A., Fourdeux, A. and Amelinckx, S. (1961), Acta  
Metallurgica, 9, 464.

Bibby, M. J. and Gordon Parr, J. (1963), Cobalt # 20.

Bonnet, N. (1976), Ph. D. Thesis, Universite de Reims.

Botros, K. Z. (1973), Ph. D. Thesis, University of Alberta.

Botros, K. Z. and Sheinin, S. S. (1975), Phys. Stat. Sol.  
(a), 31, 625.

Botros, K. Z., Perez, R. and Sheinin, S. S. (1979), Phys.  
Stat. Sol (a), 51, 41

Bristowe, P. D. and Crocker, A. G. (1975), Phil. Mag., 31,  
503.



Cann, C. D. (1967), M. Sc. Thesis, University of Alberta.

Cann, C. D. (1973), Ph. D. Thesis, University of Alberta.

Corbett, J. M. and Sheinin, S. S. (1976), Phys. Stat. Sol.  
(a), 38, 151.

Cowley, J. M. and Moodie, A. F. (1957), Proc. Phys. Soc. B,  
70, 486.

Dupouy, G., Perrier, F., Uyeda, R., Ayroles, R. and Mazel,  
A. (1965), J. Microscopie, 4, 429.

Edwards, O. S. and Lipson, H. (1943), J. Inst. Metals, 69,  
177.

Gevers, R., Art, A. and Amelinckx, S. (1963), Phys. Stat.  
Sol. 3, 1563.

Gevers, R. (1963), Phys. Stat. Sol. 3, 2289.

Gomez, A., Romeu, D. and Yacaman, M. J. (1980), Inst. Phys.  
Conf. Ser. #52, 215.

Goringe, M. J., Howie, A. and Whelan, M. J. (1966), Phil.  
Mag. 14, 217.





- Gratias, D. and Portier, R. (1980), Journal of Microscopy, 120, Pt. 2, 129.
- Grundy, P. J. and Tebble, R. S. (1964), Journal of Applied Phys. 35, # 3, 923.
- Grundy, P. J. (1965), Phil. Mag. 12, 335.
- Hashimoto, H., Howie, A. and Whelan, M. J. (1962), Proc. Roy. Soc. A269, 80.
- Hirth, J. P. and Lothe, J., (1968), Theory of Dislocations, McGraw-Hill Book Company.
- Hirsh, P. B., Howie, A., Nicholson, R. B., Pashley, D. W. and Whelan, M. J. (1977), Electron Microscopy of Thin Crystals. Robert E. Krieger Publishing Company, New York.
- Howie, A. and Whelan, M. J. (1961), Proc. Roy. Soc. A263, 217.
- Howie, A. and Basiski, Z. S. (1968), Phil. Mag. 17, 1039.
- Howie, A. and Sworn, C. H. (1970), Phil. Mag. 22, 361



Howie, A. and Whelan, M. J. (1963), Phil. Mag. 8, 1083.

Humphreys, C. J., Howie, A. and Booker, G. R. (1967), Phil. Mag. 15, 507

Humphreys, C. J., Thomas, L. E., Lally, J. S. and Fisher, R. M. (1971), Phil. Mag. 23, 87.

Humphreys, C. J. and Drummond, R. A. (1976), 6-th. European Congress on Electron Microscopy, Jerusalem, 142.

Jap, B. K. and Sheinin, S. S. (1981), Phys. Stat. Sol. (b), 105, 137.

Jones, I. P. (1978), Phys. Stat. Sol. (a), 47, 163.

Jouffrey, B. and Taupin, D. 1967), Phil. Mag. 16, 703.

Kim, H. S. and Sheinin, S. S. (1982), Phys. Stat. Sol. (a), 72, 561.

Kim, H. S., Perez, R and Sheinin, S. S. (1982) Phys. Stat. Sol (a), 72, 561

Lally, J. S., Humphreys, C. J., Metherell, A. J. F. and Fisher, R. M. (1972), Phil. Mag., 25, 321.



Lewis, A. L. and Villigrana, R. E. (1979), Acta Crys. A 35, 276.

Marukawa, K. (1977), Phil. Mag. 36, # 6, 1375.

Metherell, A. J. F. and Fisher, R. M. (1969), Phys. Stat. Sol. 32, 551.

Nagata, F. and Fukuhara, A. (1967), Japan J. Appl. Phys. 6, 1233.

Perez, R., Botros, K. Z. and Sheinin, S. S. (1981) Phys. Stat. Sol. (a), 68, 91

Pond, R. C. and Smith, D. A. (1976), 6-th. European Congress on Electron Microscopy. Jerusalem.

Pond, R. C. (1978), Phil. Mag. A 37, # 5, 699.

Salding, D. K., Whelan, M. J. and Rossouw, C. J. (1978), Inst. Phys. Conf. Ser. # 41, 50.

Serneels, R. and Gevers, R. (1969), Phys. Stat. Sol. 33, 703.

Serneels, R. and Gevers, R. (1971), Phys. Stat. Sol. 45, 493.



Sheinin, S. S. and Jap, B. K. (1979), Phys. Stat. Sol. (b),  
91, 407.

Sheinin, S. S. (1967), Phys. Stat. Sol. 21, 247.

Sheinin, S. S., Botros, K. Z. and Cann, C. D. (1970), Phys.  
Stat. Sol. (a) 3, 537

Sheinin, S. S. (1970), Phys. Stat. Sol. 37, 683.

Sheinin, S. S. and Botros, K. Z. (1972), Phys. Stat. Sol.  
(a), 12, 549.

Sheinin, S. S. and Corbett, J. M. (1976), Phys. Stat. Sol.  
(a), 38, 675.

Sheinin, S. S. and Jap, B. K. (1979), Phys. Stat. Sol. (b),  
91, 407.

Sheinin, S. S. (1966), Rev. Sci. Instr. 37, 232.

Sheinin, S. S. (1970), Phys. Stat. Sol. 38, 675.

Sheinin, S. S. and Botros, K. Z. (1972), Phys. Stat. Sol.  
(a), 13, 585.





Spencer, J. P. and Humphreys, C. J. (1971), Proc. 25-th. Anniversary Meeting of EMAG, Inst. of Physics, 310.

Sutton, A. P. and Pond, R. C. (1978), Phys. Stat. Sol. (a), 45, 149.

Troiano, A. R. and Tockich, J. L. (1948), Trans. AIME, 175, 728.

Uyeda, R. (1968), Acta Cryst. A24, 175.

Vitek, V. (1970), Scripta Metall. 4, 725.

Wagner, R. S., Ellis, W. C., Jackson, K. A. and Arnold, S. M. (1964), Journal of Applied Phys. 35, 2993.

Whelan, M. J. and Hirsch, P. B. (1957), Phil. Mag. 2, 1303.

Whelan, M. J. and Hirsch, P. B. (1957), Phil. Mag. 2, 1121.

Yamaguchi, M. and Vitek, V. (1976), Phil. Mag. 34, 1.

Yoshioka, H. (1957), J. Phys. Soc. Japan. 12, 618.















**B30395**